

Generation and interactions of energetic tin ions

Marten Johannes Deuzeman

Zernike Institute PhD thesis number: 2019-14
ISSN: 1570-1530
ISBN (printed version): 978-94-034-1619-9
ISBN (electronic version): 978-94-034-1618-2



**university of
 groningen**

**faculty of science
 and engineering**

**zernike institute for
 advanced materials**

The research presented in this PhD thesis was performed in the research group Quantum Interactions and Structural Dynamics which is part of the Zernike Institute for Advanced Materials at the University of Groningen, the Netherlands.

The research has been financed by and was partly carried out at the Advanced Research Center for Nanolithography (ARCNL), a public-private partnership between the University of Amsterdam (UvA), Vrije Universiteit Amsterdam (VU Amsterdam), the Netherlands Organization for Scientific Research (NWO), and the semiconductor equipment manufacturer ASML.



Printed by: Gildeprint, Enschede, May 2019



rijksuniversiteit
groningen

Generation and interactions of energetic tin ions

Proefschrift

ter verkrijging van de graad van doctor aan de
Rijksuniversiteit Groningen
op gezag van de
rector magnificus, prof. dr. E. Sterken
en volgens besluit van het College voor Promoties.

De openbare verdediging zal plaatsvinden op

vrijdag 21 juni 2019 om 12.45 uur

door

Marten Johannes Deuzeman

geboren op 27 juli 1990
te Rotterdam

Promotores

Prof. dr. ir. R.A. Hoekstra

Prof. dr. W.M.G. Ubachs

Copromotor

Dr. O.O. Versolato

Beoordelingscommissie

Prof. dr. F. Aumayr

Prof. dr. J.W.M. Frenken

Prof. dr. ir. B.J. Kooi

ISBN (printed version): 978-94-034-1619-9

ISBN (electronic version): 978-94-034-1618-2

Contents

1	Introduction	1
1.1	Thesis aim and outline	4
2	Ion distribution and ablation depth measurements of a fs-ps laser-irradiated solid tin target	7
2.1	Introduction	8
2.2	Experimental Setup	10
2.3	Results & Discussion	12
2.4	Conclusions	23
3	Sn ion energy distributions from laser produced plasmas	25
3.1	Introduction	26
3.2	Theoretical models	27
3.3	Experimental setup	29
3.4	Results and discussion	32
	3.4.1 Changing pulse duration	32
	3.4.2 Changing laser energy density	35
3.5	Conclusion	40
4	Interactions of energy-, charge-state-, and mass-selected tin ions with solid surfaces	43
4.1	Atomic interactions	44
	4.1.1 Scattering	44
	4.1.2 Stopping	47
4.2	Electronic processes	51
	4.2.1 Over-the-barrier	51

4.2.2	Electron capture	54
4.2.3	De-excitation of the ion	56
4.3	Ion source	57
4.3.1	Oven	60
4.4	The ion-surface setup	62
4.4.1	Beam deceleration	63
4.4.2	Electrostatic Analyzer	65
4.4.3	Tin ion detection efficiency	67
4.4.4	Electron measurements	68
4.5	SRIM	73
5	Backscattering of tin ions from a molybdenum surface	77
5.1	Introduction	78
5.2	Tin ion scattering	79
5.2.1	Experimental procedure	79
5.2.2	Typical tin scattering results	80
5.2.3	SRIM simulations	84
5.3	Results	85
5.3.1	Charge state	88
5.3.2	Ion species	89
5.3.3	Electronic structure	92
5.3.4	Target surface	94
5.3.5	Difference in ions and neutrals	96
5.3.6	SRIM-related reasons	101
5.4	Conclusions	105
6	A comparative study of two simulation methods for ion scattering	107
6.1	Introduction	108
6.2	Results	109
6.2.1	Simulations on pure ruthenium	109
6.2.2	Comparison to simulations on RuO ₂	114
6.2.3	Comparison to TOF measurements	117
6.3	Conclusions	119
7	Summary & Outlook	121
7.1	Outlook & future experiments	125

<i>CONTENTS</i>	vii
8 Samenvatting	127
A ESA power supplies	133
B Labview control program	137
C Atomic units	143
Curriculum Vitae	145
Bibliography	147
Dankwoord	157

Chapter 1

Introduction

In 1965, George Moore predicted in a now-famous paper [1] that the number of components per integrated circuit would double each year in the next decade. When this came true, the prediction became Moore's Law, albeit with a revised number of a doubling every two years [2]. Moore's Law held up over the next decades by reducing the minimum feature size, or *critical dimension*, imprinted on the chips, which is directly related to the ever-increasing performance of all kind of computers. The critical dimension is proportional to the wavelength of the light used in lithography, and inversely proportional to the numerical aperture [3]. Since the early 1990s, a wavelength of 193 nm is used, and the critical dimension is decreased by increasing the numerical aperture and by other, process-related, techniques (e.g. refs. [4, 5]). The next step in decreasing the minimum feature size is by reducing the wavelength used in the lithography machines, into the extreme ultraviolet (EUV) range around 10 nm [6]. In this wavelength range, no lenses and only multilayer Bragg reflector-based mirrors are available as optics [7]. These mirrors have a very narrow bandwidth and limit the choice in light sources. The best-reflecting mirrors are Mo/Si-multilayer mirrors [8, 9]. These mirrors reflect light around 13.5 nm with a bandwidth of roughly 2 percent [10].

For 13.5 nm, the most viable candidate as light source is a laser-produced plasma (LPP) of tin droplets (see figure 1.1) [11, 12]. The droplets are irradiated by a relatively low-energy infrared laser pulse, a so-called *pre-pulse*. This pre-pulse deforms the droplet into a pancake-like shape. This shape enhances the laser absorption efficiency for a more intense laser pulse, the *main pulse*. The main pulse obliterates the droplet and ionizes the tin atoms, leading to a dense plasma. The plasma consists mainly of tin ions with charge states ranging from 8+-14+. The tin ions have strong atomic transitions for all those charge states from the configurations $4p^6 4d^{m-1} 4f$, $4p^6 4d^{m-1} 5p$, and $4p^5 4d^{m+1}$ towards the ground electronic configuration $4p^6 4d^m$ (where m ranges from 0 for Sn^{14+} to 5 for Sn^{9+}), all in a narrow wavelength range around 13.5 nm [13, 14]. Because the ions have such strongly overlapping transitions, regardless of the charge state, an efficient generation of EUV light is possible. The EUV light is collected by the *collector mirror*, which focuses the light towards the lithography machine. Several multilayer mirrors transport the light to the wafer whereupon the features are imprinted.

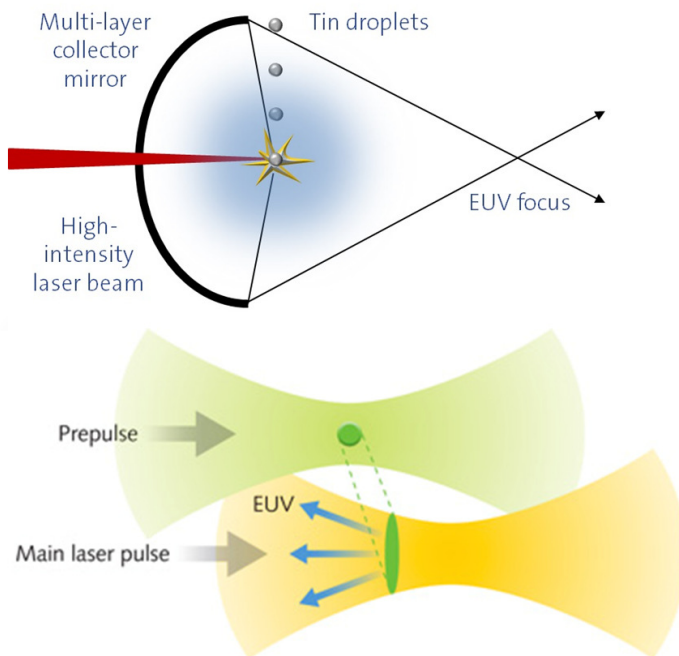


Figure 1.1: (top) Schematics of the formation of the laser-produced plasma in the 13.5 nm EUV source. The irradiated tin droplets form a EUV-emitting plasma. The EUV light is collected and reflected by the collector mirror and is transported towards the rest of the lithography machine. (bottom) A relatively low-energy pre-pulse deforms the droplet, in order to enhance the laser absorption efficiency of the target for the high-energy main laser pulse.

A point of concern in EUV light sources is the debris generated by the plasma, which may damage plasma-facing material and equipment such as the multilayer mirror [15]. Two types of debris are present: large tin particles with diameters up to several micrometers, and tin ions and atoms with a wide range of kinetic energies [16]. The debris may damage the collector mirror directly or form a non-uniform coverage layer on top of its surface [17], which may decrease the reflectivity of the mirror and

reduce its lifetime [18]. The micro-particles are largely mitigated by using a droplet as a target because it is a mass-limited target, for which is shown that they completely vaporize during plasma formation [19]. The origin of micro-particles and their interactions with solid state targets are out of the scope of this work.

The second type of debris is tin atoms and ions emitted by the plasma each time a LPP is formed, as the plasma is not contained. These ions are highly charged and can attain energies up to tens of keV [11]. The debris has therefore to be mitigated, to reduce its impact on plasma-facing materials [20]. The most promising mitigation technique is to stop both neutral as well as ionic debris with a hydrogen background gas [21, 22]. One would like to keep the H_2 pressure as low as possible not to reduce the transmission of the desired EUV light, and to limit the generation of additional hydrogen ions [23] which can interact with the surroundings, too. It is therefore important to have just sufficient mitigation of the atomic and ionic debris.

1.1 Thesis aim and outline

Due to the transient nature of the plasma in EUV light sources in combination with its unique temperature and density (see figure 1.2) the understanding of the fundamental physics is rudimentary. The first aim of this thesis is to address the plasma expansion mechanisms leading to production of energetic ions. By investigating the ionic yields and their energy distribution for different drive-laser settings we get more insight in the characteristics of the plasma.

The second aim of this thesis is to get a better understanding of the ion-surface interactions. Especially for relatively heavy ions such as tin, effects of their interactions with surfaces are mainly assessed with help of simulations which by and large lack experimental benchmarking of for example the interaction potentials. We investigate experimentally tin ion-surface interactions and make a comparison with standard simulation packages, which helps to determine to which energies the ionic debris has to be decelerated in order to not damage plasma-facing materials.

In chapter 2, I will discuss laser ablation experiments conducted at a laser facility at AMOLF, Amsterdam. We used a pulsed laser with pulse

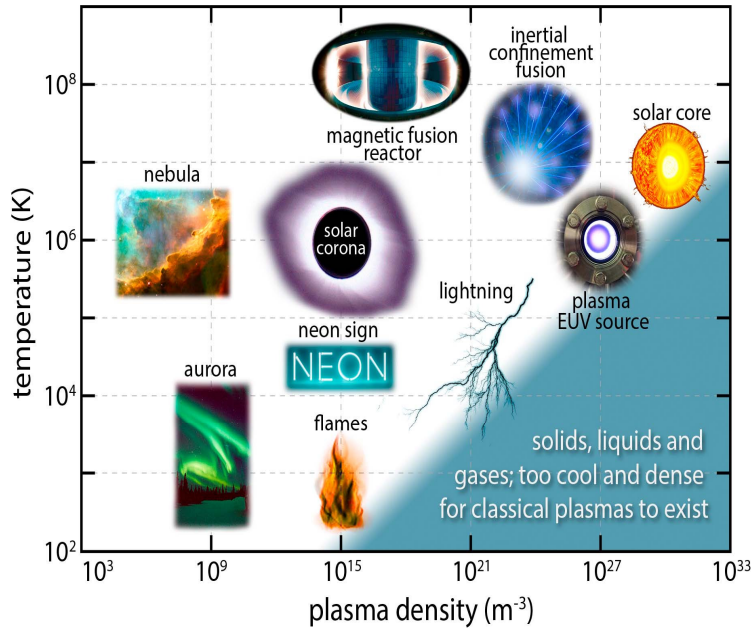


Figure 1.2: An overview of the density and temperature for several kinds of plasma. The plasmas in EUV sources have a combination of temperature and density not seen in other plasmas.

lengths in the range of femtoseconds and picoseconds to ablate a solid tin target. The kinetic energy of the ions formed in this process are measured over a wide range of energies and pulse lengths, and after the ablation experiments the amount of ablation (crater formation) is determined through optical inspection. In this way, we got a better understanding of the ionization and ablation mechanisms, and we determined the energies of the tin ions which are to be used in the ion-surface interaction experiments.

In chapter 3, the results of the ablation of the solid Sn target are combined with the results of the ablation of a tin droplet. Two plasma expansion models are tested against the ion energy distributions from these experiments, and the similarities and differences of the results obtained from the different targets are investigated.

In chapter 4, I will give an overview of the interactions relevant to

understand the results of ion-surface experiments. I will also describe the ZERNIKELEIF facility for low energy ion beams at the Zernike Institute for Advanced Materials (University of Groningen) with emphasis on the equipment especially built to accommodate tin ion-surface experiments.

The results of tin ion backscattering experiments on molybdenum are discussed in chapter 5. This includes the comparison to the results of a widely used simulation package called SRIM. The aim of this chapter is to investigate whether the interaction between a heavy ion with keV kinetic energies and a target with a similar mass is properly understood and how reliable these simulations are.

Chapter 6 consists of a study into the simulations program SDTrimSP, which is an alternative for SRIM in simulating ion-surface interactions. We compare for these simulations the agreement with the experimental data and the differences and similarities with the results of SRIM. SDTrimSP shows some promising results and is worthwhile to use in later simulations of ion-surface experiments.

Chapter 2

Ion distribution and ablation depth measurements of a fs-ps laser-irradiated solid tin target¹

This chapter describes the results of laser ablation of a solid tin target with a fs-ps laser system. The ion yield and energy distributions are measured for various detection angles in a pulse length range from 500 fs to 4.5 ps and a fluence range from 0.9 to 22 J/cm². The target is investigated with a optical microscope to measure the ablation depth and volume. We find that the ion yield increases while the depth decreases for longer pulse lengths, which we attribute to laser absorption by the plasma vapor in front of the target. The maximum ionization fraction found is 5-6%, which is considerably lower than the typical ionization fractions found for nanosecond-pulse ablation.

¹M.J. Deuzeman, A. S. Stodolna, E. E. B. Leerssen, A. Antoncicchi, N. Spook, T. Kleijntjens, J. Versluis, S. Witte, K. S. E. Eikema, W. Ubachs, R. Hoekstra, O. O. Versolato, J. Appl. Phys., **121**, 103301 (2017)

2.1 Introduction

Ultrafast lasers, with pulse durations in the femtosecond-picosecond range, are used in a wide range of applications, such as micromachining, thin film deposition, material processing, surface modification, and ion beam generation (refs. [24]-[32]). More recently, these lasers have attracted attention for their possible applicability in the field on tin-based plasma sources of extreme ultraviolet (EUV) light for nanolithography. There they could be used for generating a fine-dispersed liquid-metal target [33] before the arrival of a high-energy main-pulse responsible for the EUV emission, enhancing laser-plasma coupling [14]. The utilization of a fs-ps laser system could strongly reduce fast ionic and neutral debris from EUV sources compared with nanosecond-pulses [34], enabling better machine lifetime [11].

Since the 1990s many experiments have been performed and models developed [25, 26] for laser-matter interaction at this particular time scale. Target materials used are metals such as gold, silver, copper and aluminum (refs. [28], [34]-[42]), and non-metals such as silicon (refs. [43]-[46]) and metal oxides [47, 48, 49], among others [50, 51]. Most of these studies are conducted in a femtosecond pulse length range from 50 fs up to approximately 1 ps and a pulse fluence up to 10 J/cm^2 . In almost all studies the wavelength of the laser is in the infrared, where commercial laser systems are readily available. The focus is often either on ablation depth or ion distributions (energy, yield or angular), with a few exceptions such as the work of Toftmann et al. [34] which addresses both. A detailed study of laser ablation of the relevant element tin, including both depth and ion emission distribution, has not yet been performed in the fs-ps domain. Such a study, however, is indispensable for exploring EUV plasma sources in the short-pulse regime.

In this work, we present for the first time a systematic study of the laser ablation of a solid tin target by an 800-nanometer-wavelength laser, where we combine ablation depth and volume measurements with ion distribution measurements. We determine the angle-resolved yield and energy distributions of the produced plasma ions through time-of-flight techniques. The depth of the ablation crater was established in addition to the ion measurements using a high-numerical-aperture optical microscope. We varied the laser pulse length between 500 fs and 4.5 ps, a range which is

minimally investigated. In this pulse length range lies a transition regime in which the transfer of laser energy from the heated electrons to the lattice starts playing a significant role [26, 27]. Recent work using ultrafast laser pulses to irradiate molten-tin microdroplets hinted at a dramatic change in laser-metal coupling at 800 fs pulse length, resulting in a simultaneous sharp increase in droplet expansion velocity [33] and a strong dip in the yield of fast ionic debris [52]. This makes it highly desirable to provide further data in this pulse length regime. In our experiments, we additionally study the influence of pulse fluence in detail, covering a range from 0.9 to 22 J/cm², similar as in refs. [33, 52], broader than most studies of ablation of solid targets. At the high end of this fluence range, the total volume of ablated material reaches $\sim 10^4 \mu\text{m}^3$, which is similar to the volume of a tin droplet used in state-of-the-art plasma sources of EUV light and therefore provides an interesting comparison.

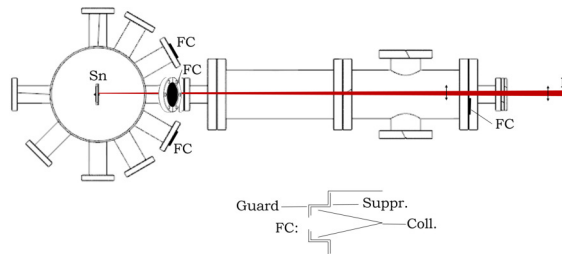


Figure 2.1: The outline of the setup (top view) used for the experiments. The four dark black spots mark the positions of the Faraday cups (FCs): one at 2° and three at 30° with respect to the normal of the target. Two of the 30°-FCs and the 2°-FC are in the horizontal plane, one of the 30°-FCs is out of plane. The laser beam (red), horizontally polarized, is incident on the target under normal angle. A schematic cut-through of a home-made FC is also shown. The outer guard shield has a diameter of 6 mm, the inner suppressor shield a diameter of 8 mm. The ion currents are obtained from the collector cone.

2.2 Experimental Setup

A solid planar polycrystalline 99.999% pure tin target with a 1-millimeter-thickness is irradiated by a pulsed 800-nanometer-wavelength Ti:Sapphire laser (Coherent Legend USP HE). The laser beam is incident on the target at normal incidence. The target and detectors is kept at a vacuum of 10^{-8} mbar. The laser pulses have a Gaussian-shaped temporal and spatial profile. All pulse lengths presented in this work are the full-width at half-maximum (FWHM) of the pulse in time-domain. The pulse duration has been changed between 500 fs and 4.5 ps by varying the group velocity dispersion in the compressor of the amplified laser system. The resulting pulse duration was measured using a single-shot autocorrelator. The beam profile of the pulses are slightly elliptical, with a FWHM of 105 ± 5 μm on the long axis and 95 ± 5 μm on the short axis. The peak fluence, the maximum fluence attained in the center of the Gaussian pulse, is calculated using these widths and the pulse energy. This fluence is varied with a $\lambda/2$ wave plate in combination with a thin-film polarizer, which leaves the spatial profile of the laser beam unchanged. The pulse repetition rate of 1 kHz is reduced with pulse-picking optics to an effective rate of 5 Hz to enable shot-to-shot data acquisition and controlled target movement between the laser pulses. The polarization of the laser light is horizontal (see figure 2.1). As the pulses are incident on the target at normal incidence, no dependence on the polarization is expected.

Time-of-flight (TOF) ion currents are obtained from Faraday cups (FCs) set up around the target, one at 2° from the surface normal and at a distance of 73 cm, two at 30° and 26 cm (in horizontal and vertical position) and one at 30° and 24 cm (also in the horizontal plane). Three FCs are home-made and consist of a grounded outer guard shield, an inner suppressor shield, and a charge-collector cone (cf. inset in figure 2.1). A voltage of -100 V on the suppressor shield inhibits stray electrons entering the collector cone and secondary electrons, which may be produced by energetic or multi-charged ions [53], from leaving it. To further reduce the chance of stray electrons arriving at the collector, a bias voltage of -30 V is applied to the collector cone itself. The other FC (at 30° and 24 cm) has a different design (model FC-73A from Kimball Physics) and can be used for retarding field analysis. Checks with retarding grids using this FC indicate that ions with energies below 100 eV, the vast majority of the

ions, are mostly singly charged. The charge yield measured with a FC can thus be regarded as a direct measure of the ion yield. Only at the highest observed kinetic energies could traces of higher charge states be found. In the conversion from a TOF- to a charge versus the ion energy-signal, the signal is corrected for the non-constant relation between bin size in the time- and in the energy-domain using

$$S_E = \left| \frac{dt}{dE} \right| S_t = \frac{t}{2E} S_t, \quad (2.1)$$

in which S_E and S_t are the signals in respectively the energy domain and the time domain, and t and E respectively denote the TOF and the ion energy. Signals are corrected for the solid angle of the detectors and for the finite response RC -time of the circuit. The total charge yields are determined by integrating the charge over the full spectrum. Unless otherwise specified, we use the average of the total charge yield for the three 30° -FCs.

To enable depth measurements and to prevent severe target modification by the laser, which would influence the measurements, the target is moved after every 30 pulses. The first pulses on a fresh spot on the target generate signals with a small TOF, indicative of light elements or high-energy tin atoms. Early studies, employing ion energy analyzers, identify these pulses as light elements contaminations [34, 36]. Energy-dispersive X-ray spectroscopy measurements reveal that areas on our tin target unexposed to laser light contain a substantial amount of oxygen and other low-mass elements, such as carbon and nitrogen. These elements are only barely visible, if at all, for an irradiated target area. Therefore, we conclude those fast ion peaks correspond to contamination of the surface by low-mass atoms. To avoid the inclusion of this contamination in the results, spectra and charge yields are considered only after cleaning the surface by the first nine shots. In the experiments, we average over five shots (shots no. 10-14) per target position as well as over 30 separate target positions, i.e. 150 shots in total. Shots later than shot no. 14 are excluded from our analysis to prevent target surface modification effects, which become apparent in the measurement of ion distributions after 20 shots (with a conservative safety margin). We verified that these effects do not change the depth of the hole and confirmed the linear dependence of the depth on the number of shots for the first 30 shots.

Following the charge yield experiments, the target is inspected by means of an optical microscope. The microscope has a 50x imaging objective with a numerical aperture (NA) of 0.42, yielding a depth of focus of $3\ \mu\text{m}$ and enabling the determination of crater depth by straightforward optical inspection of a selected number of holes. The same microscope, equipped with a 5x imaging objective and a motorized stage for automated focus scanning to provide a complete picture of the hole, is used for an automated ablation volume determination by means of the focus variation technique [54] which combines the images acquired by the microscope with computational techniques to provide 3D reconstructions of the ablated sample surfaces. A 2D Gaussian fit to the reconstructed surface profile is performed, and the integral of the fitted curve then provides an estimate of the ablated volume.

2.3 Results & Discussion

Pulse length dependence

Figure 2.2 shows the charge-per-energy signal for two FCs for varying pulse lengths, ranging 500 fs to 4.0 ps. Most of the charge is due to relatively low-energy ions, in the range of 10-100 eV. The peak energy (the energy of the maximum yield) does not substantially change for changing pulse length and is located near 30 eV. Most of the ions are directed backwards with respect to laser beam, i.e. normal to the surface of the target, in line with the model of Anisimov et al. of the ion plume dynamics during laser ablation [25]. The ratio of total charge yield of the 30°-FCs to the yield of the 2°-FC is constant in the investigated pulse length range at a value of 0.14 (see figure 2.3), implying an angular distribution which does not depend on the pulse duration.

Rates of multiphoton ionization processes, in which multiple photons are directly absorbed by a single atom, are heavily dependent on the laser intensity. For laser intensities above $10^{14}\ \text{W}/\text{cm}^2$, multiphoton ionization is dominant in laser ablation [55]. The maximum examined peak intensity in this work is $4.1 \times 10^{13}\ \text{W}/\text{cm}^2$, at a peak fluence of $22\ \text{J}/\text{cm}^2$ and with a pulse length of 500 fs. Therefore, we expect that multiphoton

ionization has a negligible role in the laser ablation and that the ablation and ionization in the surface is dominated by electron impact mechanisms [55]. These mechanisms are dependent on the total energy put in the system and not on the intensity, barring potential larger heat conduction

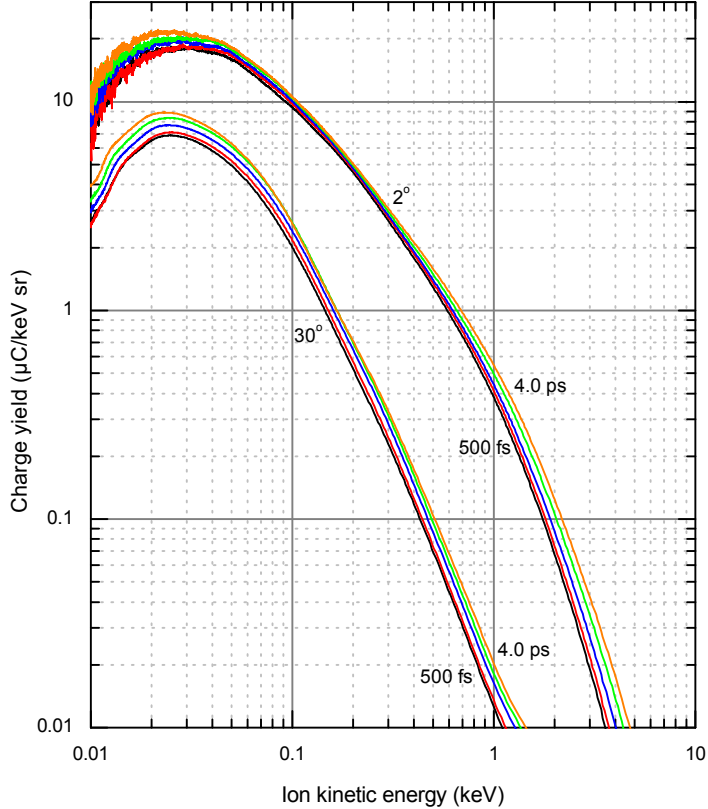


Figure 2.2: Charge yields as a function of the ion energy for the 2°-FC (upper set of lines) and one of the 30°-FCs (lower set of lines). Five pulse lengths are shown: 500 fs (black), 1.2 ps (red), 2.0 ps (blue), 3.0 ps (green) and 4.0 ps (orange). The measurements were performed with a constant peak fluence of 17 J/cm^2 .

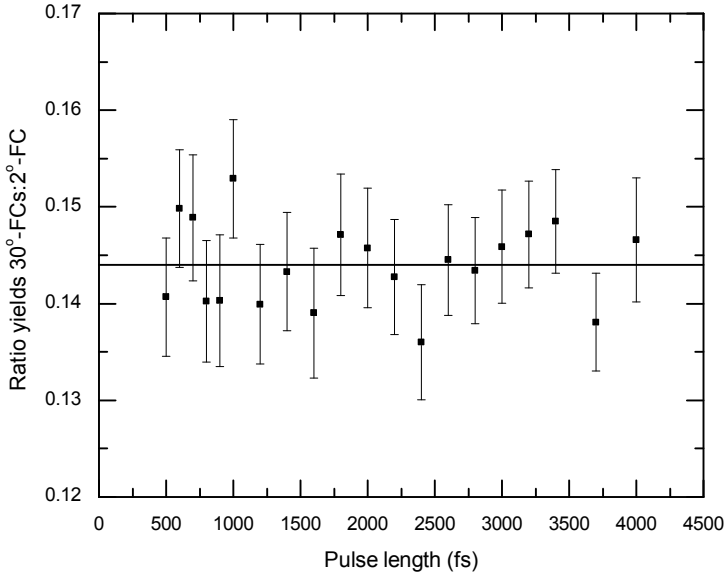


Figure 2.3: The ratio of the yields of the 30°-FCs to the 2°-FC versus the pulse length. The black line depicts the average ratio for all pulse lengths.

losses for longer pulse lengths [37, 56]. The relative insensitivity of our observations to the length of the laser pulse in the studied range confirms that laser intensity itself, at a given fluence, does not play a dominant role.

Figure 2.2 also shows that ion yields increase with pulse length for all ion energies. The upper panel of figure 2.4 shows the total charge collected on the 2°-FC together with the ablation depth for each pulse length. The charge yield increases linearly from $3.2 \mu\text{C}/\text{sr}$ at a pulse length of 500 fs to $3.9 \mu\text{C}/\text{sr}$ at 4.0 ps. In contrast, the ablation depth exhibits the opposite trend. It decreases for increasing pulse length from 2.4 (500 fs) to 2.1 (4.0 ps) $\mu\text{m}/\text{shot}$. However, the ablation volume is constant (see lower panel of figure 2.4), within the measurement uncertainties, because of an increase in hole radius compensates decreasing depth. The increase in accumulated charge does therefore neither have its origin in an increase of ablated material (cf. figure 2.4), nor in a broadening of the angular

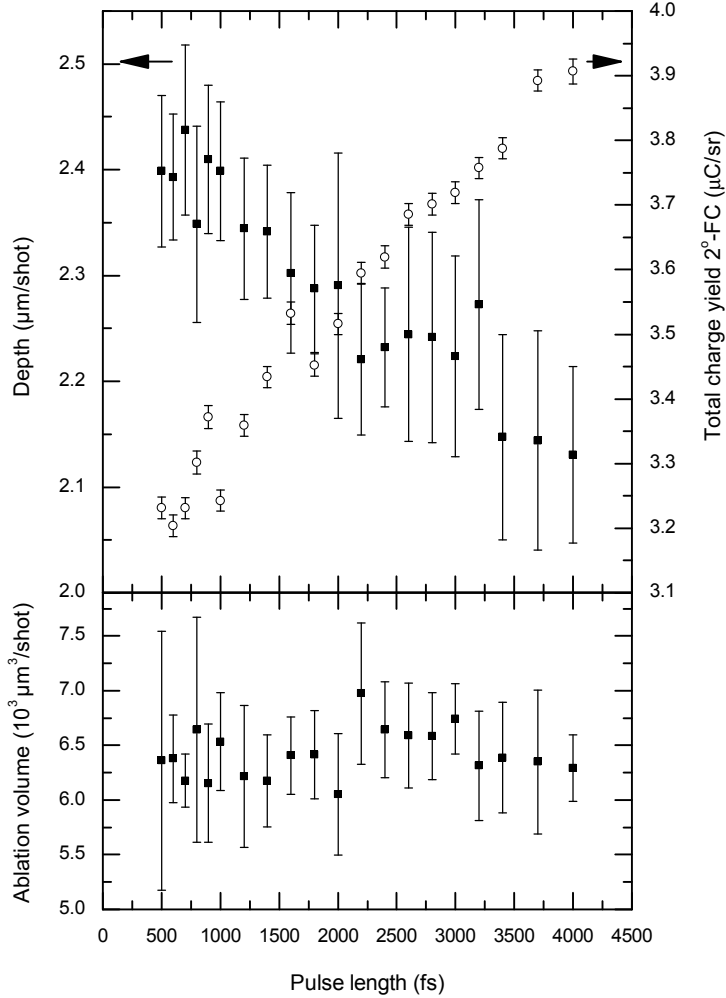


Figure 2.4: (upper) Total charge yield at the 2°-FC (open circles, right axis) and the depth at the center of the holes (closed squares, left axis) as a function of pulse length. The measurements were performed at a constant peak fluence of 17 J/cm². (lower) The ablation volume obtained from the focus variation technique [54] as a function of pulse length at the same constant peak fluence. The error bars indicate 1-standard deviation of the mean on either side. Two data points where no reliable estimation was possible are excluded.

ion distribution (cf. figure 2.3). A possible explanation could be local screening of the laser light by vapor absorption [37, 56]. For longer pulses, more and more ablated material (ions, electrons, and neutral particles) will partially block the target surface from these laser pulses. Instead of ablating the surface, this laser light will be absorbed by the vapor. For gold, Pronko and coworkers [27] used numerical simulations to show that the fraction of laser light absorbed by vapor increases from 0 to almost 20% between 100 fs and 10 ps, respectively. This results in a decrease of the amount of ablated material because part of the laser light does not reach the target, while the vapor may be further ionized.

Concluding, we find that a longer pulse length results in a gradual increase in ionization, but a gradual decrease in the ablation depth at the center. The total amount of ablated material did not change. We observe no indications of a maximum or minimum such as found by Vinokhodov et al. [33, 52]. This could possibly be attributed to the difference in target morphology in the comparison: Vinokhodov reported on results obtained on liquid tin droplets, whereas our work focuses on planar solid tin targets. The angular ion yield distribution is constant in the pulse length range of 500 fs to 4.0 ps. For the observed range, shortening the pulse length results in fewer ions.

Peak fluence dependence

In addition to the pulse duration, experiments for a varying pulse fluence are conducted. These measurements are performed at 1.0 and 4.5 ps pulse length. Figure 2.5 shows the ion spectra at 2° and 30° angle for all examined pulse fluences. The bulk of the ions have low energy, with a broad peak around 30 eV. More charge is collected as the pulse fluence increases for all ion energies. Particularly noticeable is the increase in the yield of high-energy ions. The yield at 40 eV ion energy increases approximately 10 times, whereas that at 400 eV increases by a factor of about 300, comparing the signals on the 2° -FC for the highest (22 J/cm²) and the lowest (2.6 J/cm²) peak fluence (cf. figure 2.5). For the 30° -FCs an additional shoulder at a higher ion energy (several hundred eV) is visible. This shoulder shifts towards higher energies for increasing pulse energy. At the high end of the fluence range the larger low-energy peak attains such heights and widths that the high-energy shoulder becomes indistin-

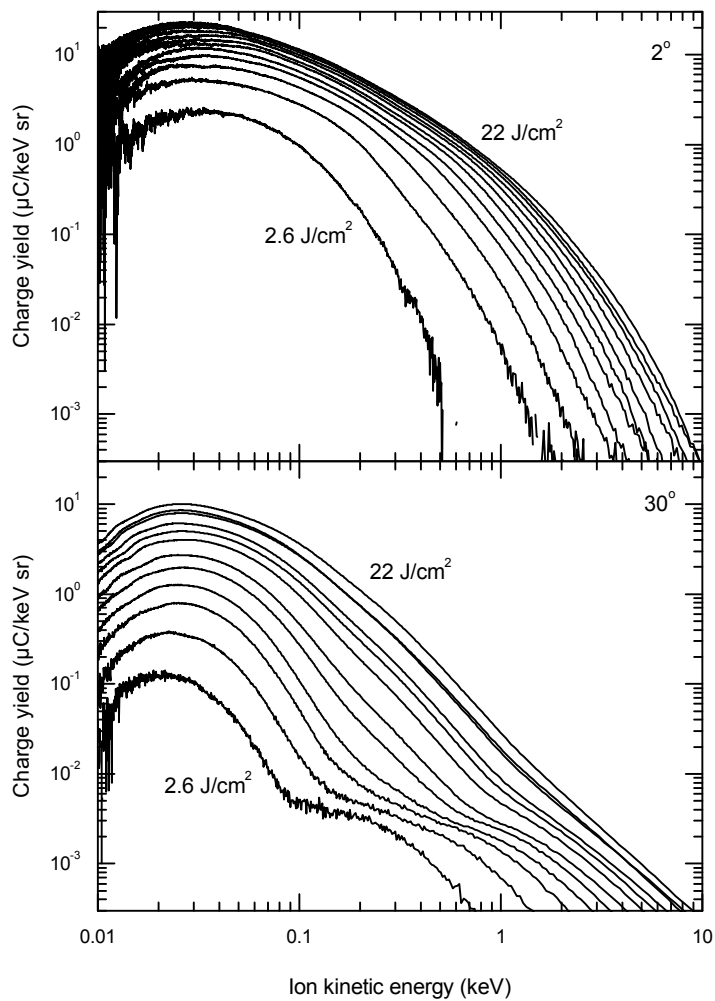


Figure 2.5: Charge yield as a function of the ion energy for the 2° -FC (upper panel) and one of the 30° -FCs (lower panel) for increasing peak fluence, from 2.6 to $22 \text{ J}/\text{cm}^2$ in steps of $1.8 \text{ J}/\text{cm}^2$ at a constant pulse length of 1.0 ps .

guishable from it. This high-energy feature is also visible in other ablation experiments with pulse durations in the fs-ps range [36, 38] and has been ascribed to the occurrence of an ambipolar field, resulting from a space-charge layer formed by electrons above the surface. This field accelerates some of the ions towards higher energies. It increases with temperature and the gradient of electron density [57].

Nolte and coworkers [37] showed that the ablation depth has a logarithmic dependence on the laser fluence for pulse lengths up to a few ps. Typically two regions are present: a low-fluence region, in which the optical penetration of the laser light defines the ablation, and a high-fluence region, in which the electron thermal diffusion is leading. The low-fluence region has a smaller ablation depth than the high-fluence region. The precise location of the boundary between these regions is dependent on the target material and the laser characteristics. In both regions, the depth follows the generic equation [26]

$$D = a \ln \left(\frac{F}{F_{thr}} \right), \quad (2.2)$$

in which D is the ablation depth, a the ablation constant, F the laser fluence and F_{thr} the threshold ablation fluence.

We measured the depth of the hole at its center as a function of the peak fluence (see the upper panel of figure 2.6). For both pulse lengths, the results show a clear logarithmic dependence separated in two regions, with the high-fluence region starting around 6 J/cm². A fit of the results for the low-fluence region shows that, within the uncertainties of the measurements, the ablation constant and threshold are the same for both pulse lengths. The ablation constant is 0.3 μm for both pulse lengths, while the ablation thresholds are 0.44 and 0.38 J/cm² for 1.0 and 4.5 ps, respectively. In the high-fluence region the thresholds are found to be 3.0 and 2.4 J/cm² for 1.0 and 4.5 ps, respectively. Such a decrease of the threshold is in agreement with the numerical simulations of Pronko et al. [27]. The ablation constant is slightly higher for the 1.0 ps case at 1.2 μm, against the 1.0 μm found for 4.5 ps.

These ablation thresholds for tin are similar to those found with a similar experimental approach for iron by Shaheen et al. [43, 58] with 0.23 and 2.9 J/cm² for the low- and high-fluence regions, respectively (for a lower pulse length of 130 fs). In comparison to other metals such as

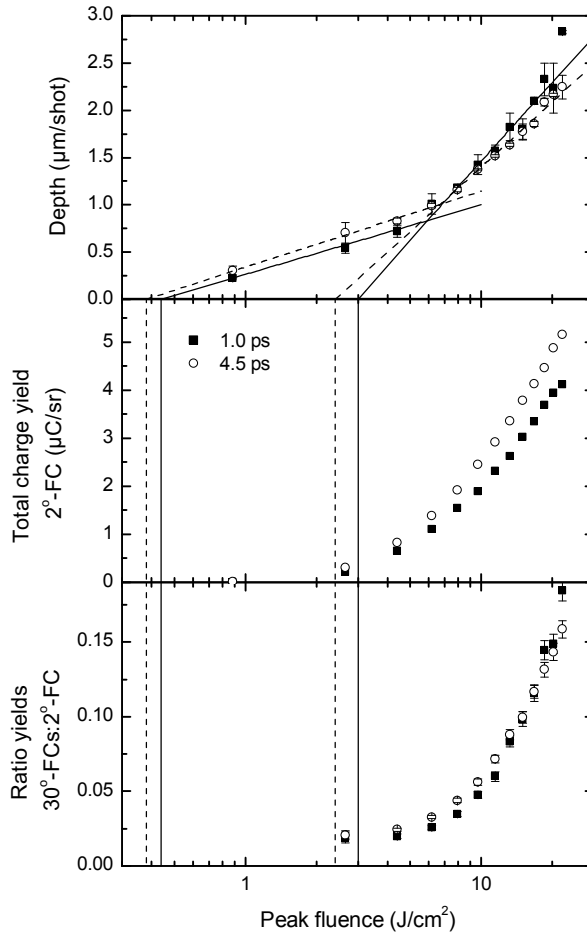


Figure 2.6: (upper) The ablation depth at 1.0 (filled squares) and 4.5 ps (open circles) as a function of the peak pulse fluence. The lines represent fits of equation 2.2 through the data. Points at 6 J/cm² are included in both fit ranges. Thresholds are 0.44 (1.0 ps) and 0.38 J/cm² (4.5 ps) for the low fluence region and 3.0 (1.0 ps) and 2.4 J/cm² (4.5 ps) for the high fluence region. As a reference these thresholds are also shown below (middle) Total charge yields for the 2°-FC at 1.0 (filled squares) and 4.5 ps (open circles). The error bars are smaller than the symbol size. (lower) The ratio of the yields of the 30°-FCs to that of the 2°-FC at 1.0 (filled squares) and 4.5 ps (open circles). The data point at 0.9 J/cm² is omitted due to low signal quality.

gold, silver, aluminum and copper, tin has higher thresholds [34, 37, 39]. The high-fluence threshold of gold, for example, is reported to be 0.9 J/cm^2 at roughly 150 fs [39, 43] and 1.7 J/cm^2 at almost 800 fs [39]. The theoretically expected ablation thresholds are dependent on target properties, such as optical penetration depth, thermal conductivity, and density [37, 39], and laser properties such as the pulse duration [37, 39, 56]. This large parameter space makes our experimental findings particularly valuable, as no straightforward predictions can be made.

The charge yield at the 2° -FC (middle panel of figure 2.6) increases for increasing pulse fluence, from the noise level below 0.1 to 4.1 (1.0 ps) and $5.2 \mu\text{C/sr}$ (4.5 ps). A noticeable difference with the results for the ablation depth is the higher "threshold" above which appreciable ionization is apparent in our measurements. At the lower fluences, the temperature of the surface is too low to generate an observable amount of ions and mostly neutral particles are emitted. Above a certain fluence ions are generated and the charge yield gradually increases above that fluence, following a roughly linear or logarithmic dependence. The charge yield results for both pulse lengths are very similar. In agreement with the above discussed pulse length results, the yield for the 4.5-picosecond pulses is slightly higher. As the charge yield at a certain angle is determined by several factors which are not necessarily constant for the pulse fluence, such as the volume of ablated material, angular distribution, and ionization fraction, there are no clear expectations for the fluence dependence. For these same reasons, a good comparison between studies in the available literature is also difficult to realize. Toftmann and coworkers [34] find a linear dependence for the total yield up to 2 J/cm^2 whereas Amoruso et al. [35, 36] find a logarithmic dependence up to 3 J/cm^2 .

While changing the pulse length does not influence the angular ion distribution, the pulse fluence certainly does. The lower panel of figure 2.6 shows the ratio of the 30° -FC yields to the 2° -FC yield for both pulse lengths. The ratio increases from 0.02 near threshold to almost 0.2 at the highest fluence. At the lower fluences the ratio is fairly constant but it increases rapidly for higher fluences, indicating a rapidly broadening of the angular distribution. There is no appreciable difference between the ratios for the 1.0- and 4.5-picosecond signals.

Following Anisimov's model [25, 57], the angular distribution of the

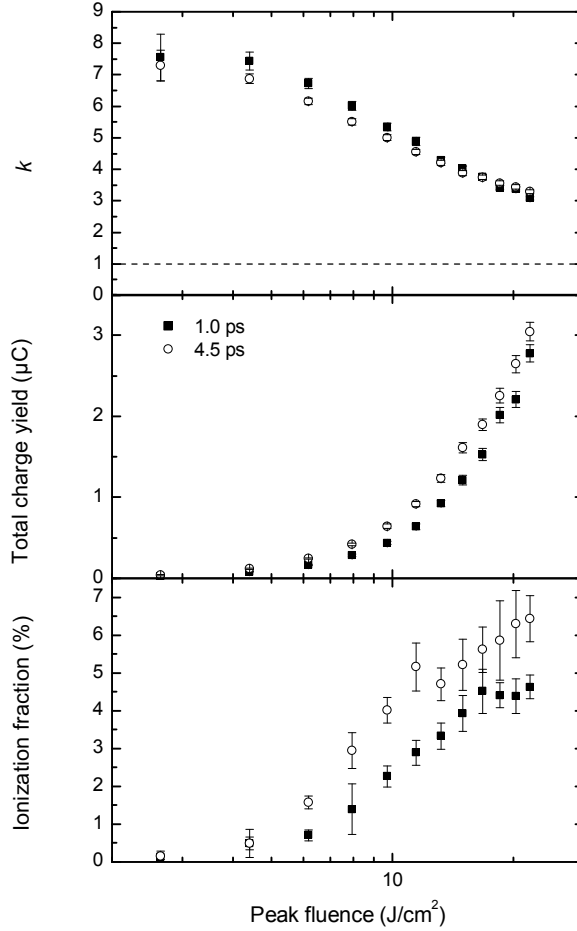


Figure 2.7: (upper) The value of k of the angular distribution (cf. equation 2.3) versus the peak fluence for 1.0 (filled squares) and 4.5 ps (open circles) pulse length. The value of the dashed line represents the value of k for which the distribution is isotropic. (middle) The total charge yield over the whole hemisphere out of the target plane for 1.0 (filled squares) and 4.5 ps (open circles), obtained using k and the total charge yield of the 2°-FC (cf. equation 2.4). (lower) The ionization fraction for 1.0 (filled squares) and 4.5 ps (open circles), obtained with the total charge yield and the ablation volume. The error bars indicate the 1-standard deviation of the mean, as obtained from error propagation (cf. figure 2.6).

plasma vapor from laser ablation in terms of the yield $Y(\theta)$ per unit surface at a certain polar angle θ with respect to the yield at 0° is described by

$$\frac{Y(\theta)}{Y(0)} = \left[\frac{1 + \tan^2(\theta)}{1 + k^2 \tan^2(\theta)} \right]^{3/2}, \quad (2.3)$$

assuming cylindrical symmetry around the target normal and introducing the parameter k . This formula is adjusted to the hemispherical case [57] from the seminal planar surface case [25]. A large value of the scaling parameter k indicates that the angular distribution is sharply peaked in the direction along the target normal, while a k equal to 1 describes a fully isotropic distribution. The values of k can be obtained from the charge yield ratios depicted in figure 2.6 (lower panel) and are plotted in figure 2.7 (upper panel). We find that k decreases from roughly 8 to 3 in the examined fluence range. A similar study on the ablation of silver [34] found similarly large values for k (6.2 and 4.0 depending on the axis of the elliptic spot size) at 500 fs pulse length and a fluence of 2 J/cm². This same study reports values for k between 2 and 3 for ns-pulses, similar to studies of Thestrup et al. in the nanosecond-range [59, 60]. Those studies found a decreasing k for increasing fluence, similar to our findings in the fs-range. Additionally, they generally found that ion distributions from nanosecond-laser ablation are much broader than those of femtosecond-laser ablation. For tin, studies with ns-long pulses indeed found similarly broad angular ion distributions [61, 62].

To obtain the total charge yield Y_{total} of all ions emitted from a pulse in terms of the yield at 0° , and k , we integrate equation 2.3 over the relevant half hemisphere resulting in

$$Y_{\text{total}} = \frac{2\pi Y(0)}{k^2}. \quad (2.4)$$

The results of the total yield are shown in figure 2.7. For the examined fluence range, the total yield increases from near-zero to $\sim 3 \mu\text{C}$, corresponding to 2×10^{13} ions, assuming singly-charged ions. The combination of increasing charge yield measured at the 2° -FC and a broadening angular distribution results in a very rapidly increasing total charge yield. The total charge yield combined with the volume measurements enable

the determination of the ionization fraction, i.e., the amount of elementary charge per atom (see lower panel of figure 2.7). The relation between ablation volume and laser fluence follows from the well-known dependence of the ablation depth on this fluence. The theoretical description for Gaussian pulses, however, is slightly modified [63, 64]. Experiments in the fs-range, on other elements than tin, report ionization fraction values of 1% [34] at 2 J/cm^2 (at 500 fs pulse length) to $\sim 3\text{-}4\%$ [65] at 5 J/cm^2 (50 fs). We find similar values, reaching 5 and 6% in our fluence range for 1.0 and 4.5 ps respectively. This is significantly lower than the ionization fraction of several 10% observed in nanosecond laser ablation (at fluences of $\sim 2 \text{ J/cm}^2$) [57, 59].

2.4 Conclusions

We have studied the influence of two laser parameters on the ion charge yield and energy distribution, as well as the ablation depth and volume. A high-energy ion peak is visible for low fluences, in agreement with the available literature. Variation of the pulse duration from 500 to 4000 fs results in a small increase of the ion charge yield, while the ablation depth decreases slightly. A possible explanation is the screening of the target by the plasma plume. The total ablation volume remains constant. Interestingly, we do not observe the abrupt changes in either depth or ion yield that were hinted at in refs. [33, 52]. The ion yield angular distribution does not change appreciably as a function of pulse length. The ablation depth follows a two-region logarithmic dependence on laser pulse peak fluence, in agreement with the existing theory. We find ablation thresholds of 0.44 (at a pulse length of 1.0 ps) and 0.38 J/cm^2 (4.5 ps) for the low-fluence region and 3.0 (1.0 ps) and 2.4 J/cm^2 (4.5 ps) for the high-fluence region, close to literature values for other metallic elements. The "threshold" at which ionization is apparent is higher, from there on the ion charge yield increases in step with fluence. The angular distribution is sharply peaked backwards along the target normal at the lower fluences, but rapidly broadens for the higher fluences. The total ionization fraction increases gradually and monotonically with the fluence to a maximum of 5-6%, which is substantially lower than typical values for nanosecond-laser ablation. Short-pulse lasers such as those employed in this work

can be utilized to generate a fine-dispersed target for plasma sources of EUV light [33]. We demonstrated that such short pulses produce less fast ionic debris, compared to nanosecond-ablation [57, 59], impacting plasma facing materials. Our results further enable a detailed understanding and optimization of laser parameters with respect to ablated tin mass, ion yield and energy, and emission anisotropies. These results as such are of particular interest for the possible utilization of fs-ps laser systems in plasma sources of EUV light for next-generation nanolithography.

Acknowledgements

We want to thank the Ultrafast Spectroscopy group of professor Huib Bakker at AMOLF Amsterdam for the opportunity to use the IRIS laser system and their laboratory. Furthermore we would like to thank the AMOLF and ARCNL workshops and technicians for the aid provided during the experiments. S.W. acknowledges funding from the European Research Council (ERC-StG 637476).

Chapter 3

Sn ion energy distributions from laser produced plasmas¹

The ion energy distributions measured in chapter 2, and newly-measured distributions for picosecond pulses on droplets and nanosecond pulses on solid targets are investigated to determine the driving plasma expansion mechanisms. The energy distributions are compared to existing models using a hydrodynamic approach. For picosecond pulses there is a good agreement for the experimental distributions with the solution of a semi-infinite simple planar plasma configuration with an exponential density profile, both for a solid as a droplet target. The distributions from ns-long pulses agree, however, more with the solution for a mass-limited model and a Gaussian-shaped initial density profile.

¹A. Bayerle, M.J.Deuzeman, S. van der Heijden, D. Kurilovich, T. de Faria Pinto, A. Stodolna, S. Witte, K.S.E. Eikema, W. Ubachs, R. Hoekstra, O.O. Versolato, Plasma Sources Sci. Technol., **27**, 045001 (2018)

3.1 Introduction

Plasma expansion into vacuum is a subject of great interest for many applications ranging from ultracold plasmas [66, 67] over laser acceleration [68, 69] to short-wavelength light sources [11, 70]. For such light sources driven by laser-produced plasmas (LPPs) the optics that collect the plasma-generated light are exposed to particle emission from the plasma. The impinging particles may affect the performance of the light-collecting optics.

Charged particles from LPPs can be monitored by means of Faraday cups (FCs) - a robust plasma diagnostics tool. Faraday cups can be used to characterize the angular distribution of ion emission of metal and non-metal LPPs [34, 60]. Faraday cups in time-of-flight mode can be used to measure the energy distributions of the ions emanating from the plasma interaction zone [38, 62, 71]. Because of its relevance to extreme ultraviolet nanolithography, LPP of Sn has been subject to similar studies, in which the kinetic energy and yield of the Sn ions together with extreme-ultraviolet light output is characterized [72]. Indications of a set of laser parameters was reported for which a dip in the Sn ion yield might occur [52]. Both droplet and planar targets have been investigated [73] but no unique optimal conditions have been found so far (see also chapter 2).

In order to understand the ion energy distributions from LPPs, a theoretical framework based on hydrodynamic expansion has been established early on [25, 74]. The theoretical framework has been expanded ever since. Nevertheless, benchmarking the energy distribution functions derived in the different studies with experimental data on LPPs remains scarce. To the best of our knowledge only two groups report the comparison of the results of hydrodynamics models to ion energy distributions measured by FCs [57, 75].

Laser-produced plasmas can be created over a vast space of laser and target parameters. Here we address the energy distributions of emitted ions in a substantial subset of this space, namely pulse lengths ranging from sub-ps to almost 10 ns and laser peak fluences up to 3 kJ/cm². The plasma is produced on solid-planar and liquid-droplet targets irradiated by infrared lasers. The measured results are used to benchmark two analytical solutions of hydrodynamics models of plasma expansion into vacuum [75, 76]. The intended accuracy of this comparison between theory and our

experiments is not expected to be able to discern any effects beyond those predicted by these single-fluid single-temperature hydrodynamic plasma models, such as the possible presence of a double layer [76, 77, 78]. First, the solution to a semi-infinite simple planar model assuming an exponential density profile of the plasma [76] shows good agreement with the experimental results of LPP by ps-laser pulses. Second, the ion energy distributions obtained by exposing solid Sn targets to 6-ns laser pulses agrees best with the solution to a modified hydrodynamics model [75]. In that work, a different density evolution of the expanding plasma is derived, starting out from a Gaussian density profile instead of the exponential profile used in the work of Mora [76]. In addition, the modified model takes into account the dimensionality of the plasma expansion.

In section 3.3 the experimental setups used to produce Sn plasmas by pulsed lasers are described. The ion energy distributions are shown in section 3.4. We compare the ion energy distributions with the results of theoretical studies on plasma expansion into vacuum which are briefly reviewed in the following section 3.2.

3.2 Theoretical models

Plasma expansion into vacuum traditionally is treated by a hydrodynamic approach [74]. A typical initial condition consists of cold ions with a charge state Z and a hot gas of electrons with energies distributed according to Maxwell-Boltzmann [79]. The electron cloud overtakes the ions during expansion leading to an electrostatic potential that accelerates the ions. The hydrodynamic equations of plasma expansion can be solved by a self-similar ansatz with the coordinate $x/R(t)$, where x is the spatial coordinate and $R(t) = c_s t$ [76] or $R(t) \propto t^{1.2}$ [75] is the characteristic system size growing with the sound speed c_s . Many theoretical studies that are based on such a hydrodynamics approach solve the problem of plasma expansion into vacuum by making different assumptions, for example isothermal or adiabatic expansion [80] or a non-Maxwellian distribution of the electrons [81, 82]. Here we focus on two studies published by Mora [76] and Murakami *et al.* [75] where we assume that the charge state Z can be interpreted as an average charge state. This presents a strong simplification especially in our rapidly expanding laser-driven plasma containing

multiply charged ions (e.g., see refs. [83, 84]). Our FC technique cannot resolve ions by their charge and the measured distribution is in fact a convolution of distributions of ions of the various charge states. These energy distributions may be expected to depend on charge state Z (see, e.g., refs. [77, 85]) and the collected charge on the FC is Z times the amount of ions captured.”

Nevertheless, it is instructive to compare the charge-per-ion energy distributions measured on FCs with the solutions to these single-fluid single-temperature hydrodynamic plasma models in terms of emitted particle number per energy interval. In Mora [76] the particle energy distribution is found to be

$$dN/dE \propto (E/E_0)^{-1/2} \exp\left(-\sqrt{E/E_0}\right), \quad (3.1)$$

while Murakami *et al.* [75] derives

$$dN/dE \propto \left(E/\tilde{E}_0\right)^{(\alpha-2)/2} \exp\left(-E/\tilde{E}_0\right), \quad (3.2)$$

under inclusion of higher dimensionality α and Gaussian evolution of the density.

The respective ion energies are characterized by E_0 or \tilde{E}_0 . The characteristic energy depends on the charge state Z of the ions and the electron temperature T_e . In the first equation the characteristic ion energy E_0 is given by

$$E_0 = Zk_B T_e, \quad (3.3)$$

with k_B the Boltzmann constant. The ion energy in equation 3.2 is given by

$$\tilde{E}_0 = m\dot{R}^2(t)/2 = 2Zk_B T_e \ln(R(t)/R_0), \quad (3.4)$$

with m the ion mass and R_0 the initial size. A higher E_0 or \tilde{E}_0 mean there are relatively more high-energy ions, with a higher mean charge state and a higher electron temperature.

Both models assume Boltzmann-distributed electron energies and isothermal expansion of the plasma. Additionally, in ref. [75] the solution (our equation 3.2) is extended and smoothly connected with a solution of an adiabatically expanding plasma. The resultant ion energy spectrum is given in the same form as our equation 3.2 only with a slight modification

in the characteristic energy scale $\tilde{E}_0 \rightarrow f\tilde{E}_0$. For simplicity, we use the solution in their first step to analyze our experimental results.

One essential difference between the two models is the functional form of the density evolution of the expanding plasmas. In ref. [76], the charge density is obtained as a perturbation of the initial charge density, which then evolves as $n \propto \exp(-x/R(t))$ (see also ref. [86]). In ref. [75] the authors argue that for longer pulse lengths or limited target masses this perturbation assumption is not valid. They obtain a Gaussian form for the charge density profile [87, 88]: $n \propto \exp(-(x/R(t))^2)$. This density profile results in a different high-energy tail of the ion distribution. The dimensionality is captured by the parameter α . If $\alpha = 1$, the expansion is planar otherwise the expansion is cylindrical or spherical for $\alpha = 2$ and $\alpha = 3$ respectively.

3.3 Experimental setup

We use two setups to create laser-produced plasmas of Sn and measure the energy distributions of the emitted ions. Figure 3.1a. shows the schematic representation of the setups. The first setup contains a solid Sn plate of 1 mm thickness as a target. In the second experiment the targets are free falling droplets of molten Sn with a diameter of $30 \mu\text{m}$. The solid and droplet targets reside in vacuum apparatuses with base pressures below 10^{-6} mbar. Pulsed infrared laser beams are focused on the targets to create the plasma. The ion emission is collected by FCs mounted into the vacuum apparatus around the plasma.

The custom-made FCs consist of a cone shaped charge collecting electrode mounted behind a suppressor electrode (see chapter 2). Both electrodes are housed in a grounding shield. The FCs have an opening of 6 mm diameter and are mounted at a distances between 25 cm and 75 cm. The collector and suppressor are biased to a negative potential with respect to ground in order to prevent plasma electrons from entering the cup, and secondary electrons from leaving the cup after Sn ions impinge on the surface of the collector.

Faraday cup measurements can only serve to give an approximation of the plasma flow as the separation of electrons from the ions in the quasi-neutral expansion of the plasma cannot be assumed to be complete and

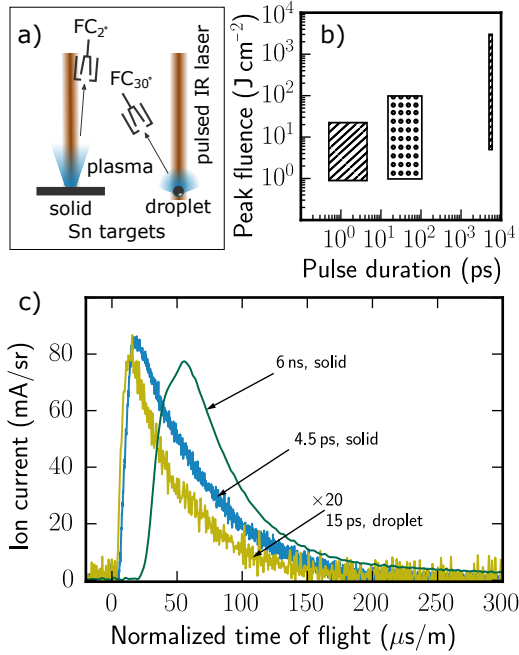


Figure 3.1: a) Schematic of the experimental setups. The plasma is created by exposing Sn metal targets to focused infra-red laser pulses. The Sn target has either planar geometry (solid target) or consists of droplets of $30\ \mu\text{m}$ diameter. The ion emission is collected by Faraday cups (FC) that are roughly 1 m away from the plasma source. b) Pulse duration and peak fluence parameter space addressed by the experiments. Hatched rectangles show the parameter space explored using solid targets. The parameter space explored on Sn droplets is shown by the dotted rectangle. c) Typical examples of time dependent ion traces collected by the FCs. The x-axis is normalized to a time-of-flight distance of 1 m. The targets are exposed to fluences of $25\ \text{J}/\text{cm}^2$ (solid target) and $30\ \text{J}/\text{cm}^2$ (droplet target)

may depend on the set bias voltages and earth magnetic fields [89]. We verified that further increasing the bias voltages had no significant impact on the measured time-of-flight traces. The earth magnetic field is only

expected to influence the detection of low-energy ions.

Figure 3.1c shows typical time-of-flight traces acquired by the FCs during experimental runs. The ion current is measured across a shunt resistor with a digital storage oscilloscope. The traces are averaged for the same laser fluence for about hundred laser exposures. The ns-laser produced traces have a lower noise amplitude, because the traces are averaged for about two hundred exposures. The shunt resistor of 10 k Ω and the added capacitance of 220 pF of the collector cup and the cable to the oscilloscope form an RC-network that limits the bandwidth of the measurement. The effective RC-time of the read-out is on the order of 2 μ s. In order to retrieve the ion current from the raw data we correct for the response function of the read-out network. The ion traces can be integrated in time to obtain the total charge emitted into the direction of the corresponding FC. The energy distribution can be calculated by the following transformation

$$dQ/dE = t^3 I(E)/mL, \quad E = mL^2/2t^2, \quad (3.5)$$

with m the mass of Sn, L the distance between the plasma and the detector and t the time-of-flight. The charge yield per energy interval is averaged over bins of 10 eV.

As shown in Fig. 3.1c, the time-of-flight traces for pulses below 15 ps have a smaller signal-to-noise ratio. The traces converge to the background noise level at 170 μ s/m. This time-of-flight is equivalent to an energy of 20 eV. Therefore we truncate the energy distributions below 20 eV.

The setup containing the droplet target is described in detail by Kurilovich *et al.* [90]. The Sn droplets are created by pushing liquid Sn through a piezo-driven orifice. Orifice diameter and piezo driver frequency determine the diameter of the droplets to 30 μ m. A pulsed 1064-nm Nd:YAG laser is focused to a 100 μ m full width at half maximum (FWHM) Gaussian spot at the position of the droplet stream. Faraday cups are added at 37 cm under angles of 30 $^\circ$ and 60 $^\circ$ with respect to the incoming laser beam to enable time-of-flight measurements.

The second setup containing the solid target is described in detail in chapter 2. The solid target is mounted onto a 2D-translation stage (PI miCos model E871) enabling a computer-controlled, stepwise motion of the target between laser pulses in perpendicular direction to the laser beam. The stepwise translation of the target between pulses is necessary

to prevent the ion emission to change because of surface deformation after too many laser shots on the same spot. Also, the first few laser pulses on a new spot on the surface ablate the oxide layer and the subsequent laser pulses produce plasmas containing mostly Sn [91]. Two laser systems are employed to create plasma at the Sn solid surface. First, a 800-nm wavelength Ti:sapphire laser is used to generate pulses of 0.5 ps to 4.5 ps duration. The Gaussian spot size of the the 800-nm laser at the surface of the target is $100\ \mu\text{m}$ FWHM. Second, a Nd:YAG laser outputs 6-ns long pulses. This laser has a wavelength of 1064 nm and is focused to a Gaussian spot of $90\ \mu\text{m}$ FWHM. The setup is equipped with three FCs, one at a distance of 73 cm and at an angle of 2° from the surface normal, and two at $\pm 30^\circ$ at distances of 26 cm and 73 cm.

We summarize the laser parameter space accessible with the lasers in Figure 3.1b. The peak fluence and pulse duration used in the experiments performed on a solid target are shown as hatched rectangles. The Ti:sapph laser produces ultrashort pulses ranging from 0.5 ps to 4.5 ps without evidence for intensity-induced self-focusing or self-phase modulation effects. Peak pulse energy densities run up to $30\ \text{J}/\text{cm}^2$. The pulse length of the Nd:YAG laser used on the solid target is 6 ns and the pulse energy densities reach $3\ \text{kJ}/\text{cm}^2$. The dotted rectangles shows the parameter space for the experiments on droplets. The Nd:YAG laser employed in the droplet setup is capable of producing ultrashort pulses between 15 ps and 105 ps duration and peak fluences of 1 to $100\ \text{J}/\text{cm}^2$

3.4 Results and discussion

First we present the energy distributions of the Sn ion emission for three different pulse lengths and same energy density of the laser and show that the experimental data can be well described by the self-similar solutions of the hydrodynamic model. Second, we show the ion distributions obtained for different laser fluences and for fixed pulse durations.

3.4.1 Changing pulse duration

We measure the ion energy distributions on the different target geometries with the following laser parameters. The solid target is irradiated by 6-ns,

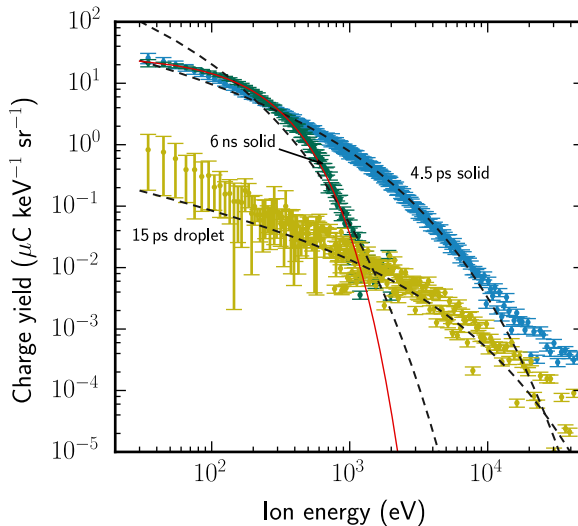


Figure 3.2: Charge energy distributions measured for different pulse durations of the laser on both solid-planar and liquid-droplet targets. The energy density of the laser pulses is $25 - 30 \text{ J/cm}^2$. The dashed (black) lines show the fits of equation 3.1 to the distributions. The solid (red) line is a fit of equation 3.2 with $\alpha = 2$ to the data.

1064-nm and 4.5-ps, 800-nm pulses with a peak fluence of 25 J/cm^2 and the Sn droplets are exposed to 15-ps and 105-ps pulses with a peak fluence of 30 J/cm^2 and 1064 nm wavelength. The presented ion energy distributions are measured under different angles for the two target geometries. Ion emission from the solid target is measured at 2° (and 30° , see chapter 2) with respect to the surface normal, while the droplet target emission is collected by the FC mounted at an angle of 30° from the laser axis. Because most (and most energetic) ions are emitted along the surface normal [84, 92, 93] the ion emission in the 30° direction from the spherical droplet target (thus emitted along a surface normal) is best compared to the ion emission in the small-angle, 2° direction from the planar target. In this comparison we note that the projection of the laser beam onto the droplet surface at a 30° angle-of-incidence will reduce the local fluence by the cosine of this angle. The absorption, governed by the Fresnel

equations, also depends on this angle. Both effects, however, have minor impact considering the relatively small angle involved and, in fact, these two effects partially cancel each other (see, e.g., ref. [94]). The difference in the reflectivities between solid and liquid tin before laser impact is quite small at 2 percentage points, comparing 82 to 84%, respectively (taking as input the works of refs. [95, 96]). At our typical energy fluences, however, the solid target is practically instantaneously melted and heated to several thousand degrees (within the skin layer). Thus, the target reflectivity, identically for both solid planar and liquid droplet cases, is determined by the optical properties of liquid and vaporized tin at $T \sim 3000\text{ K}-5000\text{ K}$ that are poorly known and quite different from those at room temperature.

Figure 3.2 shows the ion energy distributions of the LPPs obtained with the laser parameters described above. In all cases the charge yields decrease monotonically with ion energy. Charge yields obtained from pulses below 6-ns duration converge and hit the detection threshold around an ion energy of 30 keV. Long laser pulses of 6 ns produce charge yields that roll off already at 1 keV at a faster rate.

For ps-pulses the charge yield retrieved from the solid target is more than an order of magnitude higher than from the droplet target for energies below 5 keV. For the solid target we acquire a total charge of about $4\ \mu\text{C}/\text{sr}$ and $3\ \mu\text{C}/\text{sr}$ for 4.5-ps and 6-ns pulse length, respectively. The droplet target yields a total charge of only $0.06\ \mu\text{C}/\text{sr}$ when exposed to the 15-ps laser pulse. We attribute this difference between collected charge to the smaller droplet diameter compared to the focused laser beam diameter. While the solid target is irradiated by a full Gaussian intensity profile, the droplet is exposed to only a fraction of the focused laser beam energy because the diameter of the droplet is three times smaller than the FWHM of the beam. The energy deposited on the droplet can be calculated by integrating the Gaussian beam fluence profile over the droplet. Then the energy on the droplet is $E_d = E_L(1 - 2^{-d_D^2/d_L^2})$ with d_D the droplet diameter, E_L and d_L the total laser energy and the FWHM diameter of the focused laser beam. For our experimental parameters the droplet is exposed to only 6% of the total laser energy and thus the observed total charge yield will be substantially smaller than from the solid target.

The energy distributions of figure 3.2 are compared with the theo-

retical predictions discussed above. The dashed (black) lines show the least-squares fitted energy distributions according to equation 3.1 for pulse lengths of 4.5 ps and 15 ps. The experimental energy distributions agree well with equation 3.1 for both target geometries and slightly different wavelengths. Applying the model comparison yields the characteristic ion energy E_0 . For the 4.5-ps LPP we obtain $E_0 = 250(30)$ eV.

Model comparisons of the energy distributions of Sn ions emitted from the droplet target give higher characteristic energies. The plasma produced by the 15-ps laser pulses with 30 J/cm^2 energy density yields $E_0 = 970(120)$ eV. This higher characteristic energy could well be the result of the irradiation of the droplet by only the central fraction of the laser beam where the fluence is highest. The droplet is exposed to the central 6% of the total laser energy, therefore the average fluence is close to the peak fluence and thus exceeds the one on the solid target.

Irradiating the solid target surface with the 6-ns laser pulses produces an energy distribution that does not agree with equation 3.1 as illustrated in figure 3.2 by the dashed (black) line. The fit of equation 3.2 to the measured energy distribution is shown as a solid (red) line in figure 3.2. The dimensionality parameter is set to $\alpha = 2$ and with a characteristic ion energy of $\tilde{E}_0 = 150(15)$ eV, the model agrees well with the measured distributions.

The energy distributions of LPP Sn ions are reproduced well in the energy interval of 20 eV to 20 keV, although the target geometries and pulse durations vary significantly. Laser produced plasmas of ps-pulses show good agreement with equation 3.1, and can thus be modelled by the approach of Mora [76]. Between 100 ps and 6 ns pulse duration the ablated target material starts to absorb the laser energy and the density profile deviates from $\rho \propto \exp(-x/R(t))$. In this case we cannot expect equation 3.1 to fit the data. Instead, the experimental energy distribution for the 6-ns laser produced plasma is well described by equation 3.2.

In the following, we focus on the study of the applicability of the two introduced models over the measured range of laser energy densities.

3.4.2 Changing laser energy density

In the following we explore the applicability of the two models to ion energy distributions obtained from LPPs at different energy densities of the

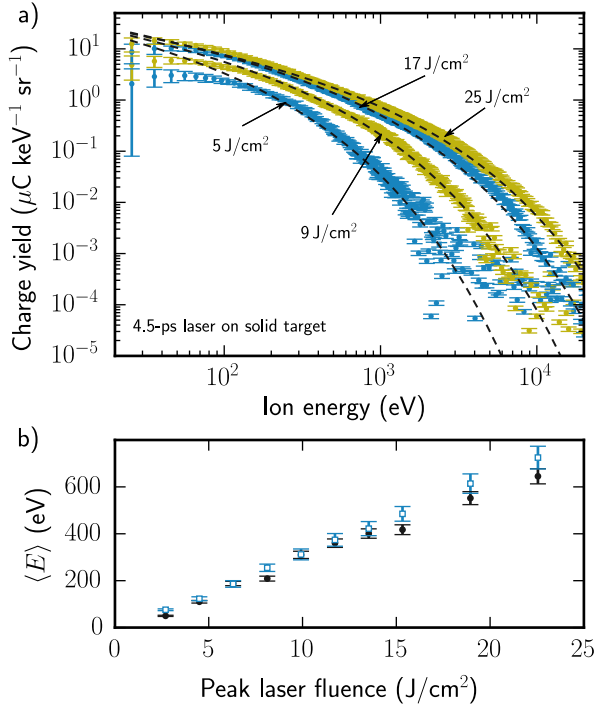


Figure 3.3: (a) Charge energy distributions for a pulse duration of 4.5 ps and different laser energy densities on the solid target, and fits with equation 3.1. (b) The values for $2E_0 = \langle E_{\text{fit}} \rangle$ (solid, black circles) obtained from the fits with equation 3.1 for these distributions, with $\langle E_{\text{exp}} \rangle$ (open, blue squares).

laser and fixed pulse durations.

The solid target is exposed to 4.5-ps pulses from the Ti:sapph laser with different energy densities. The resulting charge energy distributions are shown in figure 3.3a. The four plots on the top are acquired by the FC at 2° . These energy distributions are fit with equation 3.1 and shown as dashed (black) lines. It is informative to compare also the average kinetic energies obtained from the fits $\langle E_{\text{fit}} \rangle$ to those obtained directly from the data $\langle E_{\text{exp}} \rangle$ enabling to judge how accurately the theories describe the experiments. The average energy $\langle E_{\text{fit}} \rangle = 2E_0$ and $\langle E_{\text{fit}} \rangle = \tilde{E}_0/2$ for $\alpha = 1$

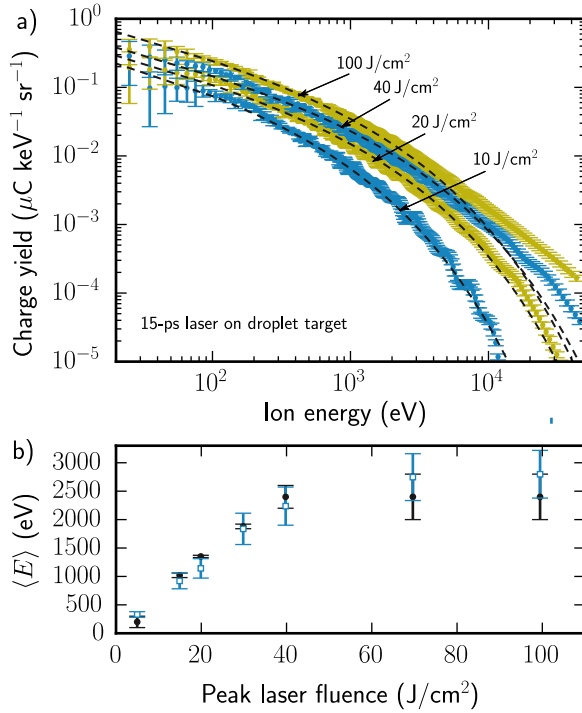


Figure 3.4: (a) Charge yield distributions for different energy densities of the laser on the Sn droplets and fits with equation 3.1. (b) The values for $2E_0 = \langle E_{\text{fit}} \rangle$ (solid, black circles) obtained from the fits with equation 3.1 for these distributions, with $\langle E_{\text{exp}} \rangle$ (open, blue squares).

can be obtained from equations 3.1 and 3.2 analytically but a correction related to the low-energy, 20 eV cut-off needs to be applied to the values $\langle E_{\text{exp}} \rangle$. The corresponding correction factor ranging from 1.2 to 1.6 is obtained by comparing the energy averages of equations 3.1, 3.2 from zero to infinity and from 20 eV and infinity. The correction factor is applied to $\langle E_{\text{exp}} \rangle$ in the following. We find good agreement between the obtained values as presented in figure 3.3b.

Exposing the droplets to ultrashort pulses of 15 ps duration results in similar energy distributions as for the solid target. Figure 3.4a shows the distributions for increasing energy density of the laser pulse. The dis-

tributions are fit with equation 3.1 and plotted as dashed (black) lines. The agreement between the experimental distributions and the model is good for ion energies below 10 keV. For high energy densities of the laser ($>20 \text{ J/cm}^2$) equation 3.1 underestimates the amount of ions with energies above 10 keV. Again, the characteristic ion energies are plotted in dependence of the peak laser fluence in figure 3.4b. Below peak fluences of 40 J/cm^2 of the laser the characteristic ion energies increase. At higher peak fluence (100 J/cm^2) the fit misses the high-energy tail of the distribution. As a result, the value for E_0 obtained from the fit appears to saturate at 1.2 keV. We find good agreement between the obtained values $\langle E_{\text{exp}} \rangle$ and $\langle E_{\text{fit}} \rangle$ (see figure 3.4)

The charge distributions change significantly when we use the 6-ns instead of the ps-laser pulses to produce the plasma. Figure 3.5a shows the energy distributions derived from the time-of-flight traces of the ions emitted from the solid target at an angle of 2° . The distributions are measured at peak fluences of the laser pulses ranging from 23.5 J/cm^2 to 3 kJ/cm^2 . Fitting the distributions with equation 3.2 requires to set an appropriate dimensionality parameter α . The parameter is determined by the ratio of the typical plasma flow length scale and the size of the laser spot size [75]. In our experiments this length scale and laser focus are of similar size and thus the choice of the dimension is not straightforward. We find that setting $\alpha = 1$ or 2 gives satisfactory agreement with the obtained data in the following. To determine the actual dimensionality of the expanding plasma, further measurements are required over a range of laser spot sizes with a multi-angle and charge-state-resolved approach. With the dimensionality parameter set to $\alpha = 1$ the energy distributions produced by pulses of laser fluences between 80 J/cm^2 and 1.6 kJ/cm^2 are fit with equation 3.2. Examples of the fit with equation 3.2 and $\alpha = 1$ to the energy distribution are shown as solid (red) lines in figure 3.5a. For $\alpha = 2$ the fit is illustrated by the dashed (red) lines. The energy distributions obtained with laser fluences below 80 J/cm^2 both $\alpha = 1$ and $\alpha = 2$ produce good agreement with equation 3.2. The ion energy distribution shows a flat response below 50 eV, which is better captured by choosing $\alpha = 2$. At peak fluences above 2.4 kJ/cm^2 the energy distributions feature a “shoulder” around an energy of 6 keV that is not reproduced by equation 3.2.

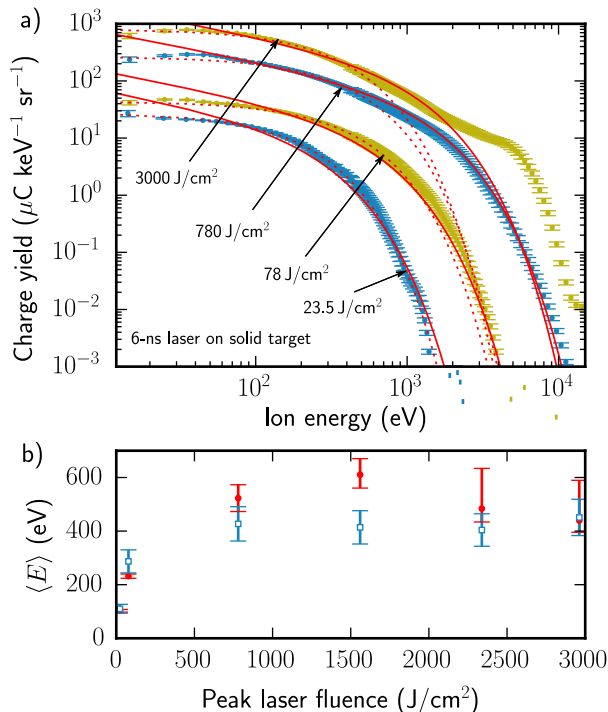


Figure 3.5: (a) Charge yield distributions for different peak fluences on the solid target and fits with equation 3.2 and $\alpha = 2$ dashed (dark-red) lines, $\alpha = 1$ solid (red) lines. (b) The values for $\langle E \rangle$ are obtained from the fits with equation 3.2 for these distributions. Closed (red) circles correspond to $\tilde{E}_0 = \langle E_{\text{fit}} \rangle$ for $\alpha = 1$, along with $\langle E_{\text{exp}} \rangle$ (open, blue squares). Obtained values for \tilde{E}_0 for $\alpha = 2$.

Figure 3.5b shows the average energies of ions $\langle E_{\text{fit}} \rangle = \tilde{E}_0/2$ for $\alpha = 1$ obtained from fitting the data to equation 3.2 as solid (red) circles. The open (blue) squares show the average energies obtained from the experimental data. The characteristic ion energies follow a non-linear trend saturating at a peak fluence of 1.6 kJ/cm^2 . Then, at a higher peak fluence the fit becomes inaccurate because of the abundance of ions with energies above 6 keV. At the lower fluences, we obtain reasonable agreement between the values $\langle E_{\text{exp}} \rangle$ and $\langle E_{\text{fit}} \rangle$ (see figure 3.5).

Our comparisons between theoretical and measured charge-integrated energy distributions show that over a wide range of peak fluences the results of Mora [76] and Murakami *et al.* [75] can be employed to characterize ion emission of LPPs. Care should be taken when laser pulses of high peak fluence are used to create LPPs. Under such conditions, the energy distributions exhibit an abundance of charges at high energies. Especially for the 6-ns pulses with energies $> 2.6 \text{ kJ/cm}^2$ the distribution shows a peak that cannot be reproduced by either of the two model descriptions.

3.5 Conclusion

We present the ion distributions of LPPs for droplet and planar targets for various laser pulse lengths and energies and compare them with the predictions of two results of hydrodynamic models. The charge-integrated energy distributions of ions are well explained by theoretical predictions of refs. [75, 76]. The ion energy distributions fit well the energy distributions found by Mora [76] when the plasma is produced by laser pulses below 100 ps. In contrast, laser pulses of 6 ns duration produced expanding plasmas with ion energy distributions that can be fit by the findings of Murakami *et al.* [75]. The essential difference of the expansion of plasma produced either by ultrashort pulses or ns-long pulses lies in the density evolution of the plasma during expansion. Ultrashort pulses produce plasma with an exponentially decaying density. While ultrashort pulses are off when the produced plasma expands, the ns-long pulse continues to heat the disintegrated target during part of its expansion. The density of the plasma generated in this way has a Gaussian shape, and the pressure of the plasma decreases in time. The two types of plasma expansions from LPPs may be studied in future to clarify this dynamical behavior in the transition regime by producing plasma with laser pulses between 100 ps and 6 ns.

Fitting the theoretical findings to the experimental energy distributions provides a characteristic ion energy of the expanding plasma. By performing additional charge-state resolved measurements the actual electron temperature of the plasma, as in equation 3.3, may be determined. Charge state resolving ion energy spectrometry not only will enable the determination of the electron temperature, but may point at why the the-

oretical predictions fail to explain an abundance of high energy ions when the plasma is produced by high-peak-fluence laser pulses.

The findings of our work show that relatively simple models are sufficient to explain measured ion energy distributions of the LPPs studied here. The understanding of ion emission of expanding plasmas is an important step to assess optics damage in short-wavelength light sources.

Acknowledgement

We thank M. Basko for fruitful discussions. This work has been carried out at the Advanced Research Center for Nanolithography (ARCNL), a public-private partnership of the University of Amsterdam (UvA), the Vrije Universiteit Amsterdam, the Netherlands Organisation for Scientific Research (NWO) and the semiconductor equipment manufacturer ASML.

Chapter 4

Interactions of energy-, charge-state-, and mass-selected tin ions with solid surfaces

Ions, atoms, and electrons are emitted during ion-surface interactions. The first part of this chapter describes the basics of interactions near, at, and in the surface when an ion collides with it. As we detect emitted ions and electrons in our experiments, the emphasis is on interactions which emit these particles. The second part of the chapter describes the ion source and the experimental setup used for ion-surface interaction experiments in Groningen, and includes test experiments on low-energy electrons. The last part of the chapter is about an ion-surface interaction simulation package, SRIM, which is used in this work.

4.1 Atomic interactions

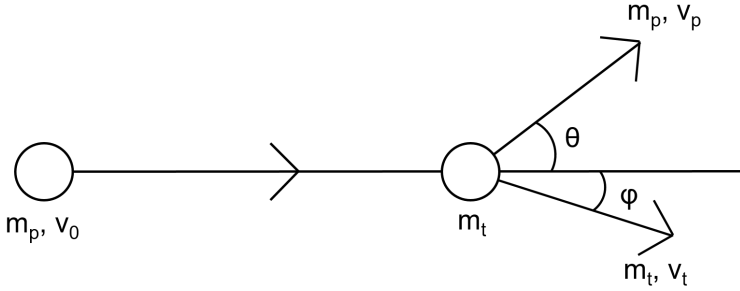


Figure 4.1: Sketch of an elastic collision between two atoms. The energy transferred from one atom to another is determined by the atomic masses and the scattering angle θ .

4.1.1 Scattering

When a moving atom or ion collides with an atom at rest, a part of its kinetic energy will be transferred and the atom will get an angle change, the *scattering angle* θ . For an elastic collision (figure 4.1), the energy transfer and scattering angle can be determined from the conservation laws of energy and momentum:

$$\frac{m_p v_0^2}{2} = \frac{m_p v_p^2}{2} + \frac{m_t v_t^2}{2} \quad (4.1)$$

$$m_p v_0 = m_p v_p \cos(\theta) + m_t v_t \cos(\varphi) \quad (4.2)$$

$$0 = m_p v_p \sin(\theta) + m_t v_t \sin(\varphi). \quad (4.3)$$

The mass of the projectile ion (m_p) and of the target atom (m_t) dictate, for every scattering angle, the ratio of the final (E_f) to the initial (E_0) kinetic energy of the projectile ion:

$$E_f/E_0 = \left(\frac{\cos(\theta) + \sqrt{(m_t/m_p)^2 - \sin^2(\theta)}}{1 + m_t/m_p} \right)^2. \quad (4.4)$$

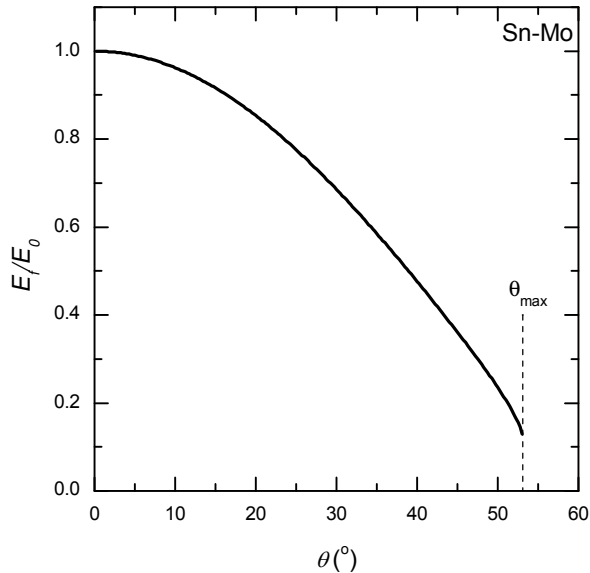


Figure 4.2: The final energy as a fraction of the initial energy of a scattered tin particle from a molybdenum atom. As tin has a higher atomic mass than molybdenum, there is a maximum scattering angle ($\theta_{max} = 53.1^\circ$).

The scattering angle is determined by the impact parameter, the distance between the moving atom's path (without collision) and the target atom: in general the scattering angle will be larger for smaller impact parameters. The recoil angle of the target atom (φ) is determined by the amount of energy transferred to the atom (E_{rec}) and the atomic masses:

$$E_{rec}/E_0 = \frac{4m_t m_p}{(m_t + m_p)^2} \cos^2(\varphi). \quad (4.5)$$

If the mass of the projectile is larger than the mass of the target atom, the angle over which it can scatter is limited. The maximum scattering angle θ_{max} is equal to:

$$\theta_{max} = \arcsin(m_t/m_p). \quad (4.6)$$

In the energy range of this work, the interaction of an incoming atom

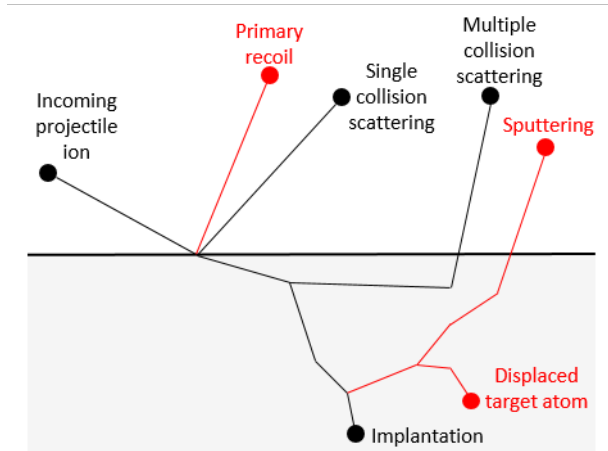


Figure 4.3: A schematic overview of the possible scattering and sputtering events if an incoming projectile ion (black) interacts with the target atoms (red).

with a surface target can be explained by a sum of multiple, consecutive binary collisions, which are described above. Most simulation packages of ion-surface interaction use this approach which is called *Binary Collision Approximation* (BCA). Various outcomes are possible for an ion interacting with a surface. The ion can be implanted into the surface or, if the scattering is large, leave the surface called *backscattering*. A single collision of an ion at or near the surface leading to backscattering is coined single scattering, and the ion will retain an energy in a narrow band around the energy calculated in equation 4.4. If the ion has one collision with a large scattering angle together with multiple small scattering angle collisions, called quasi-single scattering, the energy of the ion is almost fully determined by the large angle scattering collision. For ions which undergo multiple collisions, each over an appreciable scattering angle, there are many combinations of scattering angles available which will lead to the same overall scattering angle. As a result the energy distribution of the backscattered atoms becomes very broad. As $dE/d\theta$ is larger for larger θ (cf. figure 4.2), an ion will lose in general less energy if scattered over a specific angle in multiple collisions compared to a single scattering colli-

sion over this angle. For example, a tin ion scattering over 40° in total will retain 48% of its energy if it is scattered in one collision, but a much higher 73% if it is scattered in two collisions of both 20° . A total scattering angle larger than θ_{max} is only possible if the ion undergoes multiple small-angle collisions.

The energy lost in collisions is transferred to the target atoms (*recoils*) in the surface. A part of the energy is lost to the surface by excitation or ionization of the atoms in the surface, or to vibrational energy in the surface. If the energy of the recoils is high enough to overcome the lattice binding energy, they will also move through the surface and may collide with other atoms. These atoms will also get energy in turn, potentially leading to so-called recoil cascades. Recoils near the surface with enough energy can eventually leave the surface. This process is called *sputtering*. Sputtered atoms have typically lower energies than backscattered atoms. However, primary recoils emitted directly from the topmost surface layers are quite energetic (see equation 4.5) and can attain energies similar to backscattered ions.

Both backscattered as well as sputtered atoms might get (multiply) ionized upon leaving the surface. The probability of ionization is dependent on the ionization potential and the electron affinity of both the surface and the escaping atom. A more detailed description of the interactions near surfaces, including atomic collisions, can be found in e.g. ref. [97].

4.1.2 Stopping

As soon as the particle enters the target, it will lose energy to the atoms and electrons in the sample. This overall loss of energy is generally referred to as *stopping power*, and is defined as the energy loss per unit length:

$$S = dE/dx \tag{4.7}$$

The stopping power is often separated into two classes. One of them is called the electronic stopping power and is the stopping due to the interaction between the particle and the target electrons. The other class, the nuclear stopping power, is the energy loss due to collisions between the screened-off potentials of the nuclei of the projectile and the target particle. Electronic stopping power is typically stronger than nuclear stopping

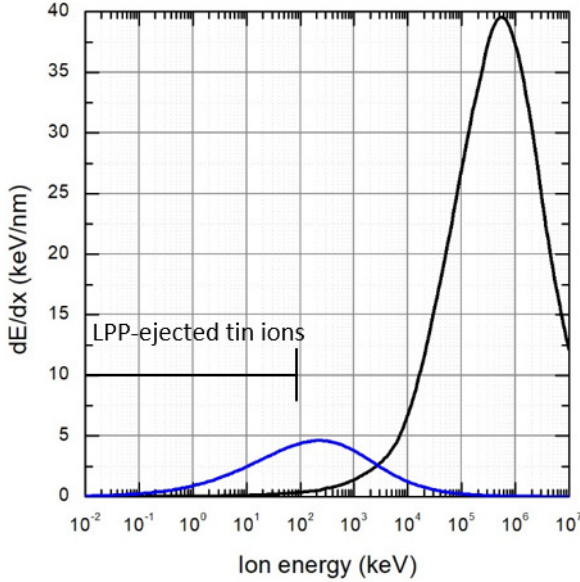


Figure 4.4: The nuclear (blue) and electronic (black) stopping power for tin projectiles in molybdenum. The stopping power data is extracted from SRIM [98].

power, but has its maximum at much higher kinetic energies (see figure 4.4). The energies of tin ions ejected from LPP-sources are relatively low (well below 100 keV, see chapters 2 and 3), where nuclear stopping is dominant.

In nuclear stopping, the projectile loses energy to the target atoms due to the Coulomb repulsion between the nuclear charges of the atoms. The Coulomb potential U depends on the nuclear charge states Z_1 and Z_2 of the projectile and target atom, and the internuclear distance r :

$$U = \frac{Z_1 Z_2}{r} [\text{a.u.}]. \quad (4.8)$$

The screening by the electrons around the nuclei is not included in this formula. They screen off the nuclear charges at large distances, but at near-distance the nuclear charges are only partially screened. Bohr [99] proposed a screening function $\chi = e^{-r/a}$, with $a = (Z_1^{2/3} + Z_2^{2/3})^{-1/2}$ as

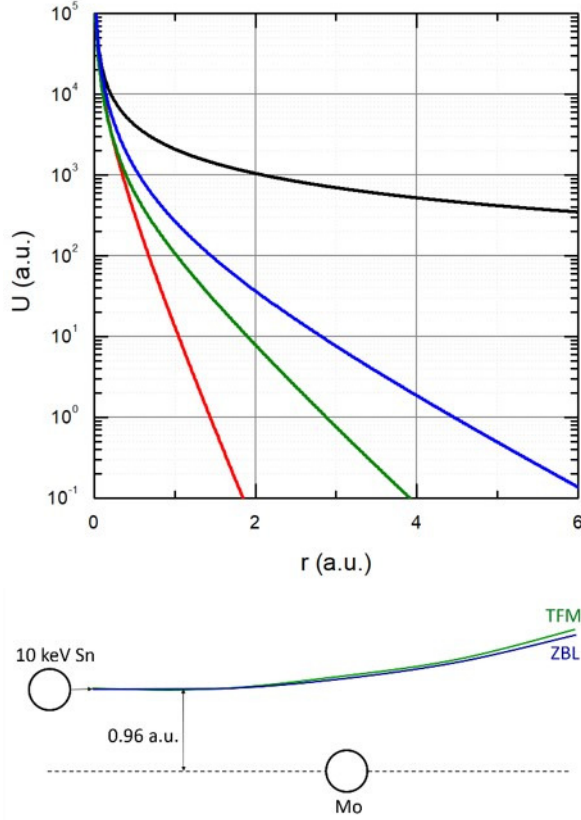


Figure 4.5: (top) The four interatomic potentials, for a tin and a molybdenum atom, described in this work: the Coulomb potential (black), the ZBL potential (blue), the TFM potential with the Firsov screening length (green), and the Bohr potential (red). (bottom) An approximation of the trajectory of a 10 keV tin ion scattering from a molybdenum atom at an impact parameter of 0.96 a.u. (0.5 \AA) for the ZBL potential and the TFM potential.

the screening length, to account for this screening:

$$U = \frac{Z_1 Z_2}{r} \chi. \quad (4.9)$$

Over the years several screening length constants and screening potentials have been proposed. A commonly used potential is the Molière approximation [100] of the Thomas-Fermi screening function (the TFM potential):

$$\chi = 0.35e^{-0.3r/a} + 0.55e^{-1.2r/a} + 0.10e^{-6r/a}. \quad (4.10)$$

Firsov used a statistical model to determine an accurate screening length for this TFM potential [101]:

$$a = \frac{0.8853}{(Z_1^{1/2} + Z_2^{1/2})^{2/3}}. \quad (4.11)$$

In recent times, a semi-empirical potential function called the ZBL potential, proposed by Ziegler, Biersack, and Littmark [102], is most often used to describe the screened Coulomb potential of the atoms. This ZBL potential is obtained by fitting a universal potential function to a number of theoretically calculated interatomic potentials, and is equal to:

$$\chi = 0.1818e^{-3.2r/a} + 0.5099e^{-0.9423r/a} + 0.2802e^{-0.4028r/a} + 0.2817e^{-0.2016r/a} \quad (4.12)$$

with a screening length a :

$$a = \frac{0.8853}{Z_1^{0.23} + Z_2^{0.23}}. \quad (4.13)$$

In figure 4.5, the Coulomb potential and the three mentioned screened potentials are shown. At larger interatomic distances, the Coulomb potential predicts still a large repulsion between the atoms, as it does not regard any screening by the electrons. For distances below 0.5 a.u., the TFM potential and the Bohr-potential are virtually the same; at longer distances the repulsion is stronger for the TFM potential. Where the Bohr potential is virtually zero at 2 a.u., the TFM potential is still substantial at that distance. The ZBL potential is close to both the Bohr potential as well as the TFM potential at distances near the ion core, but decreases more gradually than the other two screened potentials at longer distances. From roughly 0.2 a.u. on, the interatomic repulsion is always higher for

the ZBL potential. This difference in repulsion strength results in different ion trajectories and therefore different scattering angles. As shown in figure 4.5, a 10 keV tin ion scattering from a molybdenum atom at an impact parameter of 0.96 a.u. has a scattering angle of 12.4° for the ZBL potential, but an angle of 13.8° for the TFM potential, an appreciable and measurable difference. In simulations the ZBL potential is the most used potential form.

4.2 Electronic processes

4.2.1 Over-the-barrier

The neutralization of multicharged ions approaching a conducting surface can be described by the *over-the-barrier* (OVB) model [103]. In the OVB-model, the electrons at the top of the conduction band are moving over the potential barrier from the surface to the ion almost instantaneously, as the barrier lowers as the ion approaches the surface and drops below the surface's work function level. The barrier is determined by the ion with charge state $+q$ at distance z from the target, the electron with charge state $-e$ at distance d , and their image charges $-q$ and $+e$, respectively. The potential V at the ion-surface axis which the electron experiences is the sum of the electric fields of these charges:

$$V = -\frac{q}{|z-d|} + \frac{q}{z+d} - \frac{1}{4d}. \quad (4.14)$$

The *saddle point* d_s is the point where the potential between the ion and the target is at its maximum. As soon as the ion is close enough to the target that the potential at the saddle point is lower than the work function ϕ of the target, electrons can transit from the target to the ion. In figure 4.6 the potential barrier for a double-charged ion at 11 a.u. from the surface is shown, together with a work function of 5 eV. As soon as the electron has moved towards the ion, the barrier will increase again because the ion is now singly charged, and the next electron can only be captured as soon as the ion is close enough to the surface that the saddle point potential is lower than the work function again. The position of the saddle point is approximately equal to [103]:

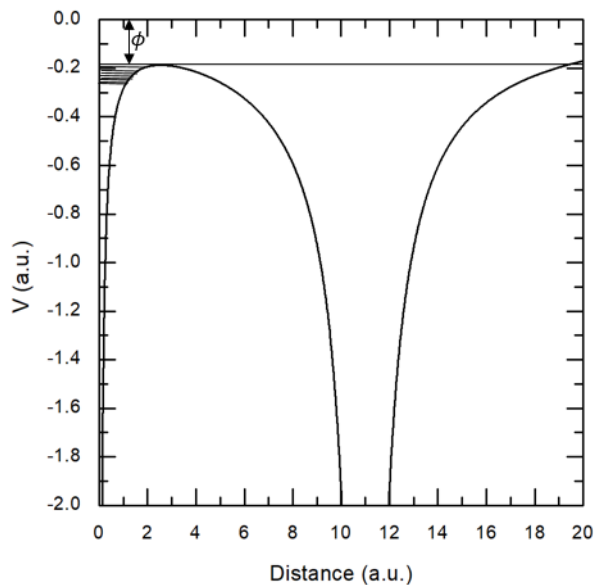


Figure 4.6: The potential an electron experiences along the ion-surface axis for a double-charged ion at 11 a.u. from a conducting surface. At this distance, an electron at the top of the conduction band of a surface with a work function of 5 eV (horizontal line) can move towards a double-charged ion.

$$d_s \approx \frac{z}{\sqrt{8q+2}}. \quad (4.15)$$

At the saddle point, the potential is equal to:

$$V_s \approx -\frac{\sqrt{8q+2}}{2z}. \quad (4.16)$$

The neutralization distance z_o can be found by equating this potential to the work function of the surface:

$$z_o \approx \frac{\sqrt{8q+2}}{2\phi}. \quad (4.17)$$

The neutralization distance is shown for different charge states in figure 4.7 for a generic metallic target with a typical work function of 5 eV. A tin

ion scattered from the surface has an impact parameter up to 2 a.u., well within the neutralization distance of 8.6 a.u. from the surface. A scattered ion is therefore very likely to be neutralized before any scattering processes take place, and therefore the initial charge state of an ion is often of lesser importance in scattering processes.

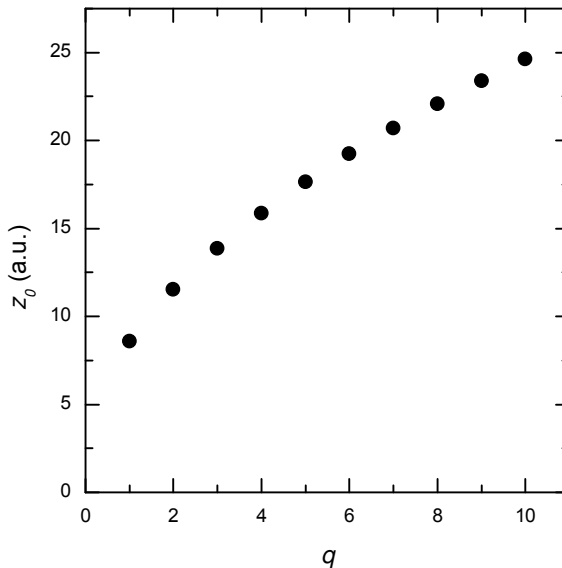


Figure 4.7: The neutralization distance z_0 for an ion with charge state q , approaching a target surface with a typical work function of 5 eV.

The force on the ion by the image charge is equal to $-q^2/(4z^2)$. This force accelerates the ion towards the surface. Assuming step-wise resonant electron capture and a complete screening of the ion core by the transferred electrons, the total energy gained by the image charge attraction is approximately equal to [104]:

$$E_{im} = \frac{q^{3/2}\phi}{3\sqrt{2}}. \quad (4.18)$$

The image energy puts a maximum on the interaction time between the ion and the surface, thereby limiting the time available for auto-ionization (see

next section) before impact at and penetration into the surface [105, 106]. The acceleration towards the surface will also induce different incidence and detection angles of the incoming ions and particles emitted from the ion-surface system [107]. Image charge acceleration has a negligible role in our ion scattering experiments due to the relatively high scattering energies, but can have influence on decelerated ion beams in electron detection measurements.

4.2.2 Electron capture

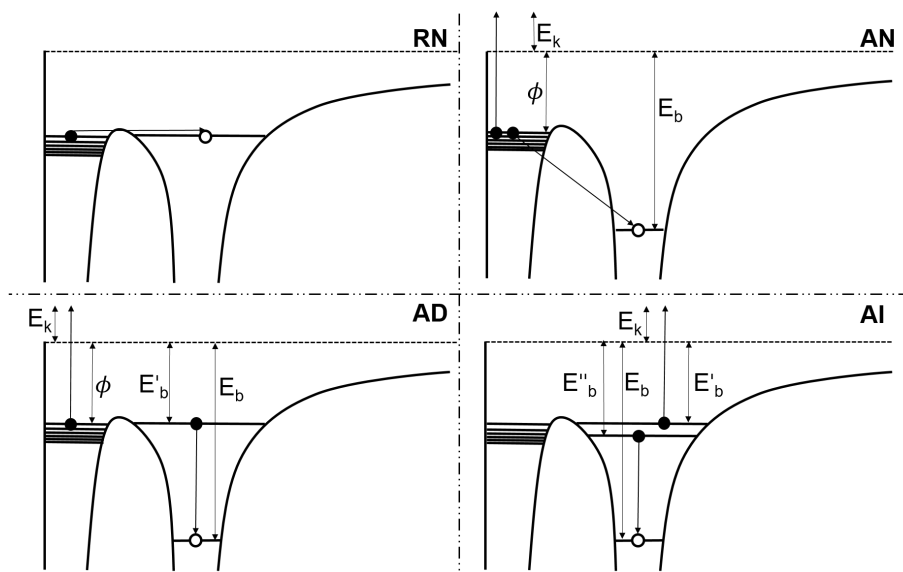


Figure 4.8: Schematic drawings of four types of electronic transitions occurring when an ion is near a surface: resonant neutralization (RN), Auger neutralization (AN), Auger de-excitation (AD), and Auger auto-ionization (AI).

The electrons can be captured from the surface by the ion via several processes. At first, the electrons can be captured by resonant neutralization (RN), as in the OVB-model, and Auger neutralization (AN). As soon as electrons are captured in the excited states of the ion, also Auger

de-excitation (AD) and Auger auto-ionization (AI) can take place. The ejection of electrons by an ion-metal surface system is extensively treated by Hagstrum [108]; here follows a short overview of the relevant processes, which are shown in figure 4.8.

RN is the transfer of an electron from the target surface into a resonant state of the projectile ion, often an excited state of the ion. In this process, no electrons or excess energy is emitted. The likelihood of this process happening is dependent on the presence of a resonant state in which the electron can be captured. Tunneling of the electron through the barrier is also possible, but is rare for multiple charged ions as interaction can take place at distances much larger than the distance normally associated with tunneling, and can in general be ignored. The reverse process, where an electron transfers resonantly from the ion to the surface, is called resonant ionization (RI). This process can be ignored when the ion approaches the surface, as the ion is in the ground state and there are no electrons to transfer to the surface. If the atom leaves the surface again, this process can take place and the atom can get ionized.

AN is an Auger process. In Auger processes, the energy gain of an electron moving towards a stronger bound state is transferred to another electron, which typically will be emitted from the ion or the surface. In AN, one electron will move from the valence band of the surface towards a stronger bound state of the ion. Simultaneously, the energy of this transition is transferred to another electron in the valence band, which will be emitted from the surface. This electron will have a kinetic energy, E_k , dependent on the binding energy E_b of the other electron, and the work function ϕ of the surface: $E_k = E_b - 2\phi$. AN is often the dominant neutralization process [109] for singly charged ions. For this process, no electrons in excited states, or a state of the ion resonant with the conduction band are required, contrary to the other electronic transition processes.

AD is a similar process, but only one electron from the surface is involved, while the other electron is from an excited state of the ion. One of the electrons moves to a stronger bound state of the ion, while the other electron obtains the energy gained in this process and is emitted from the ion-target system. The kinetic energy of the emitted electron is equal to $E_k = E_b - \phi - E'_b$, where E'_b is the binding energy of the electron in the weaker bound state of the ion.

For AI, two electrons in an excited state of the ion are necessary. One of the electrons makes a transition towards a stronger bound state of the ion, while the other electron is emitted obtaining the energy gained from this process. If E'_b is the binding energy for one of the electrons in its original state and E''_b the binding energy for the other electron, the kinetic energy of the emitted electron is equal to $E_k = E_b - E'_b - E''_b$.

4.2.3 De-excitation of the ion

The electrons captured resonantly from the surface populate highly excited states. Such ions with an inverted electron structure are known as *hollow atoms* [110]. De-excitation of the hollow atom will take place by AI, up to the point that the atom is fully in the ground state or that the atom hits the target, which is the most likely scenario as typically only tens of femtoseconds are available between hollow atom creation and penetration of the electronic selvedge of the surface. Because atomic binding energies are well-defined, the emitted electrons produce distinct Auger peaks in the electron spectra. The energy of these Auger peaks can give valuable insight about the transient atomic structure of the hollow atom. The subject of hollow atoms was thoroughly investigated in the 1990s; a review of this field can be found in ref. [111].

As Auger processes favor decay of electrons to the nearest continuum, emission of low-energy Auger electrons from the ion-surface system dominate the electron spectra. In addition to the Auger electrons, also the kinetic impact of the ion on the surface produces an excess of low-energy electrons as the impact heats the electronic system of the target. For this reason, an electron spectrum has a high, exponentially decreasing yield for low electron energies, together with the possibility of Auger peaks apparent in the spectrum. The beam has to be decelerated in order to increase the interaction time between the ion and the target surface, which increases the probability to detect Auger peaks. Another possibility is to decrease the angle with the target, as the velocity vector part perpendicular to the target is then decreased.

4.3 Ion source

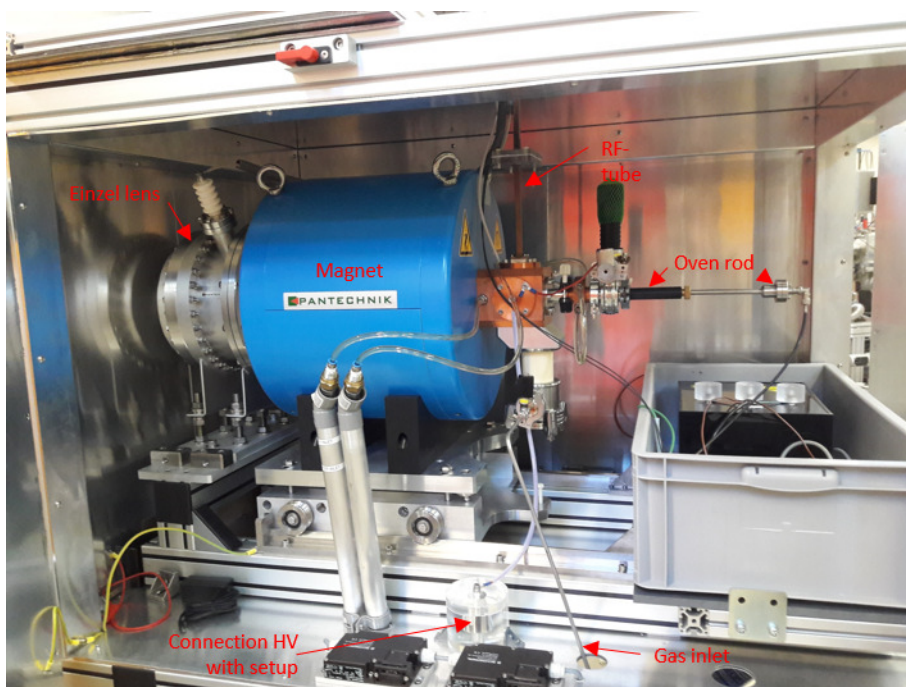


Figure 4.9: A photo of the ion source with the tin oven. The plasma is created in a vacuum chamber inside the magnet. The ions are extracted towards the left.

The ion beams in our experiments are generated by a Superanogan ECRIS (Electron Cyclotron Resonance Ion Source) type ion source of which the permanent magnetic structure and vacuum chamber and supports were purchased from Pantechnik. This source, and the corresponding beamline, is installed in 2015 at the Zernike Institute for Advanced Materials. The source consists of a vacuum chamber inside a permanent magnet, creating a strong, radially and axially increasing magnetic field. By means of an oven (see subsection 4.3.1) or a gas inlet, a vapor of the desired element can be introduced in the vacuum chamber. The vapor is ionized by electron impact ionization. The electrons in the plasma are

gyrating around the magnetic field lines with a certain frequency ω , dependent on the strength of the magnetic field B :

$$\omega = \frac{e|B|}{m_e}. \quad (4.19)$$

An injected RF-field of 14 GHz (2.1 cm) matches the gyration frequency of electrons at a magnetic field strength of 0.5 T; these electrons are accelerated resonantly and can attain high velocities. This enables multiple and stepwise electron impact ionization of the plasma, which can ionize the atoms to charge states well above 10+. The RF power, delivered at the Supernanogan by a 7 m waveguide, is coupled into the chamber through an oversized coaxially waveguide, in which also the oven is installed and the gas is let in.

The whole source is on a high potential V_S and this, together with the charge state of the ions q and the plasma potential V_P , determines the kinetic energy E_{kin} of the ions extracted from the source:

$$E_{kin} = q(V_S + V_P)[\text{eV}]. \quad (4.20)$$

The plasma potential is typically in the range of 10-30 V. The ions can get kinetic energies ranging from 5 to more than 20 keV/q. For experiments with lower kinetic energies, the low energy ion scattering setup can be floated at a set potential. More information about the deceleration of ions can be found in subsection 4.4.1.

All ions are extracted from the source through a diaphragm and a puller, which provides a small electric potential. The ions in the plasma in the source have a wide range of charge states and the background gas in the source is ionized. An 110° magnet selects the right ion in the right charge state, as the strength of the magnetic field B , which can be controlled, is proportional to the source voltage and the mass-over-charge ratio A/q : $B \propto \sqrt{V_S A/q}$. An Einzel lens is used to focus the ions into the magnet.

The ion beam goes through a 10 mm diaphragm before entering the beam line. The beam current output of the source can be monitored by a (movable) Faraday cup (FC) placed directly behind the diaphragm. The beam is guided through the beam line by three quadrupole triplets. The transmission can be measured with a FC and is typically close to 100% at

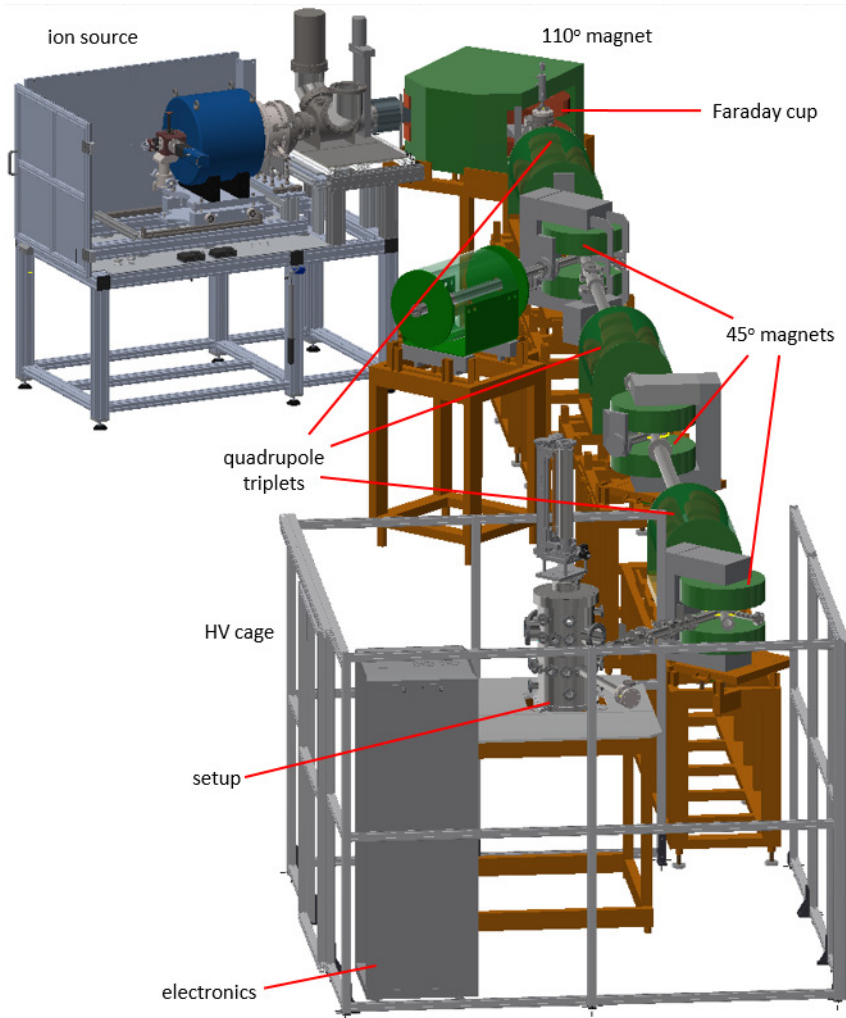


Figure 4.10: Drawing of the ion source, beam line, and the setup with HV cage. The other setups attached to the beam line are not shown. The beam line spans approximately 15 m from the source to the setup.

the end of the beamline. By means of 45° bending magnets, the ion beam can be directed into the various experimental setups. The setup described in section 4.4 is connected to the last bending magnet (see figure 4.10).

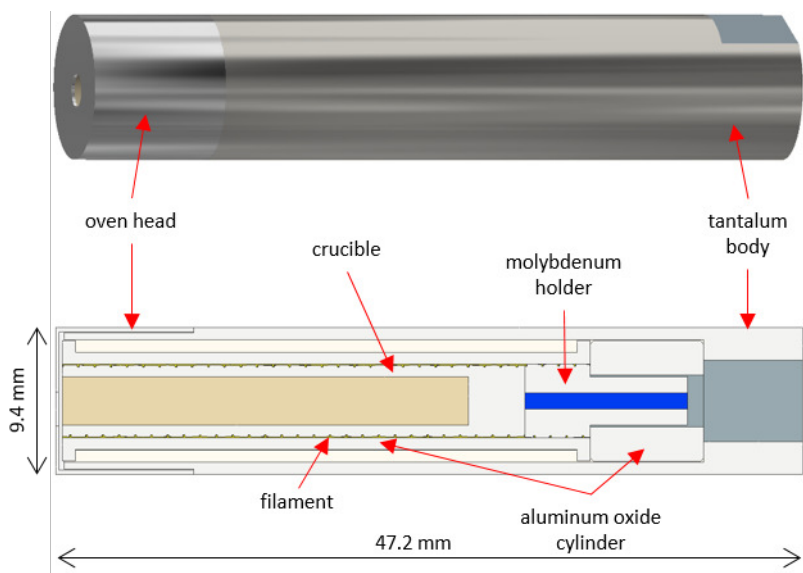


Figure 4.11: Drawing of the tin oven (top) and its cross section (bottom). The oven is attached to the linear translator rod at the right side. The tin vapor leaves the oven at the left side.

4.3.1 Oven

An oven (see figure 4.11) can be used to make an ion beam from targets which are solid at room temperature, such as tin. The oven consists of an aluminum oxide crucible and is heated by a tungsten filament, which works as a resistive heater. The filament is wrapped around the crucible and around a molybdenum holder. The holder is used to make a connection with the heating power supply. At the other end, the filament is connected to the oven head. The original stainless steel head is replaced with a tantalum cap to increase the lifetime of the ovens. The crucible and the filament are encapsulated in an aluminum oxide cylinder, which itself is placed inside a tantalum body. The oven is placed on a linear translator rod inside the RF-tube. This rod can be used to control the distance between the oven and the plasma.

Figure 4.12 shows the beam current of singly charged tin (at the FC behind the 110° magnet) versus the power of the electric current through

the oven. The beam current starts to rise at a power of 17 W, therewith achieving temperatures of about 900 °C [112]. The oven is normally operated with powers around 30 W, corresponding to a temperature of 1100° C. The tin atoms are evaporated into the main plasma of the source, normally a He plasma which provides electrons for rapid electron impact ionization of the tin atoms.

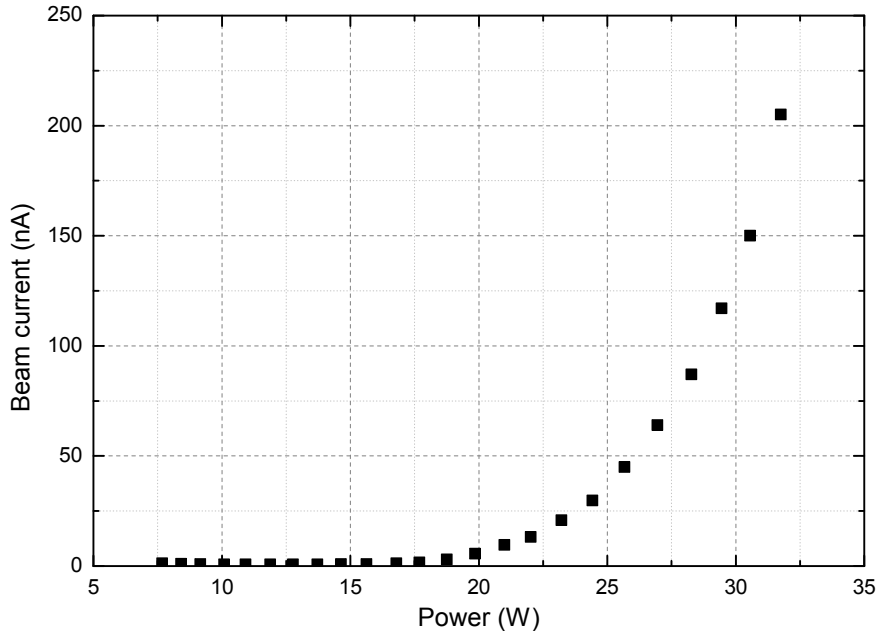


Figure 4.12: The beam current of a 7 keV $^{120}\text{Sn}^+$ beam versus the power through the tin oven. The current is measured directly behind the 110° magnet.

Tin has no less than ten stable and naturally abundant isotopes, ranging from mass number 112 to 124. Of these ten isotopes, three have a natural abundance of more than 10%: 116 (14.5%), 118 (24.2%), and 120 (32.6%). We select one isotope for the ion beam with the 110° -magnet. Unless otherwise specified, the tin ion beams used in the experiments consist of Sn-120.

4.4 The ion-surface setup

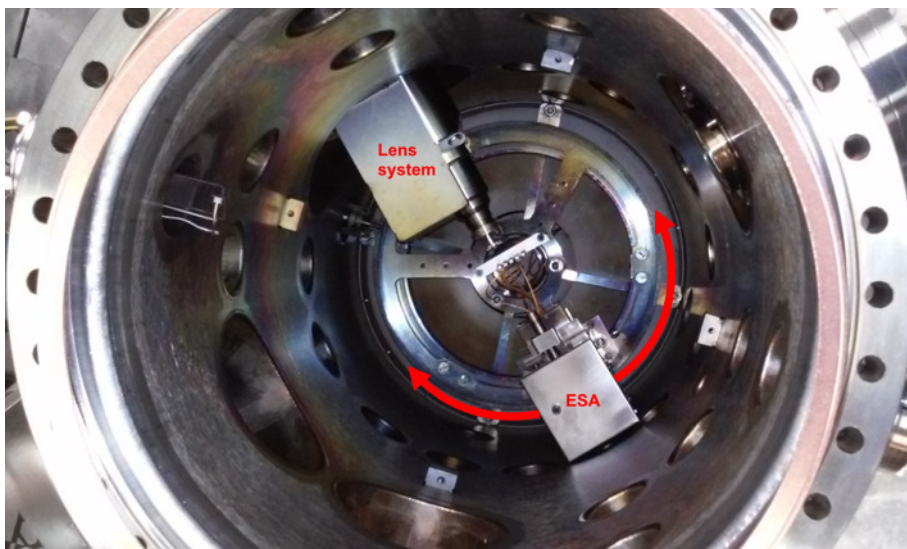


Figure 4.13: A top view of the setup. The last part of the deceleration lens system, where the beam enters the setup, is visible at the top. The detector (ESA) is visible at the bottom. The manipulator with target is not included in this figure.

The data in chapters 5 and 6 is collected with the surface physics setup $\text{Sir}\Phi$, connected to the previously described beamline. The heart of the setup is a 300 mm diameter μ -metal vacuum vessel, with a target manipulator (manufactured by Thermo Vacuum Generators) on top. The target is attached to the manipulator by two molybdenum clamps. The manipulator can be moved in all three directions, with a range of 25 mm in both directions in the plane of the beam and the detector (x,y), and a range of 400 mm perpendicular to this plane (z). The manipulator can make a full rotation around its axis, allowing for different target grazing incidence angles (ψ). The target can also be rotated to vary the azimuthal angle, but that feature is not used in this work. An electron bombardment heating system can heat the target to clean it, and a thermocouple can be used to measure the target temperature.

The ion beam is guided towards the setup through a differential pumping stage between the beamline and the main chamber. A diaphragm is placed directly behind the bending magnet and two diaphragms of 2 mm are placed in front of the deceleration lens system (see section 4.4.1). The beam enters the main chamber through two collimation diaphragms of 2 and 1.5 mm between the lens system and the main chamber. The ions and electrons resulting from the ion-surface collisions are collected by a semi-hemispherical electrostatic analyzer (ESA). This ESA can be rotated around the target, allowing different detection angles (θ). A detailed description of the ESA can be found in subsection 4.4.2. The beam current can be monitored on the diaphragm in front of the deceleration lens system, on the target sample, and on a FC behind the target. The sample current is recorded during measurements to correct for beam fluctuations. Secondary electron emission is not prevented so this will result in an overestimation of the beam current, which has to be considered in interpretation of the data.

A 400 l/s ion getter pump is used to sustain UHV pressure. An additional turbomolecular pump can be used during bake-out and the initial pumping down, but is locked off by a valve during measurements. The differential pumping stage can also be closed off by valves at both sides. An ion getter pump is used to hold the vacuum in this part to approximately 10^{-8} mbar.

4.4.1 Beam deceleration

The setup, all the accompanying electronics, and the measurement & control computer can all be floated on high voltage by the same power supply which puts the source on its high potential (V_S). This matches the potential of the setup and the source and removes any fluctuations of the source potential in the kinetic energy of the beam. At the setup, a second power supply provides a voltage difference (bias potential, V_{bias}) between the setup and the source. This bias potential determines the final kinetic energy of the ions at the target, together with the charge state of the ions and the plasma potential:

$$E_{kin} = q(V_{bias} + V_P). \quad (4.21)$$

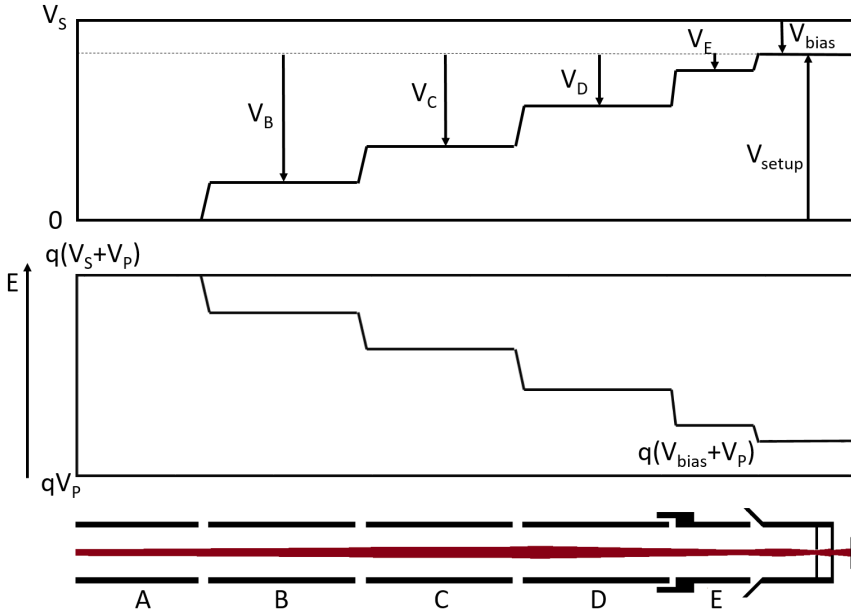


Figure 4.14: (upper) Sketch of the potentials and the resulting ion energies in the deceleration lens system. (lower) Result of simulations in Simion for decelerating a doubly charged helium ion beam from 14 to 0.1 keV.

The setup, including electronics and pumps, will be on a high potential during the measurements: $V_{setup} = V_s - V_{bias}$. During transport of the ion beam towards the setup, the ions are at ground potential. The beam is guided towards the target at high potential by a deceleration lens system of five electrostatic lenses, labeled alphabetically in order of appearance (A-E). The first lens (A) is at the same potential as the beamline (common ground), while lenses B-E are at an increasing potential. The ions are gradually slowed down before reaching the target with the final kinetic energy. The *FuG* power supplies for lenses B-E are controlled by the computer. During measurements where the ions are not decelerated, all five lenses are at ground potential.

4.4.2 Electrostatic Analyzer

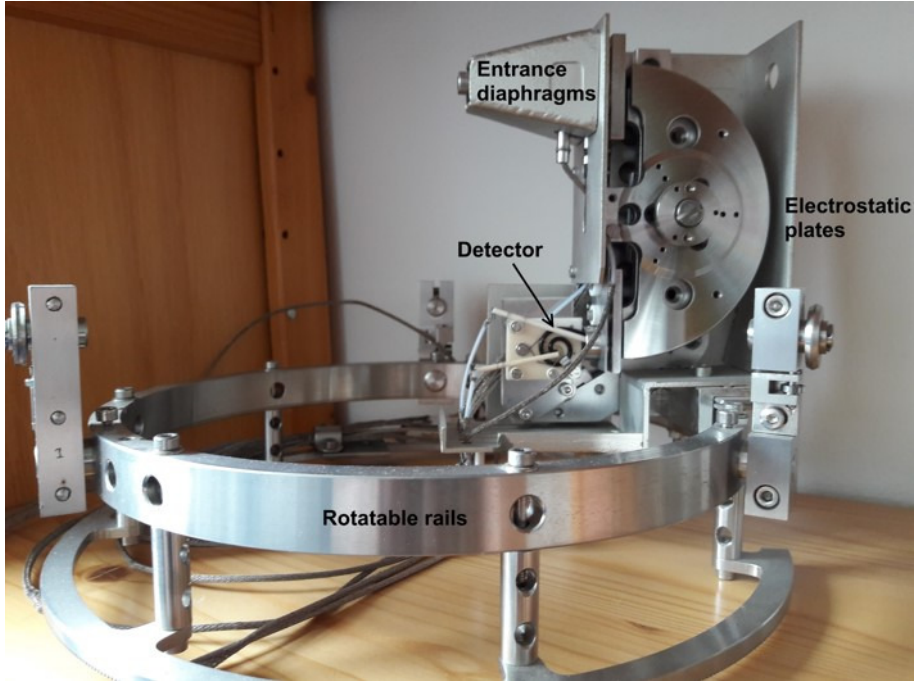


Figure 4.15: A duplicate of the electrostatic analyzer (ESA). Visible are the entrance diaphragms, the electrostatic plates and the rails system on which the detector can rotate around the target. The detector in the figure is a channeltron; a multichannel plate is used in the ESA in the setup.

The electrostatic analyzer (ESA) consists of two concentric hemispherical plates. These two plates are both kept on the appropriate voltages, resulting in an electrostatic field. A charged particle (electron or ion) will only pass the ESA when the centripetal force is equal to the force due to the electrostatic field [113]:

$$\frac{mv^2}{r} = q \frac{V_2 - V_1}{R_2 - R_1} \frac{R_2 R_1}{r^2}, \quad (4.22)$$

where m is the mass of the particle, q the charge of the particle, V_2 and V_1 the voltage on respectively the outer and inner plate, R_2 and R_1 the radii

of respectively the outer and inner plate, and r the central trajectory of the particle. This r is equal to $r = (R_2 + R_1)/2$. The voltage difference between the plates determines the kinetic energy E_k of the detected particle:

$$\frac{E_k}{q} = F(V_2 - V_1) \quad (4.23)$$

The proportionality constant F is dependent on the radii of the plates:

$$F = \left(\frac{R_2}{R_1} - \frac{R_1}{R_2} \right)^{-1} \quad (4.24)$$

To ensure that the particle is not accelerated or decelerated in the detector, the potential at the central trajectory should be zero. This condition is fulfilled if $\frac{V_2}{V_1} = -\frac{R_1}{R_2}$.

The radii of the outer and inner plate are respectively $R_2 = 52$ mm and $R_1 = 48$ mm. This results in theoretical values of $F = 6.24$ and $\frac{V_2}{V_1} = -0.923$. However, the detector consists of two central slices of hemispheres and is therefore only semi-hemispherical. Instead of the theoretical values, we use empirically found values of $F = 6.42$ and $\frac{V_2}{V_1} = -0.935$ [113].

The particles pass two diaphragms of 1.9 and 0.4 mm while entering the detector, and at the end of the detector a 0.5 mm x 1.9 mm exit slit is placed. A multichannel plate (MCP) detects the particles. The pulses generated by the MCP are analyzed by a single channel analyzer and counted by a data acquisition device, which is recorded by a computer. The electrostatic potentials on the plates of the ESA are controlled by a home-made Labview program (see appendix B). This same program also controls the potentials of the deceleration lens system and is automated to measure the signal over a certain energy range. A more detailed description of the power supply for the plates of the ESA can be found in appendix A.

The energy resolution of the ESA ($\Delta E/E$) depends on the diameters of the diaphragms, the radius of the ESA, and the angular divergence of the beam [114]; this ratio is constant:

$$\Delta E/E = \text{constant}. \quad (4.25)$$

For all spectra in the remainder of this work, the signal (counts per second)

is divided by the energy to account for the changing width of the energy bins, ΔE , with energy.

4.4.3 Tin ion detection efficiency

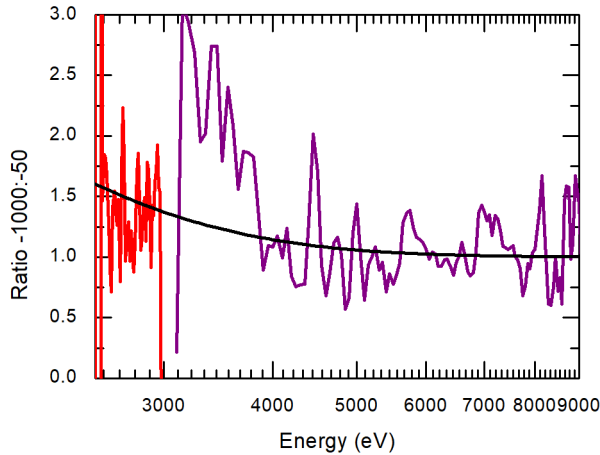


Figure 4.16: Detection efficiency ratios (red and purple) for two different tin ion energy distributions. For each distribution, two measurements are performed: one is measured with -50 V on the front of the MCP, and the other at -1000 V. The black line is the ratio of the correction factors for the tin detection efficiency given by eq. 4.26.

The detection efficiency of an MCP depends on the kinetic energy of the impinging ions. Ions with lower kinetic energies produce less electrons on impact, which reduces the height of the output signal of the MCP. For charged particles, a higher potential on the front of the MCP enhances the signal as the particles are accelerated and therefore create more impact electrons.

To obtain a proper ion energy distribution, we have to correct the yield for the ion detection efficiency. At ARCNL, the detection efficiency of channeltrons for tin ions has been investigated and an empirical formula for the detection efficiency correction factor k for tin ions is found:

$$k = \frac{100}{40(1 + \tanh((v_{impact} - a)/b))}. \quad (4.26)$$

The fitting parameters a and b are found to be equal to 0.031 and 0.0095 respectively. The impact velocity is a function of the kinetic energy of the ions (E_k), the charge state of the impinging ion (q), and the voltage on the front of the MCP (V_{front}) and is for a tin atom with an average mass of 119 amu given by:

$$v_{impact}[\text{a.u.}] = 0.2 \sqrt{\frac{E_{kin}[\text{eV}] + qV_{front}[\text{V}]}{119000}}. \quad (4.27)$$

The investigated channeltrons have the same working principle as the MCP in this work, and the correction factor could be applicable for the distributions in this work. We test this by measuring two distributions in a different energy range, ranging from 2.5 to 9.0 keV, for two different voltages on front of the MCP, -50 V and -1000 V. The difference in front voltage will result in different impact velocities, and can be used to verify the efficiency factor for our MCP. In figure 4.16, the two ratios of the different voltages for these spectra are shown. The ratio from the experiments is in good agreement with the ratio from the channeltron correction factors. We correct therefore the tin backscattering distributions in this work with the same factors as determined for channeltron and given in equation 4.26.

4.4.4 Electron measurements

He^{2+} ions will produce a distinct set of Auger peaks around 35 eV, originating from autoionization (AI) of two electrons in the singlet $2s^2$, $2p^2$, $2s2p$, and the triplet $2s2p$ state [115]. These distinct peaks make a He^{2+} ion beam suitable to test the calibration. The electron spectra shown in this section are measured with a target angle of 15° and a detection angle of 105° , or at normal incidence from the target. The electron yield is measured for energies up to 40 eV, with a step size of 0.5 eV.

The measurements of low-energy electrons below 30 eV are difficult, due to the earth magnetic field and other electromagnetic fields which may deflect the electrons. In order to prevent this, the whole vacuum

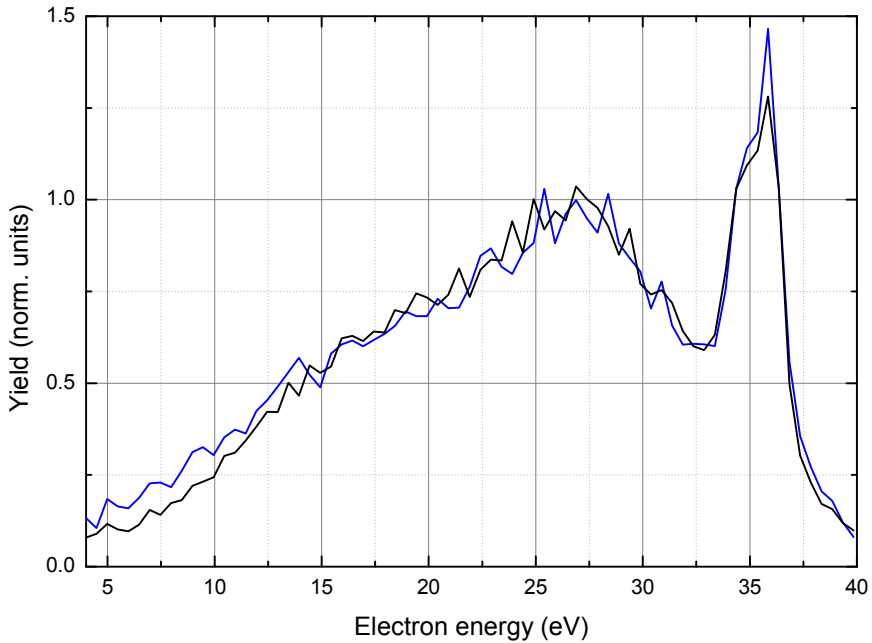


Figure 4.17: Two electron spectra of 100 eV He^{2+} on a Mo target at a target angle of 15° and a detection angle of 105° , and normalized on the maximum of the broad spectrum. The black spectrum is without additional shielding, the blue spectrum with μ -metal shielding on the CF-40 viewports additional to the shielding of the vessel. Around 35 eV, a distinct set of Auger peaks is visible [115].

vessel is made of μ -metal, which shields the inside of the chamber from external magnetic fields. Figure 4.17 shows measurements of an electron spectrum with and without additional shielding around the viewports, the lens system, and the blind flanges connected to the vacuum chamber. The additional shielding slightly increases the yield of low-energy electrons.

In order to detect more low-energy electrons, it is possible to put the target on a small negative bias voltage. As shown in figure 4.18, the yield of electrons below 25 eV is drastically enhanced for an increasing bias voltage. Also apparent is a Doppler shift of the Auger peaks around 35 eV. The ion beam is accelerated towards the target due to the bias volt-

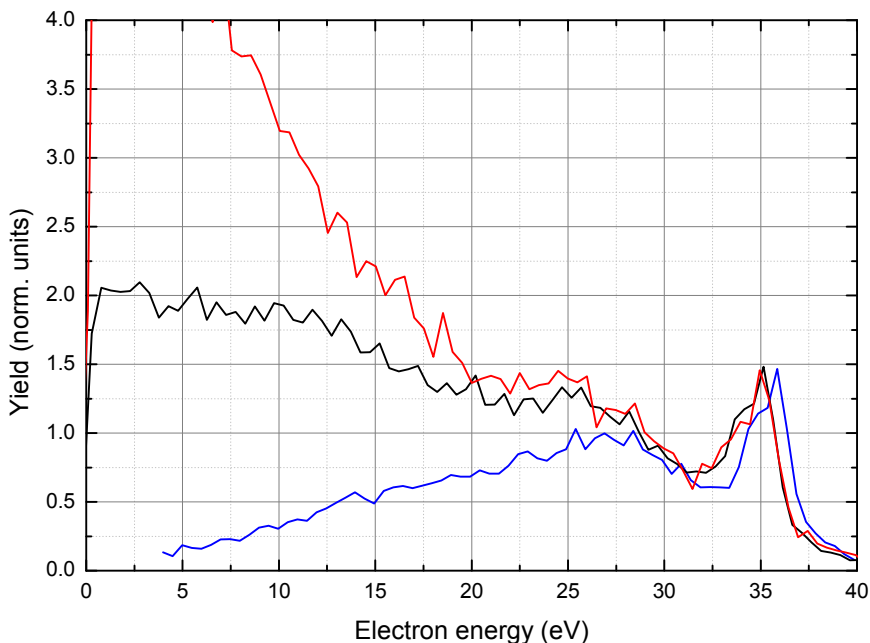


Figure 4.18: Three electron spectra with different bias voltages of 100 eV He^{2+} on a Mo target at a target angle of 15° and a detection angle of 105° . The blue spectrum is without a bias voltage, the black spectrum is biased with -9.67 V and the red spectrum with -19.33 V. The electron energy given is corrected for this bias voltage, and the yield is normalized in such a way that the Auger peaks around 35 eV have a similar yield.

age, and changes the angle of the beam. The detection angle is therefore more backwards (larger than 90°), causing a Doppler shift towards a lower energy. Another disadvantage of a bias voltage on the target is that no distinct information about the angular dependence of the electrons can be gained, as all electrons get directed towards the normal of the surface.

In figure 4.19, two electron spectra for different charge states of helium, $1+$ and $2+$, are shown. Atomic auto-ionization, which requires a doubly excited electronic configuration, is not possible for He^+ in the ground state, and therefore the distinct set of peaks around 35 eV does not appear, as any metastable He^+ ions are likely to be quenched. According to Zeijlmans

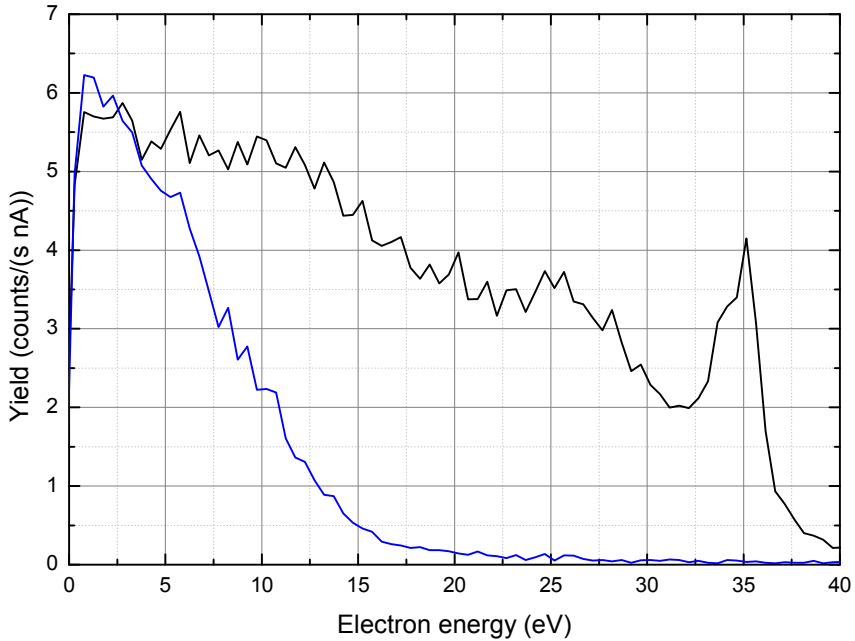


Figure 4.19: Two electron spectra of 100 eV He^{2+} (black) and He^{1+} (blue) on a Mo target at a target angle of 15° and a detection angle of 105° . A bias voltage of -9.67 V on target is applied. The electron energy given is corrected for this bias voltage, while the yield is only corrected for the beam current.

van Emmichoven et al. [116], who treat these particular electron spectra in more detail, electronic transitions other than AN are negligible for He^+ . For He^{2+} , AN towards He^+ and AD from doubly to singly excited helium is dominant, in addition to the AI process producing the peaks at 35 eV and AN of He^+ . This AN towards singly charged helium and the AD process produce the broad spectrum between the kinetic impact electrons and the AI peaks, and are absent for the He^+ spectrum as those processes can not take place with one electron in the excited state.

The previously shown electron spectra are measured with the target slightly off-center, resulting in an unintended mis-match between the overlap of the beam on target and the ESA. The target was $30 \mu\text{m}$ from the

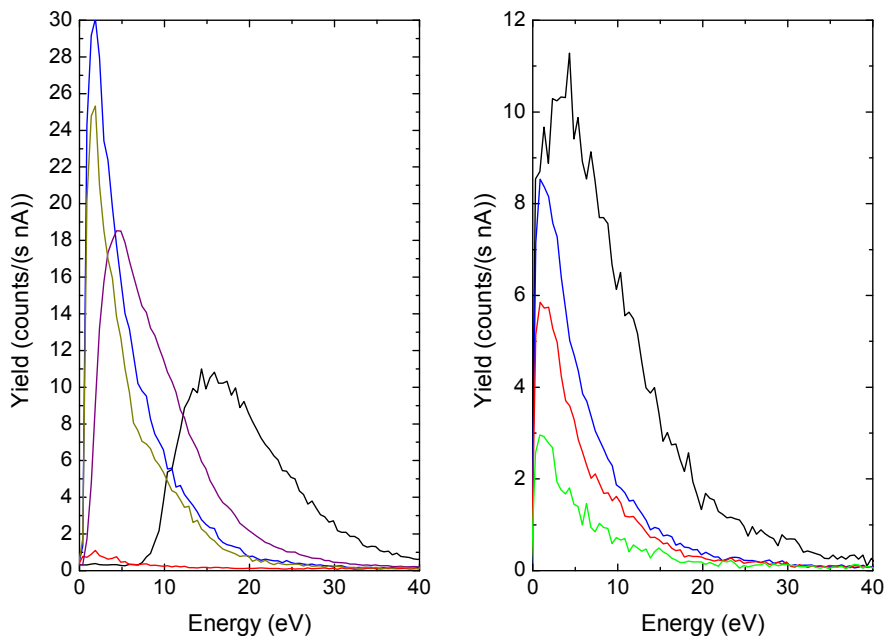


Figure 4.20: Electron spectra with the target slightly off-center ($30 \mu\text{m}$ perpendicular at the ion beam axis; left) and at the center (right) for a He^+ ion beam with different energies: 7 keV (black), 2 keV (purple), 1.5 keV (blue), 1.4 keV (dark yellow), 1.3 keV (red) and 1 keV (green). The target is at a bias voltage of -9.67 V , for which is corrected in the electron energy.

center perpendicular to the ion beam axis, which can result in non-correct electron spectra (see figure 4.20). After a $30 \mu\text{m}$ correction of the target position, the electron spectra show the normal low-energy impact electrons as expected from singly charged ions. We do not expect any deviation for the previously described test experiments with different charge states, or the positions of the Auger peaks around 35 eV .

4.5 SRIM

An often used computer package to simulate ion stopping is SRIM (Stopping Range In Matter) [98]. In this work, the SRIM nomenclature of referring to the projectiles as ions is adopted, although the package does not consider charge in its simulations. Originally the package is developed to calculate stopping power tables, mainly for high-energy ions where electronic stopping power is dominant. The package is later on expanded with Monte Carlo simulations (TRIM), where the ion range and trajectory in matter is simulated with the ZBL-potential described in section 4.1.1. With these simulations, also predictions on the energy and the exit angle of atoms leaving the target can be calculated. Depending on the level of detail of the simulations, the trajectories and range of the recoil atoms are also calculated. This can give some insight about the sputtering yield, and the angular distribution and energy of the recoils. Simulations of sputtering are sensitive to some not well-known input parameters such as the surface binding energy, and should therefore be treated with care [117, 118]. It is also reported that there exist deviations from experimental results for low-energy ions, mainly due to uncertainty in the electronic stopping power [119]. Another disadvantage is that SRIM uses solely neutral atoms, and that no charge effects are taken into consideration. The SRIM results for backscattered particles could deviate from the experimental results obtained with an electrostatic analyzer, as this detector only measures ions. The probability of reionization, the ionization of a neutralized ion leaving the surface, depends heavily on the combination of the ion and the target element [120]. The reionization probability does not depend on the projectile ion energy above a certain threshold, which is typically low. A comparison of simulations with experiments where several ion species are detected (such as sputtered and backscattered material) is often compromised, but a comparison with scattering energy distributions is feasible.

In SRIM, all incoming particles are individually and subsequently generated at the edge of the surface, and have a pre-set energy and direction. Nuclear and electronic stopping are treated separately, where the nuclear stopping is the result of a series of binary collisions and the electronic stopping is the energy loss in-between those collisions. The position of each collision is determined by the mean free flight path for a particle. This

flight path is dependent on the calculation method set as input in SRIM; in our work we use the *monolayer collisions steps*, where the mean free flight path depends on the atomic density N of the target surface: $N^{-1/3}$. For each collision, a random impact parameter is generated and from this impact parameter the scattering angle and the corresponding energy loss is determined. The next collision is again at the mean free flight path; if this next collision is located above the surface, the particle is declared backscattered and the position, energy, and direction are recorded. If the particle does not leave the target surface, the simulation for a particle is stopped when the kinetic energy is not enough anymore to displace a target atom and this last position is recorded.

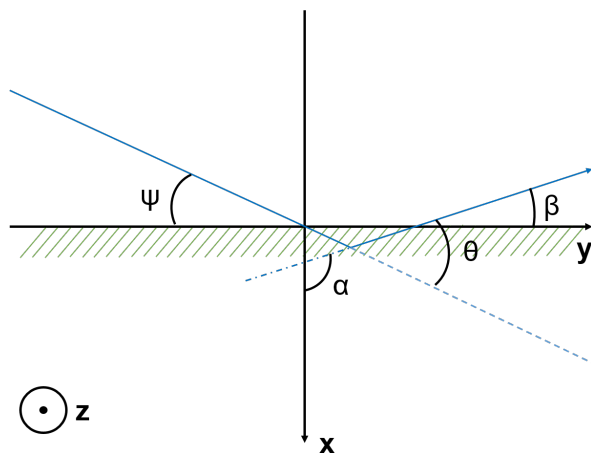


Figure 4.21: The coordinate system SRIM uses to describe the trajectories of the particles and the trajectory of a scattered particle as example (blue). The x -axis is pointing inwards the surface, the yz -plane is the surface plane. The direction of the particle is described in α , β , and γ , the angles with respectively the x -, y -, and z -axis. As γ is initially always 90° , the z -axis is not shown. The incidence angle ψ and the scattering angle θ used in the experiments are shown as reference.

The SRIM-spectra presented are extracted from the *BACKSCAT.txt*-output file. For every particle which SRIM declares backscattered, it records the last position in the target in three coordinates (x , y , and

z), the energy, and the direction of the atom as the cosine of the angle with respect to the x -, y -, and z -axis (from now on referred to as $\cos(\alpha)$, $\cos(\beta)$, and $\cos(\gamma)$; see also figure 4.21). The origin is defined as the entrance point of the ions in the surface: x and z are always 0, while y can have a value close to, but deviating from, 0. The x -axis is defined as the axis perpendicular to the surface plane, with the positive x -axis pointed into the surface. A backscattered ion will therefore always have negative values for $\cos(\alpha)$. The value of α is required to be set as input. In SRIM, the particles move in the xy -plane at the entrance in the surface. $\cos(\gamma)$ will therefore be initially 0, and β_{in} is determined by α_{in} : $\beta_{in} = 90^\circ - \alpha_{in}$. In our experiments we define the incidence angle as the angle with respect to the surface, so $\psi = \beta_{in}$. The detection angle (θ) is in our experiments the angle between the ion beam and the outgoing angle of the particle. This angle is in SRIM determined by the incidence angle and the angles α, β :

$$\cos(\theta) = \sin(\psi) \cos(\alpha_{out}) + \cos(\psi) \cos(\beta_{out}). \quad (4.28)$$

With the energies and the detection angles of the backscattered particles, a backscattering energy distribution can be emulated for comparison with the experimental results.

Chapter 5

Backscattering of tin ions from a molybdenum surface

The scattering of tin ions from a molybdenum surface is studied. The experiments show that the energy distributions are dominated by multiple collision scattering, leading to a broad energy spectrum. We compared the results with the predictions of a popular simulation package, SRIM. These predictions are in agreement with the experimental data, except for a pronounced single-scattering peak in the simulations. We conclude that the presence of the strong single-scattering peak has SRIM-related causes, such as ignoring the interaction above the surface. The fact that SRIM shows very similar results for the multiple collision spectra implies that the interaction inside the surface is simulated reasonably well.

5.1 Introduction

In modern nanolithography machines, 13.5 nm extreme ultraviolet (EUV) light is provided by an intense laser-produced tin plasma source which contains tin ions with charge states up to 14+ [11]. From this EUV light source, tin ions with kinetic energies up to dozens of keV are emitted [11] (see also chapters 2 and 3). If the ions are not mitigated, they will interact with the neighbouring walls and Mo/Si multilayer collector mirror [18]. The interaction between projectile atoms and surfaces can be simulated in order to understand and predict the consequences of this interaction.

Many simulation packages exist [121, 122], one commonly used for these kind of simulations is SRIM [98]. This package allows a wide range of energies and incidence angles for incoming particles, and simulates the particle stopping in the target, the trajectories and range, and the backscattered and sputtered particles emitted from the surface. The target can have single and multiple layers, and those layers can be a mixture of different isotopes. SRIM does not consider charge in its simulations, but treats both the projectile as well as the target as neutral atoms. A detailed description of SRIM can be found in chapter 4.

Many experimental tests on the output of SRIM are conducted, but this was mainly for sputter yields [123, 124, 125], for stopping power data [126, 127], and for low-Z ions [128, 129]. Tests of the simulations for scattering from the surface are uncommon but existing [130, 131], but also mainly for light ions. Qualitatively SRIM produces a good agreement with the experimental data in those tests, but significant differences in yield are often found. Also deviations in the angular distribution of the sputter yield are found, and the simulations do not agree with the experiments for ion beams below 1 keV (e.g. see ref. [125]). An extensive comparison of the SRIM predictions to the experimental energy distributions of backscattering for heavy ions on a heavy surface, such as tin on molybdenum, appears to be missing.

The goal of this work is to investigate the backscattering of tin ions from a molybdenum surface. We compare these results with the predictions by SRIM, and investigate the limitations and the range where the simulations are applicable for ion-surface collisions of relatively heavy ions. This gives more insight in these collisions and its underlying processes, and the extent to which SRIM can be used to simulate accurately

the interaction with the topmost surface layers of the target.

We record the scattered ion energy distribution for kinetic energies up to 14 keV, for a wide range of incidence and scattering angles. Also included is an investigation into the influence of charge state as a parameter, and comparison is made with other ion beams and target surfaces. We find some distinct deviations in the simulations from the experimental data which can only be explained by limitations of the software package.

5.2 Tin ion scattering

5.2.1 Experimental procedure

The experimental setup is described in detail in chapter 4, as is the ion source. In this chapter, we discuss the results of tin ion scattering experiments. The incidence angles (ψ) with respect to the surface range from 5° to 30° and the scattering detection angles (θ) range from 10° to 60° (see figure 4.21 for angle definition). The main target used in this work is a polycrystalline molybdenum surface, prepared by Surface Preparation Lab (SPL). Molybdenum has seven naturally abundant isotopes, with an average mass of 95.9 amu. A tin ion, which is heavier than molybdenum, has therefore a maximum scattering angle of 53.1° for a molybdenum atom of average mass, and 56.4° for the heaviest molybdenum isotope (^{100}Mo). Another target used for comparison to Mo is a ruthenium target. The main beam is a 14 keV $^{120}\text{Sn}^{2+}$ ion beam, which is decelerated to various kinetic energies, down to 3 keV. Other beams include tin beams with 1+ and 4+ as charge states, Kr⁺ beams, and Xe²⁺ ion beams.

Each measurement consists of several individual, summed energy scans. The number of individual energy scans in each measurement differs but is at least three. A single spectrum measures between a pre-set minimum and maximum E/q , with a set energy step size. For every energy point, the counts per second and the beam current on target are recorded. The total sum of counts per second is divided by the accumulated beam current on the target for each point and divided by the energy, to account for the energy resolution of the ESA. For tin ions, also a correction for the MCP tin ion detection efficiency is performed. The measurements are taken with voltages on the front of the MCP of -50V and -1000V, which

have a different ion detection efficiency and amount of background counts. The yield is normalized on the maximum in the summed spectrum.

5.2.2 Typical tin scattering results

In figure 5.1, the tin ion scattering spectra for three different energies of Sn^{2+} ion beams are shown, where ψ is 5° and θ is 10° . The 3 and 6 keV beams are produced by decelerating a primary 14 keV beam. For these shallow incidence and detection angles the energy distributions are relatively sharply peaked. The final energy of a scattered atom can be calculated with equation 4.4:

$$E_f/E_0 = \left(\frac{\cos(\theta) + \sqrt{(m_t/m_p)^2 - \sin^2(\theta)}}{1 + m_t/m_p} \right)^2. \quad (5.1)$$

A tin ion scattering 10° from a molybdenum atom retains roughly 0.96 of its initial energy in an elastic collision. In our experiments, the maximum yield is just above this value. At first, an ion approaching the surface has a large impact parameter with respect to the atoms at the top layer of the surface. They all act with a small repulsive force upon the projectile ion, resulting in a smaller grazing incidence angle, which is called *pre-scattering*. This can result in a small angle change before a collision with a larger scattering angle scatters the ion over 10° . The ion loses in total less energy compared with a single collision of the same angle, and can retain therefore an energy of more than 0.96 of the initial energy. Due to energy loss in the surface (straggling), tin ions which collide deeper in the surface lose energy, both on the way in and out, resulting in a long low-energy tail of the distribution. Possible low-Z contamination and surface roughness may contribute to some additional spectral broadening. The yield increases for increasing ion beam energy, but the shape itself does not significantly change between the three beam energies.

Figure 5.2 shows two series, one for a constant incidence angle ψ of 5° (upper) and another for a constant scattering angle θ of 45° (lower). For all measurements, an ion beam of 14 keV Sn^{2+} is used. The constant ψ series shows the spectra for an increasing θ : 10° , 20° , 30° , and 45° . As the detection angle increases, the ion energy distributions peak at lower energies and the maximum energy is lower, as larger scattering angles

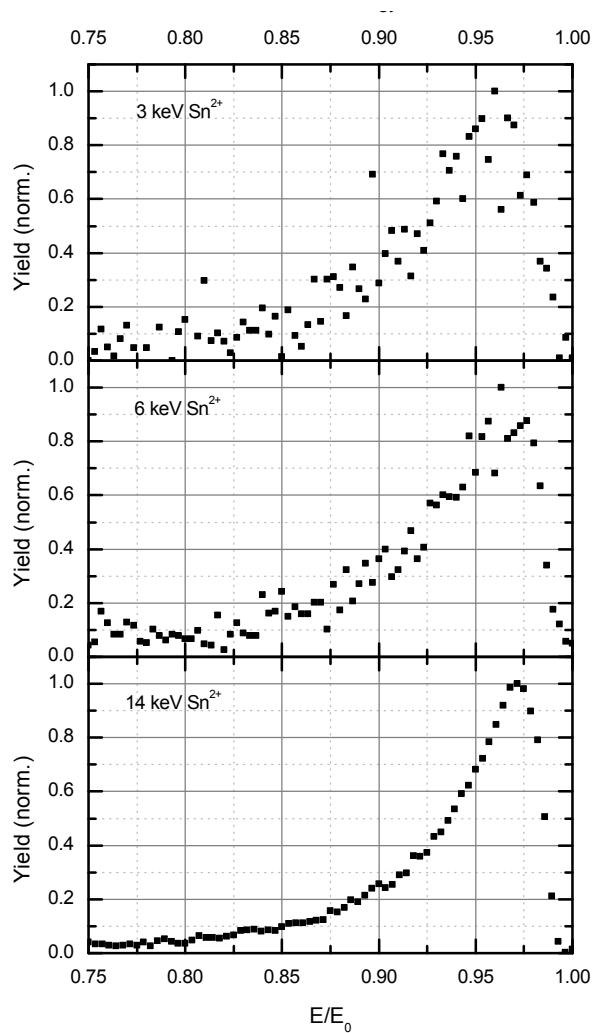


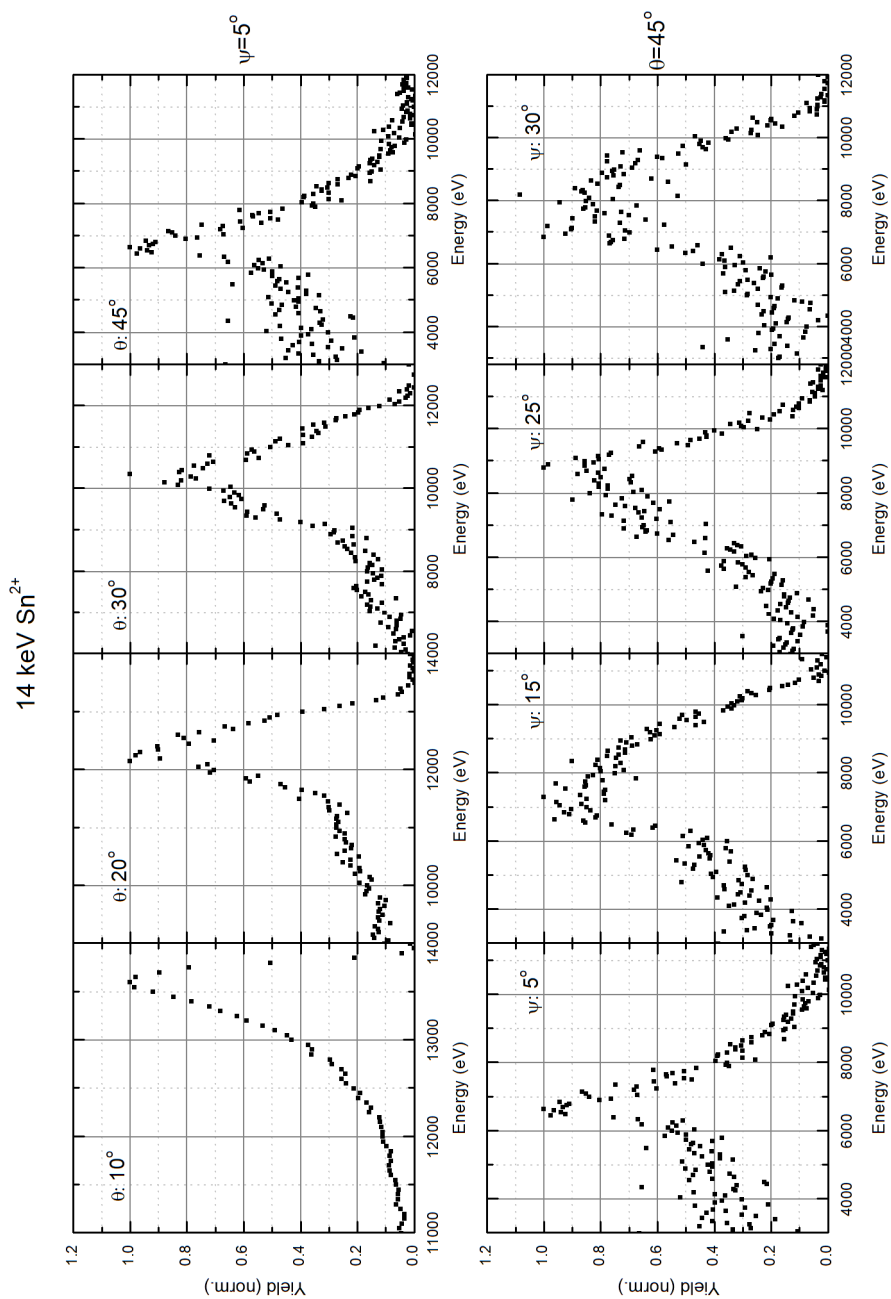
Figure 5.1: The ion scattering spectra for three initial kinetic energies (E_0): 3 keV, 6 keV, and 14 keV Sn^{2+} at ψ is 5° and θ is 10° . The energy is relative to the initial kinetic energy of the ion. The spectra are corrected for the background.

require more loss of energy. More combinations of scattering angles in multiple collision scattering are possible for larger detection angles, and the pathway through the target can become longer before the ion leaves the surface. This results in broader spectra: where for 10° almost all detected ions are within a relatively narrow range of 3 keV, the distribution spans a range of more than 7 keV for 45° .

The constant θ series, with $\theta = 45$, shows the spectra for ψ is 5° , 15° , 25° , and 30° . The spectrum with the smallest incidence angle has the sharpest peak, and that peak is located at a lower energy than in the other three spectra, between 6.5 and 7 keV. For $\psi = 15^\circ$ and 30° , the maximum yield is at energies between 7 and 8 keV, while for $\psi = 25^\circ$ the maximum is between 8 and 9 keV. The maximum recorded energy is also higher for this incidence angle, at 11.5 keV, while for an incoming angle of 15° and 30° the maximum energy is at 11 keV, and even at a little bit lower energy for $\psi = 5^\circ$. For near-specular incidence and detection angles ($\theta \approx 2\psi$), the energy distributions in our experiments are in general broader and have a higher yield. In the constant θ series of figure 5.2, this is the case for $(\psi, \theta) = (25, 45)$. For such spectra, more combinations of multiple collision scattering with smaller individual collision angles are possible, leading to higher kinetic energies of the scattered ions. The energy for double collision scattering with one scattering angle equal to the incoming angle and the other equal to the outgoing angle is often a good predictor for the maximum energy of the broad peak, so at which energy the yield decreases for increasing ion energy. For the constant θ series in figure 5.2, the so-defined double-collision energy is at respectively 7 keV, 9 keV, 9.5 keV, and at 9 keV for ψ is 5° , 15° , 25° , and 30° .

The $(\psi, \theta) = (15, 45)$ and the $(\psi, \theta) = (30, 45)$ energy distributions, where the incoming angle of the one is equal to the outgoing angle of the other, are strikingly similar. Such symmetric cases produce in our experiments always the same distribution, except if the incidence angle is grazing at 5° . In those grazing incidence cases the interaction with the surface before entering and after leaving the target is of such importance for the scattering that the spectra have different shapes. For further discussion of symmetric cases, see section 5.3.6.

Target atoms sputtered from the surface layers in one collision are

Figure 5.2: Compilation of spectra of 14 keV Sn²⁺ scattering of Mo.

called primary recoils, and have a well-defined energy (see section 4.1.1):

$$E_{rec}/E_0 = \frac{4m_t m_p}{(m_t + m_p)^2} \cos^2(\varphi). \quad (5.2)$$

Primary molybdenum recoils sputtered over 45° by 14 keV tin atoms gain 6.9 keV. The yield is slightly enhanced around this energy in figure 5.2, a feature shared with most of the energy distributions in this work. A tin ion scattered over 45° by molybdenum retains 40% of its initial energy, or 5.6 keV. All four spectra with $\theta = 45^\circ$ attain their maximum yield at higher ion energies. Also the spectra in the constant ψ series peak at energies higher than the energy required for a single collision, except for the (5,10) combination. This shows that the ion scattering distributions are dominated by multiple collision scattering and have a pathway through, and therefore interaction in, the sample before leaving the target surface. Backscattering can therefore be used to investigate the interaction inside the surface. We will compare the spectra with the output of the simulations of SRIM, and investigate the accuracy of this simulation package.

5.2.3 SRIM simulations

The final energies and the directions (the cosines of the SRIM-angles α , β and γ , see figure 5.3) of the backscattered particles are extracted from the output file. For comparison to the experiments, the backscattered particles are required to be in the xy -plane (the ion beam-detector plane in the experiments) by imposing a 3° -limit on γ : γ should be between 87° and 93° . The detection angle (θ in the experiments), the angle between the ion beam and the outgoing angle of the particle, is determined by the incidence angle and the angles α, β

$$\cos(\theta) = \sin(\psi) \cos(\alpha_{out}) + \cos(\psi) \cos(\beta_{out}). \quad (5.3)$$

Only particles which are within a certain limit of the detection angle are taken into account: for detection angles smaller than and equal to 40° this limit is 1° , for larger angles the limit is 2.5° . A histogram of the final kinetic energies of the particles which pass these angle tests emulates an experimental spectrum and can be compared with the experimental results. The simulations are normalized to the maximum of the experimental energy distributions.

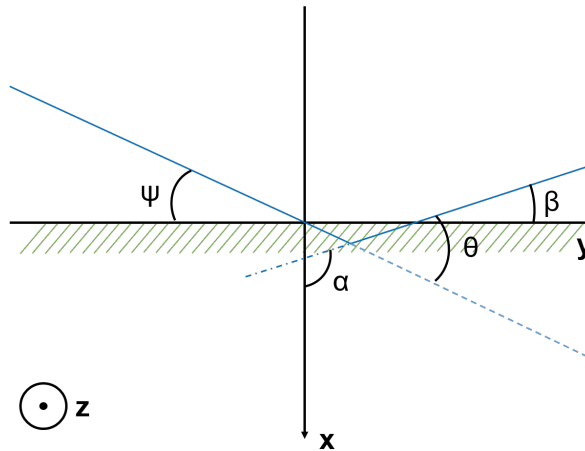


Figure 5.3: The coordinate system SRIM uses to describe the trajectories of the particles and the trajectory of a scattered particle as example (blue). The x -axis is pointing inwards the surface, the yz -plane is the surface plane. The direction of the particle is described in α , β , and γ , the angles with respectively the x -, y -, and z -axis. As γ is initially always 90° , the z -axis is not shown. The incidence angle ψ and the scattering angle θ used in the experiments are shown as reference.

We select the isotopes used in the experiments as incoming ion in SRIM: for tin this is ^{120}Sn . As target surface we use, unless otherwise specified, a mixture of the seven naturally abundant isotopes of molybdenum weighted by the abundance ratio. This will lead to spectral broadening of the energy distributions, and especially of the single scattering peaks, compared to a target surface where the average mass is used. As calculation method we use *monolayer surface collisions*, which is recommended for ion-surface interactions near the edge of the surface. We simulate six million particles for each spectrum, unless otherwise specified.

5.3 Results

In figure 5.4, the energy distributions from the experiments for three (ψ, θ) combinations are compared to the predictions of corresponding SRIM sim-

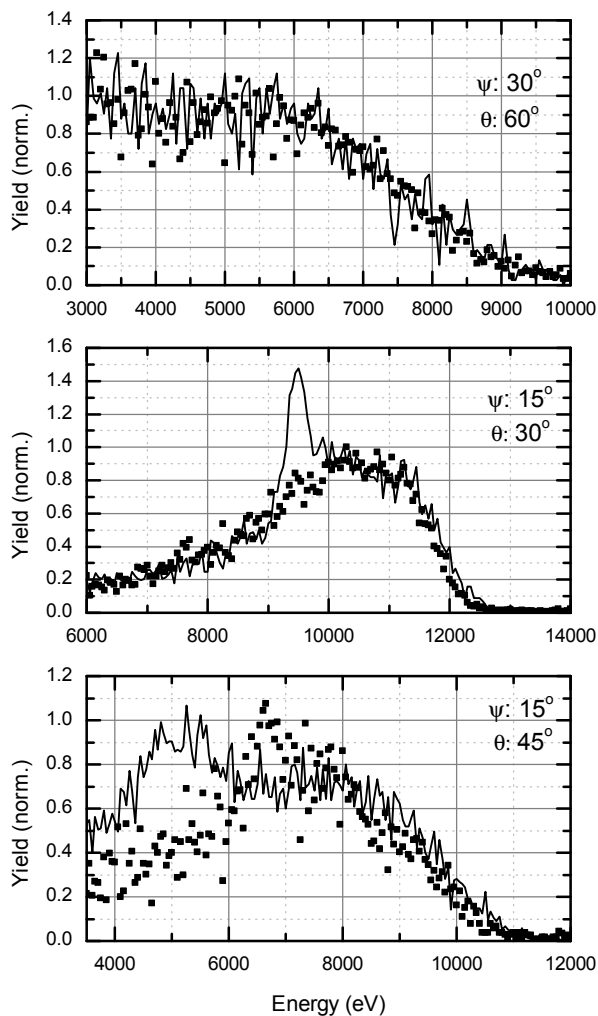


Figure 5.4: The ion scattering spectra (dots) and the corresponding predictions (line) by SRIM for a 14 keV Sn^{2+} ion beam for three combinations of ψ and θ : from top to bottom, (ψ, θ) is $(30, 60)$, $(15, 30)$, and $(15, 45)$.

ulations. The experimental energy distribution for $(\psi, \theta) = (30, 60)$ is in excellent agreement with the simulations, for both the yield as well as

the maximum ion energy. For the other two cases, the broad distribution typical for our experimental spectra is also visible in the SRIM-predictions, although the simulations expect a higher yield for the high-energy tail of both spectra, and for the low-energy part of the (15,45)-distribution. The predicted maximum ion energy is in agreement with the experiments for both spectra.

An additional peak on top of the broad distribution is apparent in the simulations. This peak is located at the energy of a tin ion after a single collision from a molybdenum atom, at 9.6 keV for $(\psi, \theta)=(15,30)$ and at 5.1 keV for $(\psi, \theta)=(15,45)$. Further analysis of the trajectories of the simulated particles indicates that the particles in this peak are the result of a single collision in the upper layer of the surface. Due to a smaller scattering cross section for large angles, the peak is smaller for larger angles. For $(\psi, \theta)=(30,60)$, single collision scattering over 60° is not possible as the maximum scattering angle is around 53° for tin on molybdenum.

The single-collision peak appears in nearly all investigated combinations of ψ and θ , but no trace of it is visible in any of the experimental energy distributions. In the next sections, we will step-wise discuss six possible parameters which may cause this discrepancy:

1. Charge state: we vary the charge state of the ion beam to look for any charge state dependent features in the energy distributions.
2. Ion species: we compare the energy distributions with the simulations for two other heavy ion beams, krypton and xenon, to get insight in the importance of the ion species on the results.
3. Electronic structure: we discuss the outcome of interatomic potential calculations and scattering distribution simulations for ^{124}Xe and ^{124}Sn , which have the same mass but very different ionization energies and electronic structure.
4. Target surface: potentially, the origin of the differences between the experiments and the simulation might stem from the characteristics of the target surface. We show the results for tin scattering experiments on a ruthenium target surface.

5. Differences between ions and neutrals: with the ESA, we can only measure charged particles. We make a comparison of the ESA results with the results of a Time-of-flight (TOF) measurements, which also measures neutral particles.
6. SRIM-related reasons: concluding, we discuss the various ways the simulation package can lead to deviations from experimental observations.

The possible role of surface contamination is discussed in chapter 6.

5.3.1 Charge state

In figure 5.5, the results are shown of scattering of 5 keV and 14 keV tin beams for two charge states: 1+ and 2+ for the 5 keV beam, and 2+ and 4+ for the 14 keV one. The 5 keV Sn^{2+} beam is decelerated from a primary beam of 14 keV Sn^{2+} and the 14 keV Sn^{4+} beam from 28 keV Sn^{4+} . The other two beams are both primary beams. For all spectra, the target angle ψ is 15° and the detection angle θ is 35° . Both 5 keV spectra maximize around 3.7 keV and the maximum kinetic energy of the scattered ions is at 4.5 keV, respectively roughly 75% and 90% of the initial energy of the ions. There are no differences visible comparing both spectra. Both the 14 keV spectra for Sn^{2+} and Sn^{4+} have a maximum around 10.5 keV (or 75%) and have a maximum energy at 12.5 keV (roughly 90%). For the Sn^{2+} ion beam, the yield at 9 keV is slightly higher than for the Sn^{4+} ion beam, which is near the energy for primary molybdenum recoils over 35° (9.15 keV).

The results for different charge states are very similar for both energies, bar some minor deviations. We conclude therefore that there is no significant charge state dependency for tin ion scattering. It is unlikely that any deviations between the experimental results and the SRIM predictions are caused by the fact that SRIM does not consider charge in its simulations. Also oscillatory charge exchange effects [132], where the single scattering yield for single-charged ions are found to have a periodic dependence on the inverse ion velocity but double-charged ions not, can be ruled out.

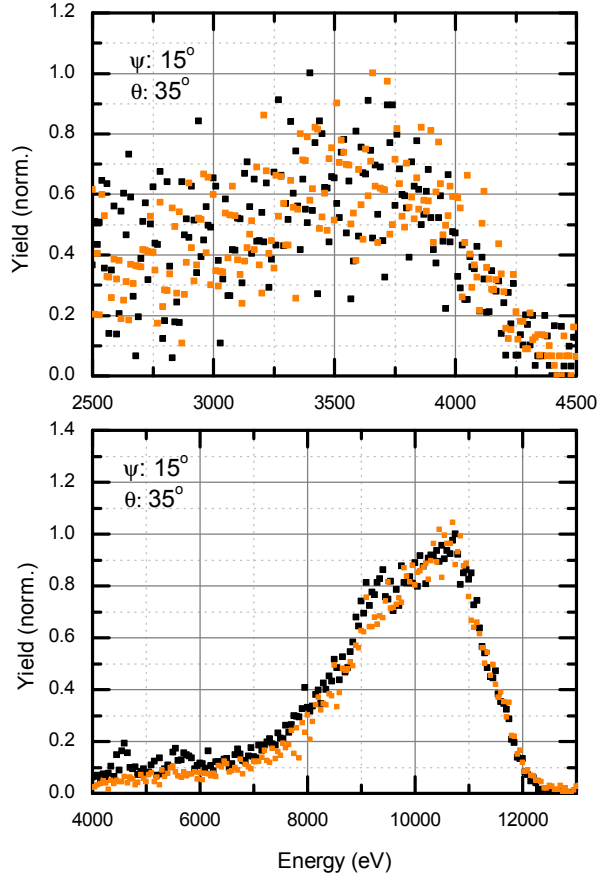


Figure 5.5: (top) The ion scattering spectra for a 5 keV Sn^+ (black) and Sn^{2+} (orange) ion beam for $\psi = 15^\circ$ and $\theta = 35^\circ$. (bottom) The ion scattering spectra for a 14 keV Sn^{2+} (black) and Sn^{4+} (orange) ion beam for $\psi = 15^\circ$ and $\theta = 35^\circ$.

5.3.2 Ion species

To exclude the possibility that the absence of the single scattering peak is purely a tin-related feature, we investigate the scattering of krypton and xenon ions from the molybdenum surface. Where tin atoms, with

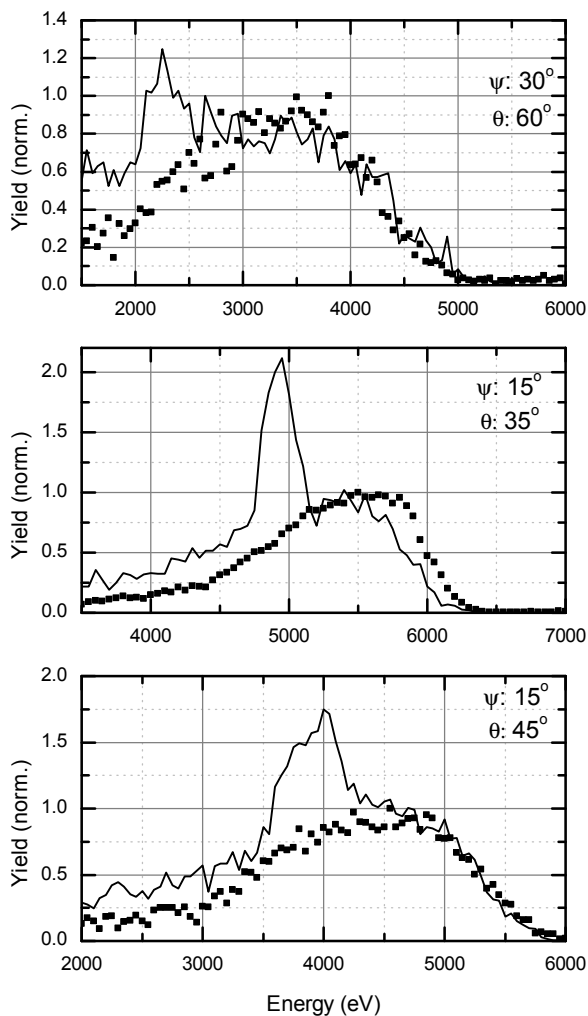


Figure 5.6: The ion scattering spectra (dots) and the corresponding predictions (line) by SRIM for a 7 keV Kr^+ ion beam for three combinations of ψ and θ : from top to bottom, (ψ, θ) is $(30, 60)$, $(15, 35)$, and $(15, 45)$.

an average mass of 118.7 amu, are heavier than molybdenum atoms (95.9 amu on average), krypton is with an average of 83.8 amu a bit lighter

than the target atoms. We use a 7 keV $^{84}\text{Kr}^+$ ion beam, which has a similar ion velocity as the 14 keV $^{120}\text{Sn}^{2+}$ ion beam we primarily use in the tin on molybdenum experiments. In figure 5.6, the results of these krypton scattering experiments and the corresponding SRIM predictions are shown for three combinations of incidence and detection angles: (ψ, θ) is (30,60), (15,35), and (15,45). As krypton is lighter than molybdenum, single scattering is possible over all angles. A krypton ion scattering 60° from a molybdenum surface retains roughly 34% of its energy, or 2.4 keV for a 7 keV krypton beam. This single scattering peak is visible in the simulations as a small peak on top of the large broad distribution, but is not visible in the experimental energy distributions. For this particular combination of angles, the simulations are in excellent agreement with the experiments for tin scattering. This is a significant result: the differences between the experiments and the simulations are still apparent for large angles if single scattering is energetically possible. This makes it unlikely that surface irregularities such as roughness, which affect results less for larger angles, are responsible.

Even more pronounced than for Sn ions, the simulations show the typical single scattering peak at 5 keV and 3.9 keV for respectively (ψ, θ) is (15,35) and (15,45), which are not apparent in the experiments. For both combinations, the yield of lower energy ions is significantly lower in the experiments compared to the predictions by SRIM. The energy distribution for (15,35) has a higher yield of higher energy ions, above 5.5 keV. The cause for this is unknown and is not observed in the other energy distributions investigated.

Figure 5.7 shows the energy distribution for a 14 keV $^{132}\text{Xe}^{2+}$ beam, incident at 15° on the surface and the detector at 35° , and its corresponding SRIM predictions. The single scattering peak, at 54% or 7.5 keV, apparent in the tin scattering simulations is also present in the simulations for xenon, but not visible in the experimental results. Also for the xenon ion distributions, the yield in the low-energy tail is lower than predicted by SRIM.

For both krypton as xenon, the results compared to the simulations are very similar to the tin-experiments. The absence of the single scattering peak in the energy distributions is not a tin-specific feature, but is shared with other ion species. Furthermore, the absence of the peak is

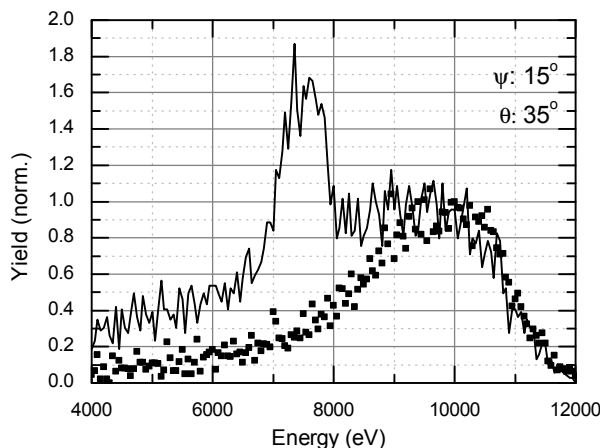


Figure 5.7: The ion scattering spectrum (dots) and the corresponding SRIM predictions for a 14 keV Xe^{2+} ion beam for $\psi = 15^\circ$ and $\theta = 35^\circ$.

also apparent in krypton scattering distributions for large angles, where single scattering from molybdenum is not possible for tin.

5.3.3 Electronic structure

Xenon has an average mass of 131.2 amu, which is only slightly higher than the average mass of tin and the difference in mass is not expected to make much difference in the experiments and the simulations. The electronic structure of xenon is very different from that of tin, however. Xenon is a noble gas and is therefore inert, has fully filled electronic shells, and has higher ionization energies. As discussed in the previous section, the results of the scattering experiments of the $^{132}\text{Xe}^{2+}$ ion beam do not differ from the results for tin.

To make visible which differences and similarities a different electronic structure causes in the predictions of SRIM, we simulated the scattering for an isotope of the same mass of 124 amu, which is naturally abundant for both xenon and tin. The results of these simulations are shown in figure 5.8. There is almost no difference between both spectra, and include a single scattering peak around 8 keV. Figure 5.8 shows the ZBL-potential, the repulsive interatomic potential most commonly used in computer sim-

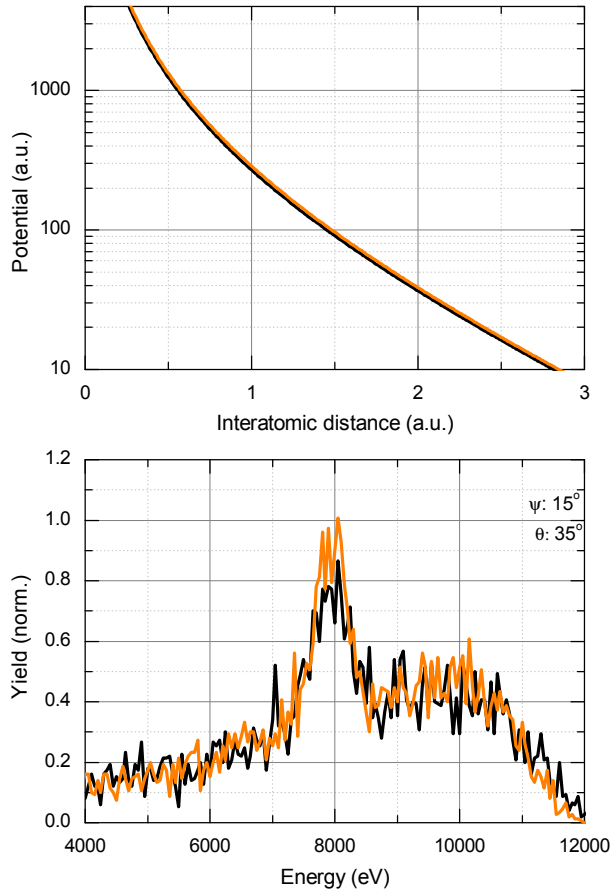


Figure 5.8: (top) The ZBL-potential between molybdenum and tin (black) and xenon (orange). (bottom) The SRIM predictions for $\psi = 15^\circ$ and $\theta = 35^\circ$ for 14 keV Sn (black) and Xe (orange), but with an atomic mass of 124 amu.

ulations such as SRIM, between molybdenum and tin and xenon. This potential is independent of the mass of a particle but does depend on the nuclear charge, which is 50 and 54 for respectively tin and molybdenum. There is a small difference between the Sn-Mo potential and the Xe-Mo potential, where the latter is slightly higher. The Coulomb repulsion part

is 8% higher, and the screening length is 1% smaller (0.1820 for Xe-Mo and 0.1836 for Sn-Mo). These minimal differences in the potentials do not have a significant influence on the scattering and ion energy distributions, as can be seen in figure 5.8. It is therefore unlikely that the electronic structure causes the differences between the SRIM-spectra and the experimental energy distributions.

5.3.4 Target surface

To test the influence of the surface on the experiments we use a ruthenium target. Ruthenium is slightly heavier than molybdenum, with an average mass of 101 amu. Ions scattering from ruthenium have therefore a higher kinetic energy for the same scattering angle compared with ions scattered from molybdenum. The maximum scattering angle is larger, with $\theta_{max} = 57.3^\circ$ for tin scattering from a ruthenium atom with average mass, and 60.1° for the heaviest isotope. The element has 7 stable and naturally abundant isotopes, ranging from 96 to 104. The target in the SRIM simulations in this work is, as it was for molybdenum, a mixture of these isotopes with the appropriate abundance ratio.

The results of a 14 keV Sn^{2+} ion beam scattering from ruthenium are shown for three combinations of incidence and detection angles, (ψ, θ) is (30,60), (15,35), and (15,45), in figure 5.9. All three ion energy distributions are relatively broad, indicating that they are dominated by multiple collision scattering. The predictions by SRIM are in excellent agreement with the experimental results for (ψ, θ) is (30,60), as it was for the tin scattering from molybdenum for this combination of angles. For the (15,35) combination, the broad energy distribution typical for multiple scattering is also visible in the simulations, although SRIM expects a higher yield for the low-energy tail. Similar to the SRIM predictions for scattering from molybdenum, a high-yield single scattering peak is expected for ruthenium in the simulations. This peak, at roughly 60% or 8.5 keV of an original 14 keV beam energy, is absent in the experimental ion energy distributions. We obtained similar results for an incidence angle of 15° and a detection angle of 45° . The single scattering peak is located at 5.6 keV, or 40% of the initial ion energy, but does not appear in the experiments. Apart from this single scattering peak, the experimental energy distributions are in agreement with the simulations.

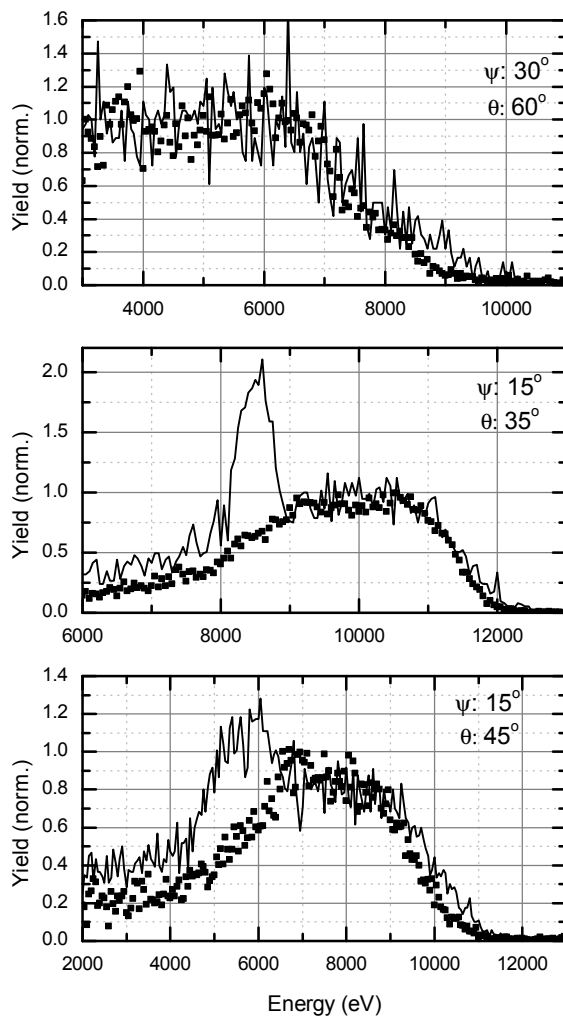


Figure 5.9: The ion scattering spectra (dots) and the corresponding predictions (line) by SRIM for a 14 keV Sn^{2+} ion beam on a Ru target for three combinations of ψ and θ : from top to bottom, (ψ, θ) is $(30, 60)$, $(15, 35)$, and $(15, 45)$.

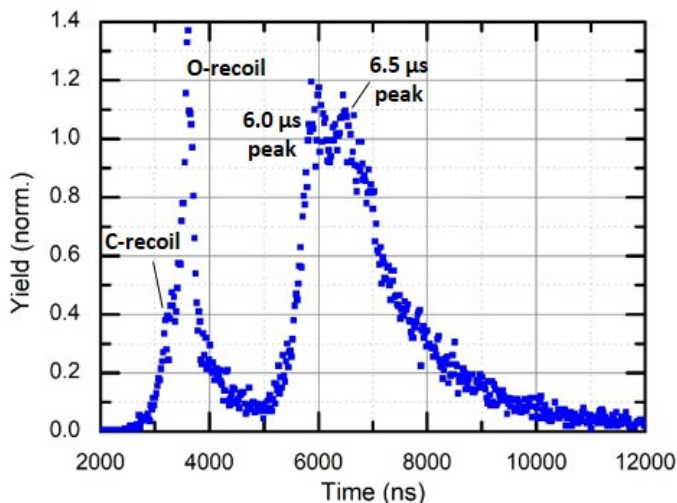


Figure 5.10: The TOF spectrum for a pulsed 14 keV Sn^{2+} ion beam on a Ru target for ψ is 15° and θ is 40° .

The results, and the comparison between the experiments and the simulations, for tin scattering on ruthenium are very similar compared with the scattering on molybdenum. It should be noted that ruthenium and molybdenum have similar masses; a heavier or lighter target will obviously change the results. However, in this target mass range the target does not significantly influence the results of the scattering experiments and does not explain deviations between the simulations and the experiments for the scattering from molybdenum.

5.3.5 Difference in ions and neutrals

The ESA does not measure any neutral particles. To be able to measure (neutral) atoms, we pulse the beam with a sweeper-chopper system and detect the particles with a channeltron at the end of a time-of-flight (TOF) tube. This channeltron is located at 740 mm from the target. The detector records both ions as well as neutral particles; the TOF tube can be floated on a high voltage to accelerate or decelerate any ions while the atoms are not affected. The time elapsed between the start trigger of the

chopping voltage and the stop trigger given by the detector is recorded by the computer. This time can be used to determine the TOF of the particle between the target and the detector, which is related to the energy of the particle.

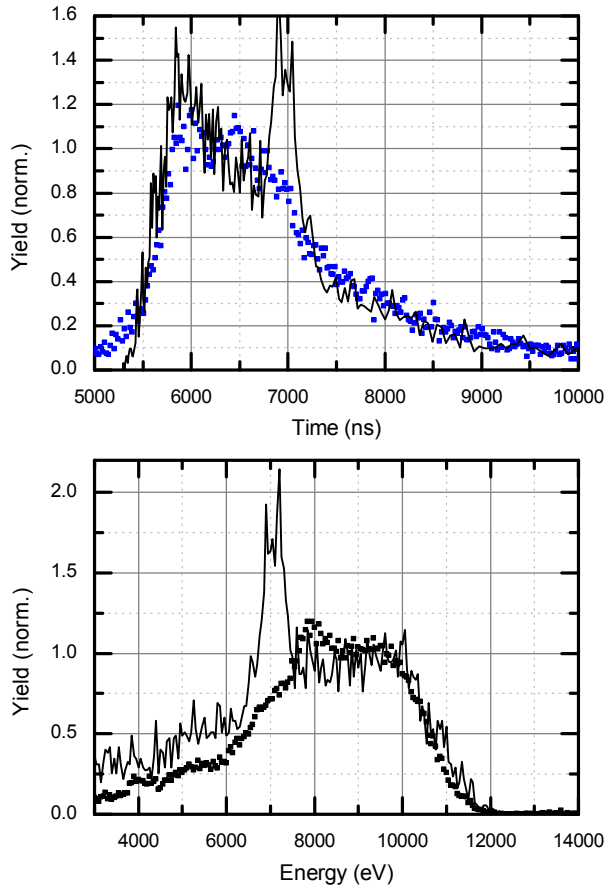


Figure 5.11: The TOF spectrum (blue dots, top), the ESA distribution (black dots, bottom), and the corresponding SRIM predictions (line) for a 14 keV Sn^{2+} ion beam on a Ru target for (ψ, θ) is $(15, 40)$.

In figure 5.10, the TOF spectrum of a 14 keV Sn^{2+} beam on a Ru target is shown, for an incidence angle ψ is 15° and a detection angle θ of

40° . The yield is normalized and the spectrum is corrected for the delay induced by the chopping and detection electronics, and the TOF between the sweeper-chopper system and the target. Two peaks are visible: a sharp peak around $3.5 \mu\text{s}$ and a broad peak between 5 and $10 \mu\text{s}$. The flight times of the particles for the sharp peaks are too short to belong to backscattered tin, as tin has to gain energy to attain those flight times. The TOF corresponds to the primary recoil energy of an oxygen sputtered over 40° (3.4 keV , see equation 4.5). A small additional peak is visible on the short-TOF tail of the oxygen peak, which corresponds to the energy of primary carbon recoils (2.7 keV). The sharp peak is therefore the result of low- Z contamination at the surface. This peak is not apparent (when the recoil energy was in range) for the pure ion energy distributions measured with the ESA, which suggests that the ionization degree of this contamination is significantly lower than the ionization degree of tin or that the target had less contamination for those measurements.

The broad peak in the TOF spectrum corresponds to energies for backscattered tin earlier seen in ESA measurements and SRIM simulations. It has a sharp rise for the shorter flight times (corresponding to higher kinetic energies), a broad maximum, and a long-TOF tail. The maximum seems to be double-peaked, with peaks at roughly 6 and $6.5 \mu\text{s}$. Figure 5.11 shows the distributions obtained, for the same ion beam and detection angle, with the ESA and the TOF measurements, together with the corresponding SRIM simulations in both the time as well as the energy domain. The conversion for the results of SRIM from energy to time domain includes a correction in the yield for the non-constant bin size (see equation 2.1). Direct comparison of the ESA and TOF results is not prudent, as for conversion a well-defined atom mass is required. The ruthenium recoil peak and tin scattering peak overlap, so the atom mass is not defined for the distribution.

The yield from the TOF measurements is in good agreement with simulations. The TOF measurements have a higher yield for flight times around $5 \mu\text{s}$, which originates from the long-TOF tail (or low-energy tail) of the oxygen peak. For flight times longer than $7 \mu\text{s}$ the TOF yield is in good agreement with the SRIM simulations, while the ESA distribution has a significantly lower yield for lower energies. The low-energy tail of the ESA measurements in the previous sections has often a lower yield than

shown in the simulations of SRIM; possibly particles with higher energies are more easily ionized, skewing the energy distributions.

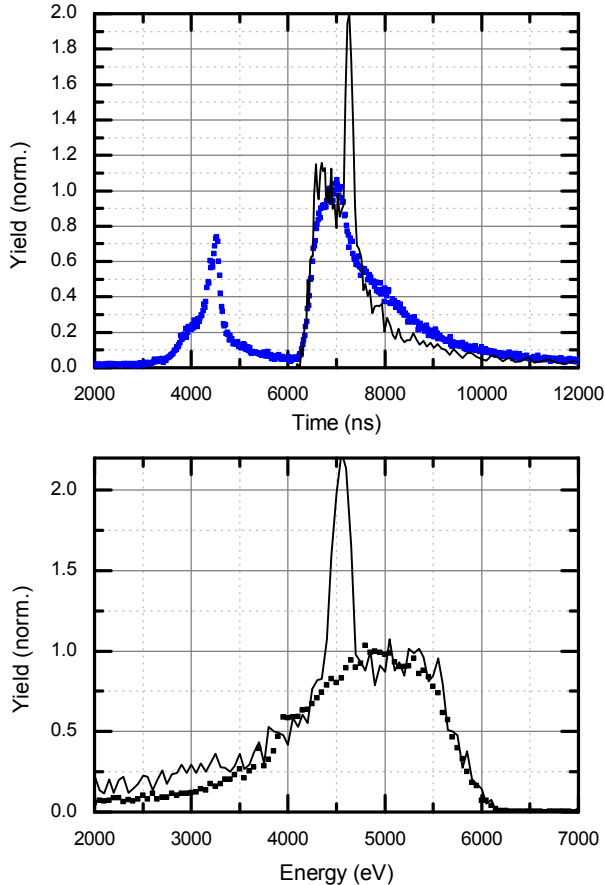


Figure 5.12: The TOF spectrum (blue dots, top), ESA distribution (black dots, bottom), and corresponding SRIM predictions (line) for a 7 keV Kr^+ ion beam on a Ru target for (ψ, θ) is $(15, 40)$.

The $6.5\text{-}\mu\text{s}$ peak corresponds to an energy for tin of roughly 8 keV in the energy domain. At this time and energy, both the TOF as well as the ESA measurements show a small peak, slightly higher than the yield in the SRIM predictions. The energy of primary ruthenium recoils at 40° is also

located at 8.2 keV, and can possibly appear in the ESA measurements at this energy. The TOF of these recoils is located at roughly 6 μs , which is at the other peak of the broad maximum in the TOF measurements. This complicates the interpretation of the results. The single scattering peak, visible as usual with a prominent appearance in the SRIM simulations, is located around 7.1 keV in the energy domain and 7 μs in the time domain. At this energy and time, only a small bump in the TOF and ESA measurements is visible, and it is certainly not as pronounced as in the SRIM predictions.

In figure 5.12, the results of TOF measurements, ESA measurements, and their corresponding SRIM simulations are shown for a 7 keV Kr^+ beam with ψ is 15° and θ is 40° . For krypton, the single scattering was very pronounced in the SRIM predictions, but not visible in the ESA measurements. The primary ruthenium recoils have an energy around 4.1 keV or a flight time of 8.4 μs , which are both outside the main broad peak in the time and the energy domain. The TOF spectrum shows the low- Z contamination around 4.5 μs which corresponds to the primary recoil energy of 1.8 and 2.2 keV of respectively carbon and oxygen. The TOF measurements are in reasonable agreement with the SRIM simulations, with a broad maximum between 6.3 and 7.5 μs . The low-energy tail of the low- Z contamination peak gives a larger yield for flight times smaller than 6.3 μs and above 7.5 μs the yield of the TOF measurements is significantly higher than the simulation results. Possibly primary ruthenium recoils are visible in the TOF spectrum, which gives a higher yield for longer flight times around 8.4 μs . The single scattering peak, located at 4.7 keV or 7.3 μs is not apparent in either the ESA or the TOF measurements. Deceleration of ions by floating the TOF tube on a 2 kV voltage did not lead to a significant change of the spectrum.

In conclusion, we investigated the neutral particles originating from two ion beams for which the single scattering peak has a prominent appearance in the SRIM simulations. For both ion beams, a distinct single scattering peak is not visible in the TOF or the ESA measurements. We conclude therefore that the absence of the single scattering peak in the experimental results does not originate from the fact that the ESA only measures ions, and not atoms.

5.3.6 SRIM-related reasons

In this section, we turn our eyes towards the simulation package, and see how it may produce deviations from the experimental data. In the past, wrong SRIM predictions for sputter yields and inaccurate angular distributions of sputtered ions were reported [117, 118], and also the electronic stopping power data of SRIM was criticized [119]. The agreement of the simulations with backscattering experiments was barely investigated, but also deviations mainly in the angular distribution of the scattering yield were noticed [131]. In the following pages, we will discuss our choice of SRIM calculation method, how SRIM determines the next collision, and the negligence by SRIM of interaction above the surface.

Three different calculation methods can be selected for the simulations: *monolayer sputtering*, *detailed calculation*, and *quick calculation*. In figure 5.13, the predictions of two (ψ, θ) combinations for a 14 keV tin beam on molybdenum are shown for those three methods. The results are very similar for both spectra: the single scattering peak typical for the SRIM predictions is visible for all three methods, and has approximately the same height. The single-scattering peak appears to be slightly broader for the quick calculation method for the (15,30) combination. The multiple collision part of the distribution is also in good agreement for all three calculation methods. This shows that the appearance of the single-scattering peak, and thus the deviation from the experimental results, persists even when a different calculation method is used.

In SRIM, the target is amorphous and does not have any crystal structure. The program determines the place of the next collision by calculating a mean free path length d of the incoming projectile, which is proportional to the inverse cubic root of the atom density N for the monolayer sputtering calculation method: $d = N^{-1/3}$. The projectile enters the surface in the simulations near the origin with a certain direction (the angle), and the first collision takes place at a distance d away from the origin. The particle will be declared backscattered if it is scattered in such a way that it is moving towards the edge of the surface and the next point of collision, at a distance d , is placed somewhere above the surface. However, this is only possible if the outgoing angle of the projectile, with respect to the target, is larger than the incoming angle. Otherwise, the particle is forced to have another collision, which increases the possibility of being

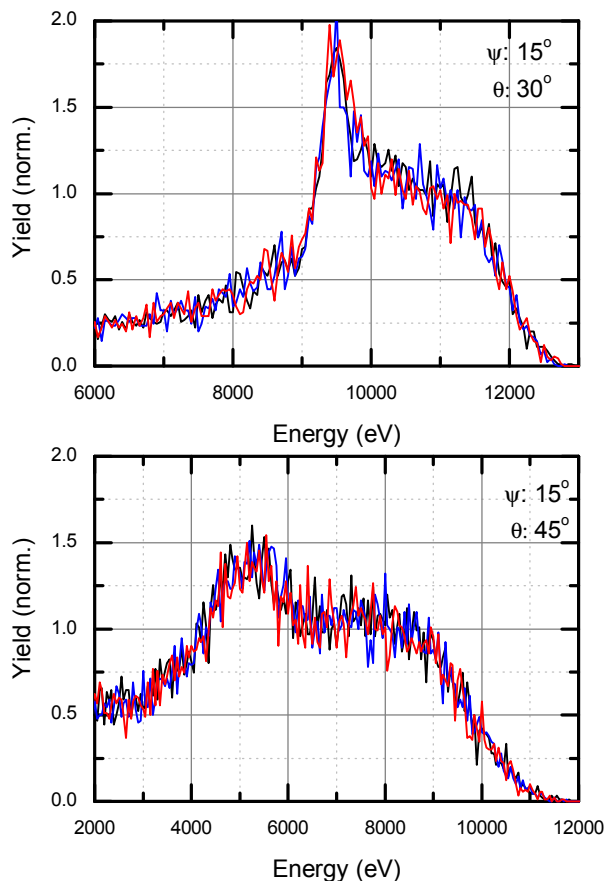


Figure 5.13: The SRIM predictions for a 14 keV Sn beam on molybdenum for (ψ, θ) is $(15, 30)$ (upper) and $(15, 45)$ (lower) for three different calculation methods: monolayer sputtering (black), detailed calculation (blue), and quick calculation (red).

scattered back into the surface or getting an even larger scattering angle. This is reflected in figure 5.14, where the results are shown for two cases of symmetric incoming and outgoing angles with respect to the target: (ψ, θ) is $(15, 35)$ & $(20, 35)$ and $(15, 45)$ & $(30, 45)$. For both cases the experimental results are very similar, except for a small peak around 9 keV

visible for (ψ, θ) is (15,35) but not for (20,35). This coincides with the primary recoil energy for molybdenum sputtered over 35° : 9.15 keV. On contrast, the simulations show a pronounced difference in the height of the single scattering peak and this peak has almost disappeared for (30,45). The single scattering peak, or quasi-single scattering peak if the incoming angle is larger than the outgoing angle, is lower for larger incoming angles. The peak height depends on the incoming angle's magnitude relative to the outgoing angle. Also visible is the spectral broadening of the peak for (20,35), which originates from where SRIM initiates the simulation and how it determines the next collision. For all investigated angular symmetric cases, the experimental distributions are in agreement with each other, but the simulations show a different (quasi-)single scattering peak. Novikov et al. [131] studied the angular distribution of backscattering yields and report a symmetric distribution around specular detection angles, while SRIM expected an asymmetry. This can be explained by how SRIM forces a collision at a fixed distance and disregards any surface structure. The combination of the initialization of the simulation at the surface and how SRIM determines the point of the next collision causes unreported and unexpected asymmetries in angular distributions.

A simulation of a single particle in SRIM is initiated at the edge of the surface, and only the interaction inside the target is considered. In reality, the interaction between the target and the ion starts at some distance in front of the surface. An ion approaching a surface can already be scattered over a small scattering angle at a large distance from the surface. Robin et al. [133] estimate the distance to the surface at which the ion experiences significant energy loss and therefore scattering. They obtain for nitrogen scattering from platinum in an energy range similar to ours a distance of 2.6 atomic units, for an incidence angle of roughly 5° . This distance decreases for larger incidence angles, but can not be ignored. The ion will be pre-scattered, which is always scattering towards the detector. This necessitates a smaller scattering angle to obtain the same total scattering angle as for a single scattering process, and will therefore lead to higher energies for the scattered ions. As there are many pathways with many potential final energies, the energy distribution is very broad for these quasi-single scattered ions, so there is no obvious peak visible and it will be indistinguishable from the multiple collision energy distribution. There

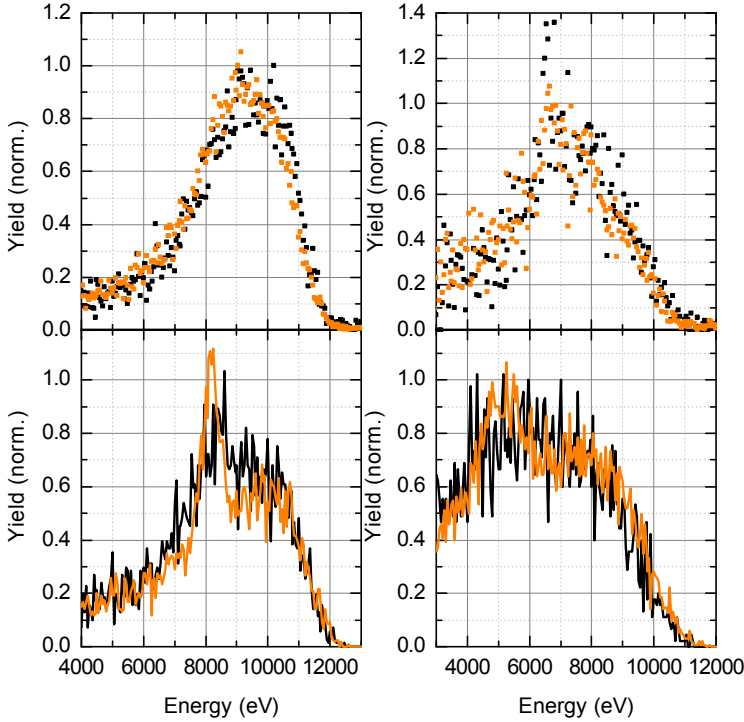


Figure 5.14: The ion scattering spectra (top panels) and their corresponding SRIM predictions (bottom panels) for a 14 keV Sn^{2+} ion beam on a Mo target for two cases of symmetric incoming and outgoing angles. (left column) The spectra and predictions for (ψ, θ) is (20,35) (black) and (15,35) (orange). (right column) The spectra and predictions for (30,45) and (15,45) (black and orange respectively).

is less pre-scattering for larger incidence angles, but it still has a significant impact on the energy distributions, as $\frac{dE}{d\theta}$ is larger for larger angles. Only a slightly smaller scattering angle can therefore result in a notable, apparent increase of the kinetic energy of the scattered particle. For example, a 14 keV Sn particle scattered from Mo over 44° retains 5.38 keV, while it retains only 5.05 keV if scattered over 45° , i.e. a difference of 0.33 keV in energy for only a difference of one degree in angle.

The negligence of pre-scattering in SRIM has a large impact, certainly for grazing incidence angles. For grazing outgoing angles, the way SRIM determines the next point of collision increases the number of collisions and therefore increases the possibility of a deflection into the surface or to large angles outwards. In reality, a scattered particle leaving the target under a grazing angle will experience mainly repulsive interaction resulting in small increases in the total scattering angle and higher ion energies, similar to pre-scattering. Because this is very similar to pre-scattering, energy distributions of symmetric cases of incidence and detection angle combinations, such as in figure 5.14, are also very similar.

The single-scattering peak is more pronounced for smaller incidence angles. Furthermore, one can conclude from our work and is known from previous research [131, 133] that the SRIM simulations show large deviations from experimental data for small, grazing incidence angles, because interaction above the surface is neglected and how SRIM determines the next point of collision. The results from SRIM simulations for ion-surface interaction with small incidence angles should therefore always be treated with care and backed up with experimental data. The problems reported in this section, and the deviation from the experimental results, would be largely mitigated if SRIM would start the simulation of an ion above instead of in the surface.

For larger incidence angles, the predictions of SRIM are in accordance with the experimental results, barring the single scattering peak. This shows that SRIM is quite accurate for the interaction between the projectile and the target atoms inside the sample. The interatomic potentials, the scattering angle determination, and the straggling are simulated well for tin interactions within a molybdenum target, as far as our research extends.

5.4 Conclusions

In modern EUV-sources, based on laser-produced tin plasmas, tin ions are emitted from the plasma and can interact with the surrounding walls and optical elements. The interaction between the tin ions and a surface can be investigated by the use of SRIM, a widely-used simulation package. A thorough experimental investigation of the accuracy of these simulations

for backscattering energy distributions of heavy ions is lacking however. We presented the results of tin backscattering experiments on a molybdenum target, and compared the energy distributions with the predictions of SRIM.

The experimental energy distributions are in agreement with the simulations, except for a significant peak in SRIM which is associated with a single collision in the upper layer of the simulated target. This peak is not visible in any of the examined distributions in the experiments. We excluded the possibility of this being a charge state-specific deviation, or only appearing for a specific projectile ion and/or target surface. TOF measurements, which measures mainly atoms instead of ions, did not significantly differ from the ESA measurements. The single scattering peak in SRIM is probably due to ignoring any interaction above the surface and the determination of the next collision point. This also induces deviations for grazing incidence and outgoing angles. Inclusion of surface interaction by initializing the ion trajectory simulation above the surface will largely mitigate these deviations. The agreement in the case of the multiple collision part of the experimental energy distribution with the simulations shows that the underlying principles of ion-surface interaction inside the surface are well-understood and properly simulated by SRIM. The penetrating trajectories are simulated well by SRIM, but for lower kinetic energies the ions penetrate the target less than for higher energies. For these lower energies surface interactions are more and more relevant, which are not that well-simulated by SRIM. Simulation packages with improved models are necessary to investigate these surface interactions.

Chapter 6

A comparative study of two simulation methods for ion scattering

In chapter 5, we discussed the energy distributions of tin ions scattered from Mo and Ru. We compared experimental distributions with the simulation results of a simulation package called SRIM, showing clear deviations in particular related to single-collision events. In this chapter, we use the results of another simulation package (SDTrimSP) to investigate the accuracy of this package. This gives also more insight in the origin of the deviations visible for SRIM. SDTrimSP gives better agreement with the experimental scattering distributions than SRIM for both a pure Ru target as well as RuO₂, although a single scattering peak persists in smaller form. The TOF distribution measured in chapter 5 can be properly simulated by SDTrimSP by the combined recoil and scattering distribution from a RuO₂ target.

6.1 Introduction

In the previous chapter, we showed the ion energy distributions of tin ion beams (among other ion species) scattered from molybdenum and ruthenium solid targets. The distributions were dominated by multiple collision scattering inside the target. We compared those distributions with the results of simulations performed with a widely-used simulation package called SRIM [98]. In general these simulations are in good agreement with the experimental results, bar a strong single scattering peak visible in the simulations but not in the experiments. We investigated many possibilities as a cause of this discrepancy, and concluded that it is probably inherent to the simulation package, hinting at errors in scattering potentials or the interaction treatment near the surface.

In this chapter, we show the simulation results of SDTrimSP [122]. This program combines the variety of possible input parameters of SRIM with the dynamic target properties of TRIDYN [134], in which the target composition can change during the simulation because of sputtering and implantation. In addition, SDTrimSP enables parallel computation and more control on the output of the simulation, at the expense of user friendliness. A major difference to SRIM is that SDTrimSP starts the trajectory of a particle already above the surface (2.2 Å), instead of on the surface itself as in SRIM, which in chapter 5 was concluded to have a major contribution to the deviations from the experiments. Other differences include a more accurate computation method and flexibility in the choice of interatomic potentials and the scattering angle determination method. SDTrimSP is a binary collision approximation program which uses an amorphous structure as a target sample, similar to SRIM.

We will make a comparison between the results of the SDTrimSP simulations and the experimental distributions. We will also show the similarities and differences with SRIM simulations. Unless otherwise specified, the number of projectile particles simulated is six million for both packages. We define the incidence angle as the angle with respect to the surface plane and the detection angle as the angle with respect to the incoming beam, as we did in the last chapter. SDTrimSP uses the average atomic mass of the target element (101.1 amu for ruthenium) and of the projectile element (118.7 amu for tin). Isotopically pure ^{120}Sn and a Ru isotopic mixture with the appropriate abundance ratio is used in SRIM. The bin

size for all distributions in this chapter is 50 eV. For SDTrimSP only particles which are within 1° of the detection angle are taken into account. For SRIM this 1° limit is also applicable for detection angles up to and including 40° ; above this angle the limit is 2.5° . The lower yield for SRIM for large detection angles necessitates a larger limit to ensure a comparison with SDTrimSP simulations is valid.

6.2 Results

6.2.1 Simulations on pure ruthenium

Figure 6.1 shows for an incidence angle ψ of 15° and three detection angles θ (25° , 35° , and 45°) the ion energy scattering distributions and the corresponding simulations of SRIM and SDTrimSP. The experiments show for all detection angles a broad energy distribution, associated with multiple collisions inside the target. No clear single scattering peak is visible.

The energy distribution simulated by SRIM for θ is 25° shows a very broad single collision scattering peak around 11 keV. As SRIM does not consider above-surface interaction, only quasi-single collision scattering contributes to the peak for this angle (as $\psi > \theta/2$, see section 5.3.6). This results in a very broad and very large peak visible for SRIM at 11 keV (the energy of a single collision scattering peak) as more combinations with small angle collisions are possible. For SDTrimSP, the yield increases drastically around 11.0 keV, indicating that traces of single collision scattering might also be present in the SDTrimSP results. Overall, the SDTrimSP distribution has a very good agreement with the experimental results, except for a lower yield in the low-energy tail below 10.5 keV.

The presumption that the single collision peak is still present in the SDTrimSP calculations is confirmed by the results for a detection angle of 35° . The SDTrimSP simulations show a small peak at 8.5 keV, the energy position of the single collision scattering peak. However, the SDTrimSP simulation deviates from the ESA distribution in both height and width not as much though as the SRIM result does. The broad part of both the SDTrimSP and SRIM distributions, which has its origin in multiple scattering, is in excellent agreement with the experimental results. A

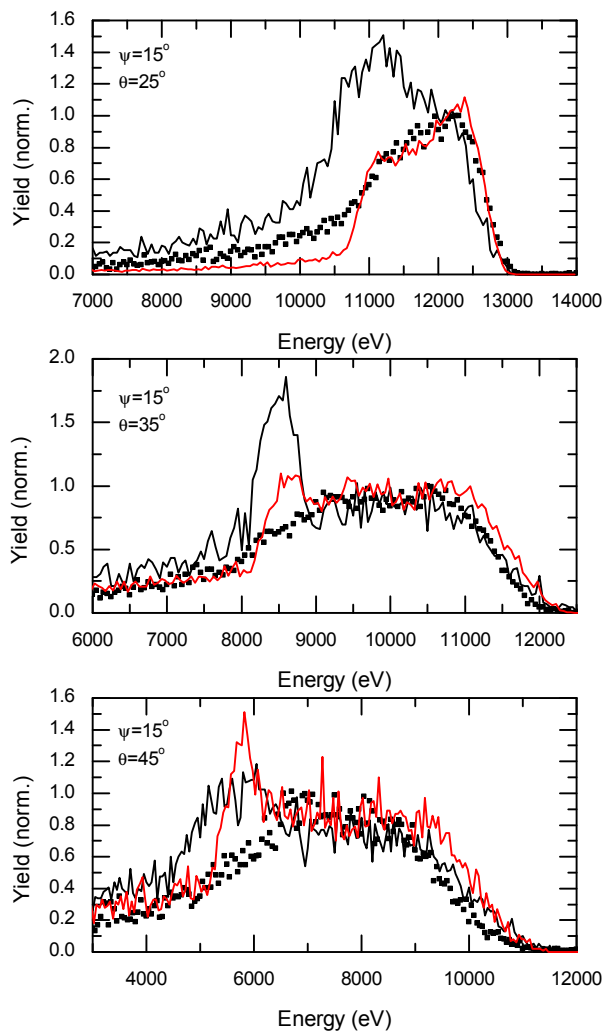


Figure 6.1: Experimental tin ion scattering spectra (black dots), together with corresponding SRIM (black line) and SDTrimSP simulations (red line) for 14 keV Sn^{2+} at ψ is 15° . θ is, from top to bottom, 25° , 35° , and 45° . The simulations are for a pure Ru target.

small deviation is visible in the high-energy tail, where the simulations show a higher yield than measured by the ESA. This stems from the fact that the experiments are conducted with an isotopically pure ion beam of ^{120}Sn , while the SDTrimSP simulations use the average mass of tin (118.7 amu). The tin atoms retain a slightly larger part of the energy in the simulations (in the order of approximately 50 eV), as the mass used in the calculation is slightly lower. Another aspect is that tin particles scattered from implanted tin will also retain a larger energy, as a Sn target atom is heavier than the original ruthenium. This energy shift is in the order of roughly 500 eV, becoming larger for larger detection angles.

For θ is 45° , the SRIM simulations still have a broad single scattering peak around 5.6 keV, but not as strong as at smaller scattering angles. This is expected as the cross section is smaller for larger scattering angles, due to the smaller impact parameter. Remarkably the SDTrimSP simulations show a single collision peak which is slightly higher and more narrow than the one in the SRIM results. This might be due to the SDTrimSP simulations assuming a Ru target with a single, average mass (101.1 amu) instead of a combination of all ruthenium isotopes with the appropriate natural abundance ratio as used by SRIM. For example, a 14 keV tin ion scattering over 45° from the heaviest isotope of ruthenium (103.9 amu) retains 5.9 keV while for the lightest isotope (95.9 amu) it is only 5.0 keV, a difference of no less than 0.9 keV. A mixture of isotopic masses results in a variety of outgoing energies, and therefore a broadening of the single scattering peak. The remainder of the SDTrimSP distribution has a good agreement with the experimental data, similar to SRIM.

The single collision scattering peak, so notable in the SRIM simulations but absent in the experimental distributions, persists for SDTrimSP. However, the peak is less strong, up to the point that the simulations are in good agreement for the distribution of θ is 25° . The single scattering peak is roughly as high for SDTrimSP simulations as it is for SRIM for the largest detection angle, while for smaller detection angles the peak is significantly larger in SRIM simulations. In chapter 5, we mention the negligence of the interaction above the surface by SRIM, both on the incoming and outgoing trajectory, as a possible cause for deviations from the experimental distribution and as a point of concern. SDTrimSP starts the simulation above the surface, and has a significant lower single scattering

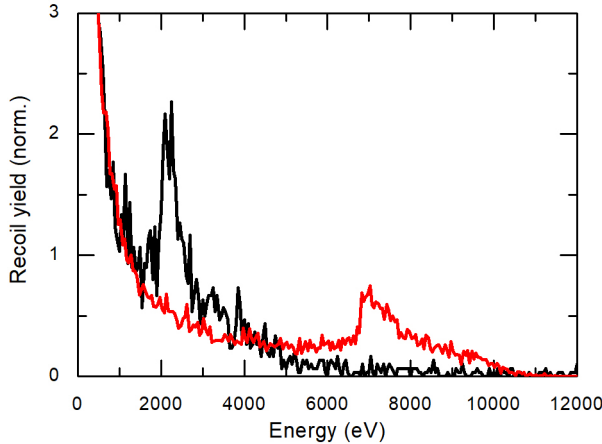


Figure 6.2: SRIM (black) and SDTrimSP (red) energy distributions of sputtered Ru recoils from a pure ruthenium target for a 14 keV Sn ion beam incidence at 15° and a detection angle of 45° .

peak especially for the smaller detection angles, i.e. where the interaction above the surface matters the most. Possibly SDTrimSP could benefit from a starting point at an even larger distance in front of the surface. These results at least confirm the difficulties SRIM has to properly simulate ion-surface interactions with small incoming and outgoing angles. The multiple collision scattering part of the SDTrimSP simulations agrees with the experimental distributions, as it was the case for SRIM.

The ESA energy distributions in the last and in this chapter show sometimes small increases in yield around the primary recoil energy of sputtered particles (cf. equation 4.5). SRIM and SDTrimSP are both capable to calculate sputtering distributions and might be used to predict the sputter yields. In figure 6.2, the energy distributions of sputtered Ru particles of both SDTrimSP and SRIM are shown for (ψ, θ) is $(15, 45)$ for a pure ruthenium target. Five hundred thousand particles are simulated for the SRIM simulation, resulting in roughly 14 million sputtered Ru recoils over all angles. This implies high sputter yields on the order of 30 Ru particles per incoming 14 keV Sn ion. SDTrimSP predicts a sputter yield of 15 particles per incoming ion, approximately half of SRIM. Contrary to

our findings, Hofsäss et al. [117] report higher sputter yields for SDTrimSP if the projectile mass is larger than the target mass, albeit with lower ion kinetic energies of 1 and 5 keV and a normal incidence angle. They find, for example, 50% higher sputter yields for 1 keV xenon on molybdenum, and 28% higher yields for 5 keV. The downward trend for higher projectile energies does not contradict our result that SRIM has a higher yield for 14 keV ions.

Striking differences are visible in the recoil energy distributions. For the SDTrimSP simulations, a clear distinct peak is visible at 6.9 keV, together with many sputtered particles with low kinetic energies. Those low-energy sputtered particles are also visible in SRIM, but the peak at 6.9 keV is not. Instead of this peak, a peak just above 2 keV is apparent. The distinct peak in the SDTrimSP simulations corresponds to the primary recoil energy of Ru sputtered over 45° , 7 keV. The peak showing up at 2 keV in the SRIM calculations can not be attributed to a single collision event.

It is clear that SRIM does not predict a peak where it is expected, at the primary recoil energy. Instead it produces an unattributed peak at lower energies. In literature, it is reported that SRIM has problems with the appropriate sputtering yield and the angular distribution of sputtered particles [118, 125], which are better simulated by SDTrimSP and other simulation packages [117]. In addition of these deviations, our work shows that SRIM also has large uncertainties in the energy distributions of energetic sputtered particles.

Primary oxygen recoils are not visible in these ESA spectra due to the reionization probability, but they do show up together with traces of carbon in the TOF spectra. Oxygen is continuously attached to the surface in the experiments due to the ambient pressure. The single collision scattering peak showing up prominently in the simulations might become less or even diminish if absorbed oxygen layers are included in the simulations, by e.g. using RuO_2 as a target instead of ruthenium. In the next section we compare the simulations for an oxidized target to the ion scattering distributions. A small increase of the yield is found at the primary recoil energies of ruthenium and molybdenum in the ESA energy distributions. The ionization fraction of the oxygen recoils is apparently significantly lower than for tin and ruthenium, compromising a direct comparison of

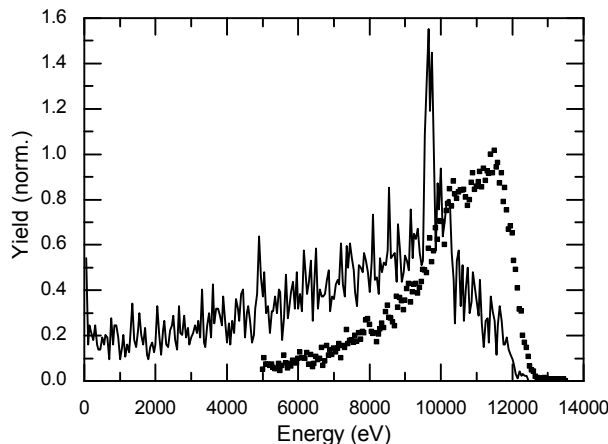


Figure 6.3: The SRIM backscattering simulation for a RuO_2 target (line) and the experimental energy distribution (dots) of a 14 keV Sn^{2+} ion beam incidence at 15° and a detection angle of 30° .

ESA results with sputtering simulations. It is feasible to include recoils in a comparison with TOF measurements (see section 6.2.3).

6.2.2 Comparison to simulations on RuO_2

In figure 6.3, the results of an ESA measurement is compared with SRIM backscattering simulations on a RuO_2 target for (ψ, θ) is $(15, 30)$. As mass for ruthenium the mean mass of 101.1 is used instead of the usual isotopic mixture. The overall comparison to the experimental data is worse than for SRIM simulations using a pure Ru target. The single collision scattering peak, theoretically located at 9.8 keV, is still visible. The peak is located just below this ion energy and is relatively sharp. The broad part of the scattering energy distribution is now very different from the experimental results, it is shifted towards much lower energies. It does predict almost no yield between 10 and 12 keV, the energy range where the yield is at its maximum in the experiments. The scattering from an oxide-compound target is not accurately simulated by SRIM. The energy loss of relatively heavy tin particles on the light O atoms seems to be overestimated by SRIM.

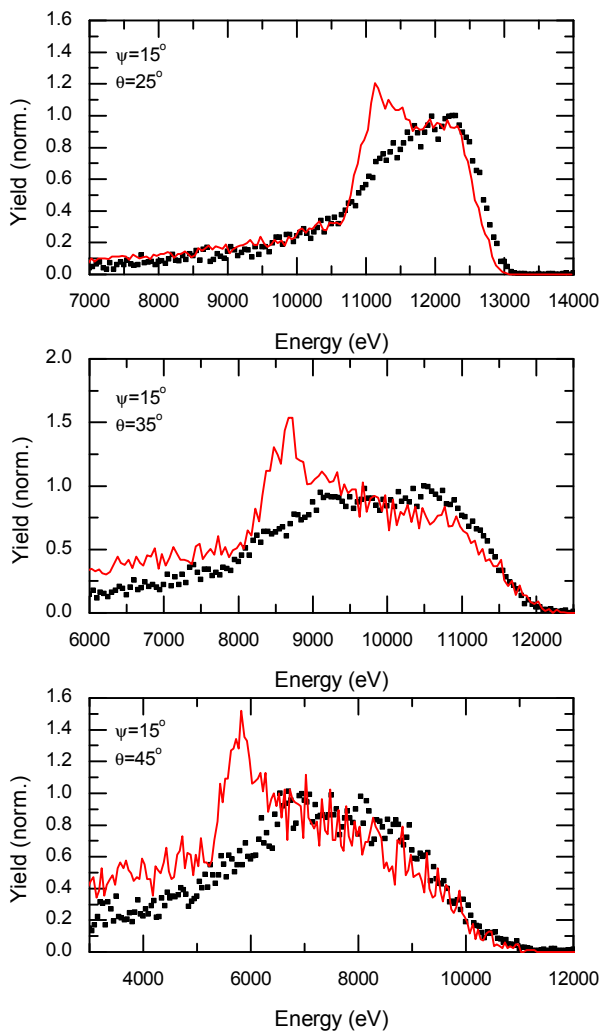


Figure 6.4: The ion scattering spectra (black dots) and the SDTrimSP simulations (red line) for 14 keV Sn^{2+} at ψ is 15° and θ is from top to bottom 25° , 35° , and 45° . The simulations are for a RuO_2 target.

In figure 6.4, the same ESA distributions as in figure 6.1 are shown, but now with the corresponding SDTrimSP simulations for a RuO_2 target

instead of pure Ru. There is no obvious shift towards lower energies, as observed in the SRIM energy distributions. For ψ is 15° and θ is 25° , the broad distribution shows excellent agreement with the measurements, but once again a peak is visible in the synthetic spectra around 11 keV, the energy corresponding to the single collision scattering peak of tin scattering from ruthenium. The low-energy tail has an excellent agreement with the experimental results. In the high-energy tail the yield seems to be slightly shifted towards lower energies for an ion energy above 12 keV.

For θ is 35° , the simulation exceeds the low-energy tail of the experimental data. Between 10 and 11.5 keV the simulations underestimate the ion yield. The single scattering peak at 8.5 keV stands out. The distributions at θ is 45° give a similar view as for 35° . The yield in the low-energy tail is higher while lower for energies between 7 and 9.5 keV. The single scattering peak around 5.8 keV remains prominent.

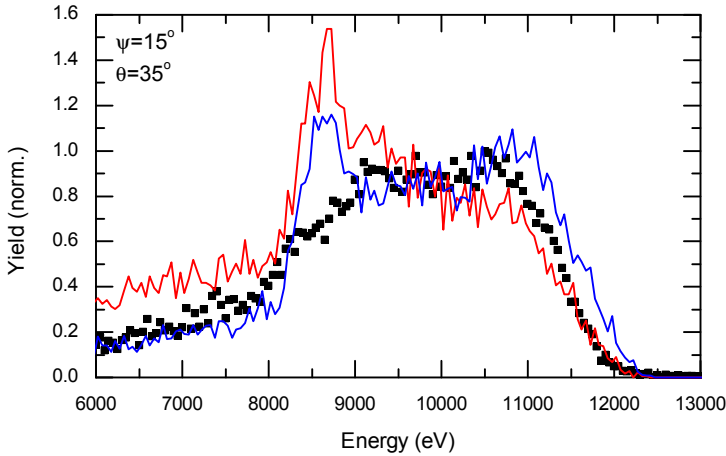


Figure 6.5: An ion scattering spectrum (black dots) and the SDTrimSP simulations for a pure Ru target (blue line) and a RuO_2 target (red line) for 14 keV Sn^{2+} at ψ is 15° and θ is 35° .

Although the simulations for the RuO_2 target are in reasonable agreement with the experiments, the single scattering is still strongly present. Furthermore the yield for higher energies is suppressed, while it is higher in the low-energy tail. The simulations for a pure ruthenium target agree

better with the experiments than those for RuO₂ (see, for example, figure 6.5). In the simulations, the oxygen in the target reduces the energy of the scattered tin ions too much and reduces the yield for multiple collision scattering which results in relatively more single collision scattering. Using only a small number of monolayers of RuO₂ on a pure Ru target in the simulations can possibly be a solution.

The agreement with the experiments is bad for SRIM when using an oxidized target, and can be improved for SDTrimSP by using a different target composition. Even if the ESA distribution can not be simulated perfectly using an oxidized target, oxygen is present on the target surface. The ion yield depends heavily on the specific ionization degree for each species, complicating direct comparisons of the data with simulations of both backscattered tin and sputtered ruthenium. We use TOF measurements in the next section, and compare these with the oxygen, tin, and ruthenium distributions calculated for RuO₂ by SDTrimSP. As we measure both neutrals and charged particles alike, the ionization fraction does not play a role.

6.2.3 Comparison to TOF measurements

In figure 6.6, the TOF distribution for a 14 keV Sn²⁺ ion beam incidence at 15° and measured at 40° is shown, together with the scattering and recoil distributions obtained by SDTrimSP. The location of the short-TOF peak at 3.5 μs corresponds to the energy of the oxygen recoils and is properly simulated by SDTrimSP, but is larger in the experimental distribution.

For longer flight times, the simulations expect a higher oxygen recoil yield than measured in the experiments. This low-energy oxygen recoil tail extends far into the Sn scattering and ruthenium recoil peak, but appears not to be visible in the experiments. This can be explained by considering the detection efficiency of a channeltron which decreases strongly from a value of 0.9 at 3.4 keV to just 0.3 at 0.85 keV [135]. This kinetic energy corresponds with a flight time of 7 μs. Therefore the contribution of O to the main feature (5-10 μs) is neglected in the comparison. We do show the summed spectrum of the Ru recoil and Sn scatter peak, and their individual contributions. The detection efficiency of tin, and presumably also ruthenium as it has a similar mass, decreases in the shown energy range from 0.8 at its maximum to an appreciable 0.7 (cf. section 4.4.3).

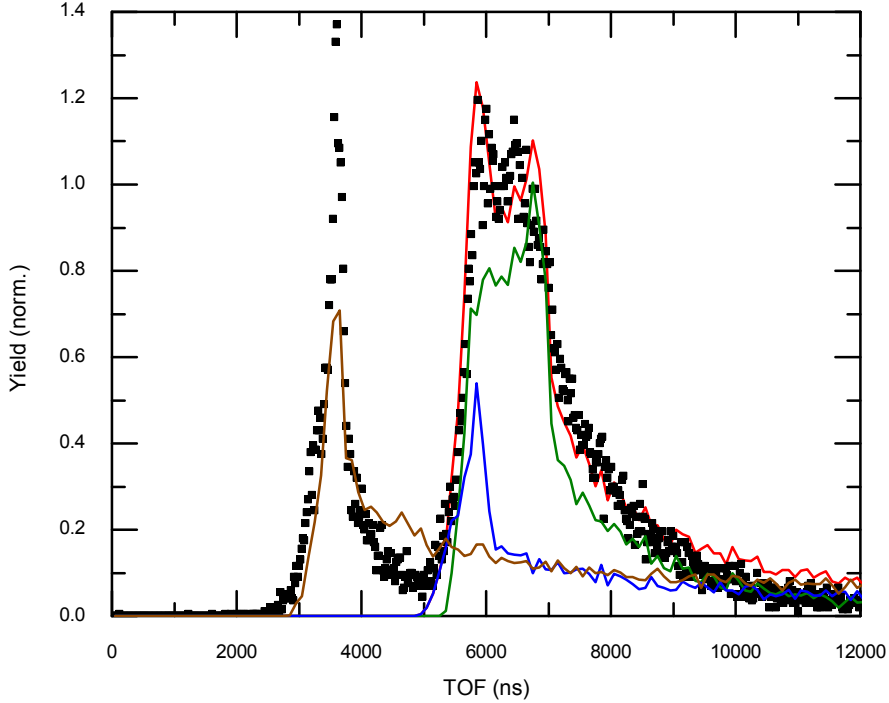


Figure 6.6: The measured TOF distributions (black dots) and the SDTrimSP simulations (lines) for 14 keV Sn^{2+} at ψ is 15° and θ is 40° . The simulations are for a RuO_2 target. The dark green line is the simulation of the backscattered tin particles, the blue line the sputtered ruthenium atoms, and the brown the sputtered oxygen particles. The red line is the sum of the backscattered Sn and the sputtered Ru results.

Between 5 and 8 μs a large peak is apparent in the experimental distribution, and is also predicted by the simulations. For flight times above 8 μs the simulation exceeds the experiments. This peak seems to have a double-peak structure, with a peak at 6.0 μs and at 6.5 μs . This corresponds reasonably well with the primary ruthenium recoil peak at 5.8 μs and the peak of the scattering distribution at 6.8 μs predicted by the SDTrimSP calculations.

There is good agreement between the TOF measurements and the combined Sn scattering and Ru recoil spectrum of SDTrimSP, and also the primary recoil peak of oxygen is properly simulated. The overlap of the maximum of the tin scattering distribution and the primary recoil energy of ruthenium for this particular detection angle is strong. Two TOF tubes at different angles will be attached to the setup. This will provide a larger difference in TOF, as the final energy of a sputtered particle depends on the angle in a different way than a scattered ion. With this larger TOF difference, the individual contribution to the total spectrum by the scattering and the recoil distribution can be assessed better. With the new TOF tubes the SDTrimSP simulations of the sputtered and scattered spectrum can be investigated in more detail.

6.3 Conclusions

We compared the results of three ion energy distributions taken at different detection angles and a TOF distribution with the results of two simulation packages, SRIM and SDTrimSP. For a pure Ru target SDTrimSP has a much better agreement with the experimental results than SRIM, especially for smaller total scattering angles. The simulations can be further improved by using the appropriate isotopic mixture of ruthenium instead of the average mass. Comparison of the experiments to the simulations with an oxidized Ru target are not feasible for SRIM, as the backscattering distribution has a strong shift towards low-energy ions and the sputtered particles are not simulated well, indicating that the package has difficulties in simulating the interaction between a heavy and a light atom. In SDTrimSP, the simulations for RuO₂ target are in fair agreement with the experimental results but not as good as for taking a pure ruthenium target. A target which consists of several monolayers RuO₂ on top of pure Ru in the simulations can possibly improve the agreement. For the comparison with the TOF measurements we included sputtered ruthenium; these simulations agree with the experiments. The recoil and the scattering peak are close to each other and do overlap. For further investigation of the sputtering and scattering simulations by SDTrimSP it would be an advantage to have a larger flight time difference between those peaks.

Chapter 7

Summary & Outlook

In modern nanolithography machines, extreme ultraviolet (EUV) light from a laser-produced plasma (LPP) is used. This plasma is realized by first irradiating mass-limited tin droplets with a low-intensity nanosecond laser pulse deforming the droplet, in order to increase the laser absorption of an intense main pulse creating the EUV emitting LPP plasma. Tin ions with charge states between 8+ and 14+ have a serendipitous overlap of transitions at 13.5 nm, enabling an EUV light source with this wavelength. The plasma is not contained and emits therefore tin ions and atoms which interact with the source environment, including the optical elements used to transport the EUV light. The ion energy distributions can be 'tuned' by the laser parameters in such a way that less energetic ions are created, and by using 'stopping' methods such as embedding the LPP in a background gas in order to decelerate the ejected ions. In order to tune the laser parameters, it is necessary to get the best possible understanding of the fundamental physics behind the laser absorption of the target and the expansion mechanisms of the plasma (chapters 2 and 3). In order to find the optimal amount of background gas, it is necessary to get a better understanding of the tolerances of plasma-facing materials to ion-surface interactions driven by relatively heavy tin ions (chapters 5 and 6).

In chapter 2, we describe the results of laser-surface interaction experiments. We developed an experimental setup where we irradiated a solid tin target with a pulsed 800-nanometer-wavelength laser, in order to investigate the possibility of using a pre-pulse with a shorter pulse length. In a fluence range spanning 0.9 to 22 J/cm² and a pulse length range from 500 fs to 4.5 ps, we measured at several angles with Faraday cups the yields and time-of-flight distributions of the tin ions. The ablation depth and volume could be obtained employing a high-numerical-aperture optical microscope. We found an increasing ion yield for an increasing pulse length, while the ablation depth decreases and the ablation volume stayed constant. This is attributed to the fact that the laser pulse ionizes the expanding vapor in front of the surface, instead of ablating the target. The ablation depth follows a two-component logarithmic dependence on the pulse fluence, which is in agreement with the available literature. For lower fluences the angular distribution is sharply peaked along the target normal, but this distribution broadens rapidly for increasing pulse fluence. We estimate the ionization degree to be 5-6% at the maximum

fluence investigated, which is substantially lower than the typical ionization fractions obtained for nanosecond-pulsed ablation of metals.

In chapter 3, we look in more detail into the plasma expansion mechanism of a laser-produced plasma. We have measured the ion energy distributions of tin droplets exposed to infrared picosecond laser pulses, and a solid target irradiated by nanosecond pulses in a fluence range up to 4 kJ/cm^2 . These distributions, and the distributions from chapter 2, are compared to two self-similar solutions of a hydrodynamic approach assuming isothermal expansion of the plasma into the vacuum. For laser pulses below 100 ps, the distributions are in agreement with the self-similar solution of a semi-infinite simple planar plasma configuration with an exponential density profile, for both planar as droplet targets. For a solid Sn target exposed to nanosecond-pulses, the results agree with the solutions of a limited-mass model that assumes a Gaussian-shaped initial density profile.

The study of keV ions interacting with surfaces requires large-scale equipment, equipment commissioned at the ZERNIKELEIF facility at the Zernike Institute for Advanced Materials (University of Groningen). The experimental setup for tin ion-surface interactions and its auxiliary equipment is introduced in chapter 4. The interaction of tin ions with solid targets is investigated by measuring in a pioneering experimental campaign the kinetic energy distributions of tin ions backscattered from a molybdenum target, of which the results are presented in chapter 5. The energy distributions are very broad and indicate that the interaction is dominated by multiple collision scattering inside the top layers of the sample. The interaction between projectile particles and solid targets is often addressed with simulations by a computer package called SRIM. We compared synthetic SRIM-based backscattering distributions with the experimental results. The simulations reproduce the broad distributions of the experiments, but on top of it show an additional distinct peak located at the energy corresponding with a single Sn-Mo scattering event. This single-scattering peak is absent in the experiments. This is very remarkable, as it is the simplest, most basic type of scattering. To figure out why single-scattering events appear to be missing we performed a large series of experimental tests. Based on these tests it is concluded that it is not just occurring for tin ions or molybdenum targets, nor is it due to the

electronic structure or the charge state of the projectile ions. With TOF measurements we showed that the energy distribution of backscattered tin neutrals is very similar to the distribution of tin ions. The deviation between experiment and simulation is likely SRIM-related. The interaction inside the target is simulated well, but the interaction at the topmost surface layers is likely less accurate. As ions with lower kinetic energies penetrate the target less deeply, surface interactions, including interactions in front of the surface which are not considered by SRIM, become more relevant and even more elaborate simulation methods are called for.

In chapter 6 we compare the results of such an extended simulation package, SDTrimSP, with SRIM results and with the experimental distributions of tin ions backscattered from a ruthenium target. The SDTrimSP simulations on a pure Ru target correspond overall better with the experimental data than the SRIM simulations, although a smaller peak is still visible at the energy of single collision scattering events. The SDTrimSP single scattering peak is roughly as high as for SRIM only for the largest detection angles, but is significantly smaller for smaller detection angles, while keeping the incidence angle constant. This indicates the problems SRIM has with smaller incidence and detection angles. As the target is not extensively cleaned it is likely to be oxidized on the surface. Therefore we also simulated the backscattering distributions for a pure RuO₂ target. These simulations were done for SDTrimSP only, as SRIM could not provide reliable results for this compound target. Although the RuO₂ simulations have a fair agreement with the experimental distributions, they do not describe the experiments better than when using a pure Ru target. The SDTrimSP simulations with an oxidized target do reproduce the O recoil distribution showing up in our TOF experiments. The combined spectrum of the calculated TOF spectra of Ru recoils and scattered Sn ions is a good agreement with the TOF measurements. SDTrimSP provides definitely better simulations of the low-energy surface interactions in heavy particles colliding on a heavy target, and can also be used to study the interaction with oxidized surfaces.

7.1 Outlook & future experiments

In chapter 6, SDTrimSP shows promising results as compared to SRIM, especially for oxidized surfaces. The TOF measurements could be explained by the combined Sn backscattering and Ru recoil spectrum. It would be beneficial to measure at different detection angles and incidence energies and angles. For different detection angles, the larger TOF separation between the recoil and backscattering peaks makes it easier to distinguish them from each other. Another possibility is to use a different combination of ion species and target sample with a similar ratio of atomic masses, such as krypton on copper. The energies associated with the primary recoil and backscattering ions are very similar due to the same mass ratio, but the TOF peaks are easier to distinguish as these depend on ion velocity instead of energy. It is also interesting to see if and when the single collision scattering peak appears for lighter ion-target combinations.

An open question from the tin backscattering studies is the energy distribution for tin beams with lower kinetic energies. For lower energies, the penetration of the target by the ions is very shallow. Therefore, interaction in the upper surface layers is more important, and the accuracy of simulation packages can be profoundly tested in an energy regime of great relevance to plasma-wall interactions. Such experiments with Sn ion beams are challenging as the detection efficiency of slow Sn ions is very low. Possibly low-energy scattering can first be investigated with krypton or xenon beams, which are relatively heavy so comparable with tin but for which it is easier to obtain high-current beams.

Another uncharted territory is the specific role of the electronic structure of the tin. In figure 7.1, the preliminary results of electron measurements from tin ion beams are shown. For two different charge states of tin, 2+ and 5+, the emitted electrons are measured and compared. The ion beams are decelerated to 1 keV from 14 and 35 keV for respectively 2+ and 5+. A small bias voltage of -9V is used to obtain a better electron yield. The yields are normalized at the highest point in the spectra around 1 eV. The spectra are dominated by low-energy electrons for both charge states, but a higher yield of higher energy electrons is visible for 5+. Sn²⁺ has a closed shell configuration in the ground state, while Sn⁵⁺ has an open hole in the 4d shell. This difference in electronic structure, together with the higher ionization energies for higher charge states, give rise to other,

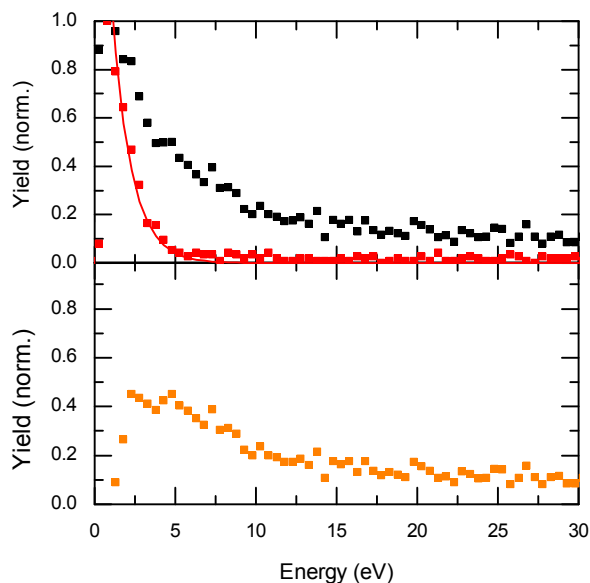


Figure 7.1: (top) The results of electron measurements of a 1 keV Sn^{2+} (red dots) and Sn^{5+} (black) ion beam, with a target angle of 15° and detection angle of 105° . The target is biased at -9V , for which is corrected in the electron energy. Also shown is a fit of the exponential decay of the Sn^{2+} results (red line). (bottom) The residual of the Sn^{5+} results minus the fit of the Sn^{2+} results.

more energetic electrons to be emitted from hollow tin atoms produced by the resonant neutralization of the Sn^{5+} ions. Also shown in figure 7.1 is the residual of the 5+ results of which the 2+ results are subtracted. This shows the electrons for which the higher charge state enables their emission. This difference spectrum shows hints of two peaks, at 2.5 and 5 eV, indicating specific electronic transitions which could be interesting to investigate further to assess how much potential energy hollow atoms may deliver to the surface in addition to their kinetic energy.

Chapter 8

Samenvatting

In hedendaagse nanolithografiemachines wordt extreem ultraviolet licht (EUV) gebruikt dat ontstaat in een laser-geproduceerd plasma (LPP). Dit plasma wordt gemaakt door eerst tindruppels te beschijnen met laag-intensieve, nanoseconde-lange laserpulsen (voorpulsen). De voorpuls vervormt de druppel en verhoogt de laserabsorptie van een zeer intense hoofdpuls, die het EUV-uitzendende plasma vervolgens vormt. Tinionen met een ladingstoestand tussen de 8+ en 14+ hebben een zeer fortuinelijke overlap van verschillende overgangen nabij 13.5 nm, wat een EUV-bron bij deze golflengte mogelijk maakt. Het plasma wordt niet opgesloten door sterke magneetvelden en zendt daardoor tinionen en -atomen uit die een wisselwerking hebben met de omgeving, inclusief de optische elementen die worden gebruikt om het geproduceerde EUV-licht verder te sturen. De energieverdelingen van de ionen kunnen worden gestuurd met de laserparameters, waardoor bijvoorbeeld minder energetische ionen ontstaan. Door middel van 'stopping'-methodes, zoals het inkapselen van het LPP met een achtergrondgas, kunnen de vrijgekomen ionen worden vertraagd. Om de laserparameters te kunnen tunen is een zo goed mogelijk begrip nodig van de fundamentele natuurkunde die ten grondslag ligt aan de laserabsorptie en de expansiemechanismes van het plasma (hoofdstukken 2 en 3). Om de optimale hoeveelheid achtergrondgas te vinden is het nodig om een beter begrip te krijgen van de consequenties van interacties tussen relatief zware ionen en oppervlakken voor aan plasma blootstaande materialen (hoofdstukken 5 en 6).

In hoofdstuk 2 worden de resultaten van experimenten besproken die de interactie tussen laserlicht en oppervlakken onderzoeken. Met deze serie experimenten onderzoeken wij de mogelijkheid om kortere laserpulsen te gebruiken als voorpuls. We hebben een experimentele opstelling opgebouwd waarmee een vast tinmonster wordt beschoten met laserpulsen, die een golflengte hebben van 800 nm. In een fluentiebereik van 0.9 tot 22 J/cm² en voor een laserpulsduur van 500 fs tot 4.5 ps maten wij onder verschillende hoeken de opbrengst en vluchttijd distributies van tinionen. De ablatiediepte en het ablatievolume kon naderhand worden bepaald met een optische microscoop met een hoge numerieke apertuur. Wij vonden een toenemende ionenopbrengst voor langere pulsen, terwijl de ablatiediepte afnam en het volume gelijk bleef. Dit schrijven wij toe aan het feit dat de laserpuls de expanderende tindampen voor het oppervlak ioniseert

in plaats van dat het leidt tot ablatie van het monster. De ablatiediepte heeft een tweevoudige logaritmische afhankelijkheid van de pulsfluentie, wat overeenkomt met de beschikbare literatuur. De hoekdistributie van de ionen is voor lage fluenties een haarscherpe piek loodrecht op het oppervlak, maar deze wordt snel breder als de fluentie toeneemt. De ionisatiegraad is een geschatte 5 à 6 % voor de hoogste fluentie die wij hebben onderzocht, wat aanzienlijk lager is dan de ionisatiegraden die normaliter horen bij ablatie van metalen door middel van nanoseconde-lange pulsen.

In hoofdstuk 3 richtten wij de ogen op de expansiemechanismen van een lasergeproduceerd plasma. Wij maten de ionenergiedistributies van tindruppels die zijn blootgesteld aan infrarode, picoseconde-lange laserpulsen en van vaste stoffen die zijn beschenen met nanosecondepulsen voor fluenties reikende tot 4 kJ/cm^2 . Deze verdelingen, en die van hoofdstuk 2, worden vergeleken met twee relatief simpele modellen voor de expansie van een plasma (beide zijn zelfgelijkvormige oplossingen van een hydrodynamische aanpak die veronderstelt dat het plasma isothermaal expandeert in het vacuüm). Voor laserpulsen korter dan 100 ps komen de distributies, voor zowel vlakken als druppels, overeen met het meest elementaire model (de zelfgelijkvormige oplossing van een semi-oneindige, simpele planaire plasmaconfiguratie met een exponentieel dichtheidsprofiel). Om de resultaten te begrijpen voor een vast tinmonster blootgesteld aan nanoseconde-pulsen was een uitbreiding van het eerste model nodig: dit zijn de oplossingen van een massa-gelimiteerd model dat initieel een Gaussisch dichtheidsprofiel veronderstelt.

Bestudering van de wisselwerking tussen ionen met keV-grote energiën en oppervlakken vereist grootschalige apparatuur, apparatuur die is opgebouwd in de ZERNIKELEIF-faciliteit behorende bij het Zernike Institute for Advanced Materials van de Rijksuniversiteit Groningen. De opstelling voor tinionen-oppervlakkenexperimenten en de bijbehorende randapparatuur wordt beschreven in hoofdstuk 4. De interactie van tinionen met vaste stoffen is onderzocht in een uitgebreide meetcampagne door de kinetische-energiedistributies te meten van tinionen die worden verstrooid door een molybdeenstaal. De resultaten hiervan zijn te vinden in hoofdstuk 5. De energieverdelingen zijn zeer breed, wat er op wijst dat de interactie wordt gedomineerd door verstrooiing via meerdere botsingen in de bovenste lagen van het oppervlak. De wisselwerking tussen atomaire deeltjes

en vaste stoffen wordt vaak bestudeerd met simulaties van het computerprogramma SRIM. Wij hebben de kunstmatige, op SRIM-gebaseerde verstrooiingsverdelingen vergeleken met de experimentele resultaten. De simulaties reproduceren de brede verdeling zichtbaar in de experimenten, maar zien daar bovenop een zeer kenmerkende piek voor een energie die overeenkomt met de verstrooiing van Sn door Mo in een enkele botsing. Deze enkelvoudige-verstrooiingspiek is niet aanwezig in de experimenten, wat zeer opmerkelijk is aangezien dit de simpelste en meest elementaire vorm van verstrooiing is. Om uit te zoeken waarom deze piek mist hebben wij een serie experimentele proeven uitgevoerd. Hieruit concluderen wij dat de enkelvoudige-verstrooiingspiek niet alleen absent is voor tinionen of molybdeenoppervlakken, noch dat het te wijten is aan de elektronenstructuur of de ladingstoestand van de inkomende ionen. Met vluchttijdmetingen hebben wij aangetoond dat de energieverdeling van verstrooid, niet-geladen tin zeer vergelijkbaar is met die van tinionen. Zeer waarschijnlijk ligt de oorsprong van de verschillen tussen experiment en simulatie in SRIM. Binnenin het oppervlak is de interactie wel goed gesimuleerd door SRIM, maar in de bovenste laag is het minder nauwkeurig. Omdat ionen met minder energie het proefmonster minder ver binnendringen, wordt de interactie met de toplaag en de interactie plaatsvindend vóór penetratie van het oppervlak - wat niet meegenomen wordt door SRIM - steeds relevanter. Voor deze interacties zijn meer uitgebreide simulatiemethodes vereist.

In hoofdstuk 6 vergelijken wij de berekeningen van een dergelijk pakket, SDTrimSP, met die van SRIM en met de experimentele distributies van tinionen verstrooid aan een rutheniumstaal. De SDTrimSP-simulaties voor een puur Ru-oppervlak komen over het algemeen veel beter overeen met de experimentele data dan de SRIM-simulaties, alhoewel een kleinere piek nog steeds zichtbaar is bij de energie van een enkelvoudige botsing. Deze piek is voor SDTrimSP ongeveer net zo hoog als voor SRIM bij de grootste detectiehoeken, maar wordt aanmerkelijk kleiner bij kleinere hoeken voor dezelfde invalshoek. Dit toont de problemen aan die SRIM heeft met het simuleren van kleinere inval- en detectiehoeken. Omdat het monster niet wordt schoongemaakt bij preparatie is het waarschijnlijk licht geoxideerd. Daarom hebben wij ook de verstrooiingsverdelingen gesimuleerd voor een volledig RuO₂-oppervlak. Omdat SRIM hiervoor geen

betrouwbare resultaten kon produceren, zijn deze simulaties alleen uitgevoerd met SDTrimSP. Alhoewel ze redelijk goed overeenkomen, is het niet een duidelijk betere beschrijving van de experimentele resultaten dan de simulaties voor puur ruthenium. De SDTrimSP-berekeningen met een geoxideerd oppervlak reproduceren het verstoven zuurstof wat zichtbaar is in onze vluchttijdmetingen. Het gecombineerde spectrum van de vluchttijdberekeningen voor ruthenaflagen samen met dat van verstrooide tindeeltjes heeft een goede en veelbelovende overeenkomst met onze gemeten vluchttijdverdeling. SDTrimSP levert duidelijk betere simulaties af voor laag-energetische oppervlakprocessen die plaatsvinden bij botsingen tussen zware deeltjes met een qua atoommassa vergelijkbaar monster. Ook is het geschikt voor bestudering van interactie met geoxideerde oppervlakken.

Appendix A

ESA power supplies

The voltages on the inner and outer plates of the ESA are provided by two Applied Kilovolts high voltage power supplies (HVPS) of type HP 2.5R. These power supplies are polarity reversible and can deliver a voltage in the range of 10-2500V. At full load the voltage ripple is less than 20 mV_{p-p} , and is further reduced by a 0.1F capacitor parallel to the output voltage. An input voltage of 0-10 V directs the output voltage of the HVPS, which amplifies the input voltage by a factor of 250 and sets the polarity ($0 - 10V \cong \pm 10 - 2500V$). A programmable gain amplifier (PGA), used to enhance the resolution, provides this input voltage. The PGA amplifies a 0-1V signal by a certain, programmable gain factor (1, 2, 5, or 10). The voltage from the HVPS is sent to one of the two plates of the ESA. The same voltage is also reduced with a factor of 25 multiplied with the PGA factor. This reduced voltage is therefore in the range of -10-10V and can be used to monitor the output voltage. A schematic overview can be found in figure A.1.

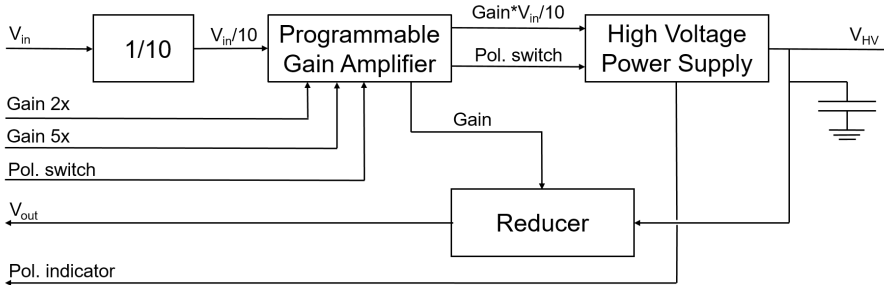


Figure A.1: A schematic representation of the power supplies for the plates of the ESA. An analog input voltage and three digital signals for the gain and polarity determine the voltage for the ESA plates.

The system of PGA, HVPS, and reducer is controlled by a Measurement Computing DAQ-device of the type USB-2408-2AO. The DAQ-device has two 16-bit analog output channels in the range of -10 - 10V. A 0-10V signal is reduced by a factor of 10 before it is used as an input voltage for the PGA. Two 24-bit analog input channels of the DAQ-device with a range of -10-10V read the (reduced) output voltages of both power supplies. The measurement control program (see appendix B) uses these voltages to check and, if necessary, readjust the voltage of the HVPS. Two

digital output channels (per HVPS unit, so four in total) control the gain factor of the PGA. One of the two changes the gain with a factor of 2 when a 5V-signal is applied, the other with a factor of 5. The combination gives four possible gain factors: 1, 2, 5, and 10. A third digital output channel controls the polarity of the HVPS: 0V will result in a negative output voltage, 5V in a positive voltage. A digital input channel can be used to check the polarity. A 5V signal on this channel indicates a negative output voltage of the HVPS, remarkably the opposite of the signal on the output channel.

<i>Channel DAQ</i>	<i>Connector</i>	<i>Wire color(s)</i>	<i>Purpose</i>
AI0 1	U1 ADC	white	Reads Voltage U1
Agnd 3	U1 ADC	brown	Ground
AI1 4	U2 ADC	white	Reads Voltage U2
Agnd 6	U2 ADC	brown	Ground
Dgnd 13	U1 PBIO	brown	Ground
DIO0 14	U1 PBIO	yellow	Sets Gain(2x) U1
DIO1 15	U1 PBIO	yellow-brown	Sets Gain(5x) U1
DIO2 16	U1 PBIO	yellow-white	Sets Pol U1
DIO3 17	U1 PBIO	grey	Polarity indicator U1
DIO4 18	U2 PBIO	grey	Polarity indicator U2
DIO5 19	U2 PBIO	yellow-white	Sets Pol U2
DIO6 20	U2 PBIO	yellow-brown	Sets Gain(5x) U2
DIO7 21	U2 PBIO	yellow	Sets Gain(2x) U2
Dgnd 22	U2 PBIO	brown	Ground
Agnd 35	U2 DAC	yellow & green	Ground
AO1 36	U2 DAC	white & brown	Sets Voltage U2
Agnd 37	U1 DAC	yellow & green	Ground
AO0 38	U1 DAC	white & brown	Sets Voltage U1

Table A.1: A table of the connections between the new DAQ-device and the old connectors of the power supplies.

Originally, the system of HVPS, PGA, and reducer was connected to a set of controllers which used a BITBUS communication protocol to communicate with the control computer. This set of controllers was replaced by the DAQ-device, but still some redundant connections and controllers

are in place. An overview of all the relevant connections between the power supplies and the DAQ-device is given in table A.1.

Appendix B

Labview control program

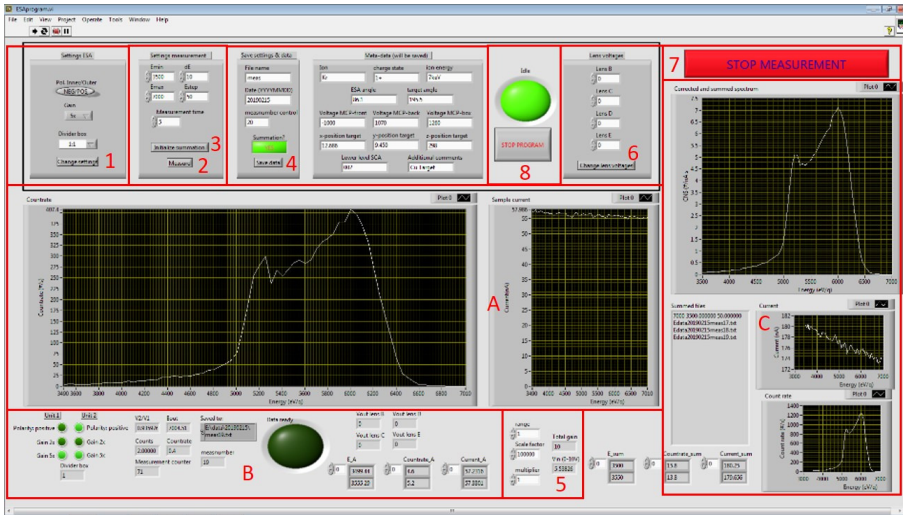


Figure B.1: The main screen of the control program. Visible are the eight action blocks (labeled 1-8) and the three data output blocks (A-C), which are explained in more detail in the main text.

The replacement of the BITBUS communication protocol with connections to the DAQ-device (see appendix A) and the new measurement & control computer necessitated a new home-made Labview control program. This program is inspired by the old one but is suitable for the new communication system and has new features, such as controlling the deceleration lenses and automatic recording of the measurement parameters. In this appendix the program is described on basis of its eight action and the three output blocks (see figure B.1). First the working principle of the action selection is explained, and an example of one of the action blocks is used to show what a typical block consists of. Then an overview of the remainder of the program is given.

Five of the eight actions are activated by pressing a button which will initiate a certain *case* (5, 7, and 8 work differently), of which an example (setting the deceleration lenses, labeled as button 6 in figure B.1) is shown in figure B.2. The program consists of a continuous while-loop, of which the stop condition is the activation of the *stop program*-button (action 8). In this while-loop, a shift register will keep track of the case number which

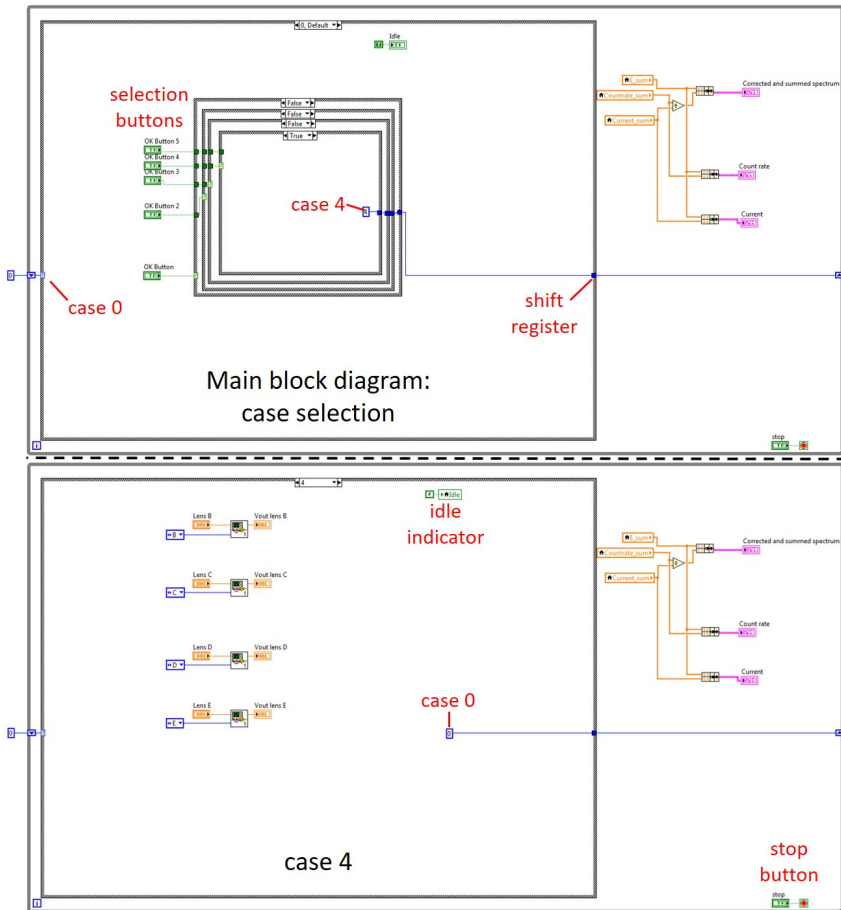


Figure B.2: (top) Part of the program where a case is selected (in this example case 4) by one of the main screen buttons. (bottom) Example of one the cases (case 4, which sets the deceleration lenses). After execution of the case, case 0 (case selection) is loaded again.

has to be selected in the next iteration of the loop. At first, the default case 0 is loaded, in which the next case number is selected by pressing one of the action buttons. If one of these is pressed, the case number corresponding to that action button is loaded into the shift register and will be executed in the next iteration of the while-loop. In figure B.2 this

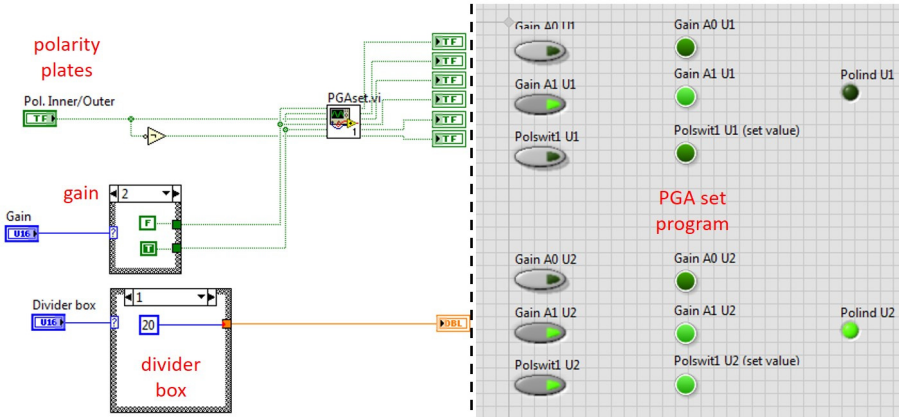


Figure B.3: (left) Cut-out of the main program block diagram where the settings for the ESA are changed. (right) Front screen of the sub-program controlling the settings of the ESA.

is illustrated in the bottom panel, for case 4 setting the lenses (action button 6). This case will be fully executed, and then case 0 is loaded again in the shift register. During execution of one of the cases, the idle indicator will be turned off until the default case 0 is active again. A case can not be interrupted, except by termination of the whole program. The only other exception is the measurement of a spectrum, for which action button 7 can be used.

As an example of what a typical case encompasses, we describe how the ESA HV power supplies receive the right settings. The polarity and the power supply gain for both plates (see appendix A), and the setting of the divider box are required as input and loaded when the 'change settings' button is pressed (button 1 in figure B.1). Figure B.3 shows the block diagram of this particular case in the main program. The divider box setting selects one of the three possible values of the divider box. That value is stored as a variable and is called when the voltages on the ESA plates are calculated from the set energy. The gain determines which of the x2 and x5 gains (see last appendix) should be selected in order to set the right gain for the power supplies. For both of the gains a Boolean value is given as input in the set ESA sub-program, together with the

Boolean values for both of the plate polarities. This sub-program, of which the front screen is shown in figure B.3, gives the right digital (0 or 5 V) values to the various input channels of the HV power supplies. The power supplies send out a polarity indication signal, which is recorded by this sub-program. As the ESA consists of two plates, all signals are in twofold. The digital values for the ESA are shown in output block B, as soon as they are changed.

The main activity of the control program is the measurement of energy distributions of ions and electrons. This measurement is set into motion by giving the energy range (maximum and minimum energy), energy step size, the measurement time per energy point, and the energy limit as input and pressing action button 2, *measure*. At first three arrays, for energy, counts, and beam current, are initialized (the number of measurement points is calculated and the array is filled with this number of zero-values) and are shown as graphs on the main screen (output block A). Starting at the minimum energy, the required voltages on the ESA plates are calculated from the energy and the calibration factors. The control voltage required as input for the HV power supplies is determined from the plate voltage and the settings of the ESA. The next step is to check for each plate if the output voltage is within the pre-set energy limit. If not, the control voltage is altered in such way that the output voltage is adjusted towards the desired voltage. As soon as the voltages on both plates are within the limit, the amount of pulses generated by the MCP are counted for a certain time (the measurement time) and recorded in the count array. The beam current is measured for each energy point at the start of the measurement (see action block 5 for the beam current measurement). If an energy point measurement has concluded, the program will check if the last set energy plus the energy step exceeds the maximum energy. If not, the next energy point is measured, if it is the measurement is finished and the distribution can be saved. If data is ready to be saved an indicator will light up in output block B until the data is saved or a new measurement is started. The measurement can be stopped by pressing the *stop measurement* button (action 7), which will finish the ongoing measurement of an energy point and then halt the spectrum measurement. The arrays and information about the current measurement point (e.g. the energy) are shown in output block B.

Action button 3, *initialize summation*, creates three arrays for energy, counts, and current, and adjusts the axes of the graphs in output block C. These arrays keep record of the total sum of counts and the accumulated beam current of all measurements. Every time a measurement is saved (see next paragraph), the arrays are updated with the data of the measurement. Three graphs are visible in output block C: the total sum of counts, the accumulated beam current, and the total counts divided by the beam current. A list of all measurements included in the summation is also visible.

The data can be saved by the *save data* button (action 4 in figure B.1). Required input is the measurement day (for the folder name) and the name of the measurement file. The measurement file number starts at 1 as default but is alterable. This number will automatically increase by 1 upon saving the next set of data. The energy, counts, and current arrays are saved in a tab-delimited txt-file. All the measurement settings, e.g. the energy step size and the ESA plate polarities, are saved in a separate file. Measurement parameters such as the ion energy and the detection angle can also be recorded in this file, but have to be manually added in the text field next to the button. If desired, a measurement can be saved but excluded from the summation graphs described previously by pressing the '*summation?*' button.

In action block 5 the settings of the electrometer measuring the ion beam current is set as input. These settings determine the current measurement scale. The electrometer has an output voltage ranging from 0-10 V, where 10 V corresponds to the full scale of the meter. The settings in this block are necessary, together with the output voltage, to determine the beam current recorded for each measurement point.

The voltages on the four deceleration lenses (see section 4.4.1) are controlled by action button 6, the '*set lens voltages*' button. A voltage ranging 0-10 V controls each lens, where 10 V corresponds to the full voltage range of the lens. For the voltages given as input in this block, the control voltage is calculated for and sent to each of the four lenses. Each lens has a 0-5 V read-out voltage, corresponding to the full range of the lens. The four output voltages are calculated from these voltages and shown in output block B.

Appendix C

Atomic units

In this work, often atomic units are used instead of SI units. These atomic units are derived from setting four fundamental constants to unity: the reduced Planck's constant \hbar , the elementary charge e , the electron rest mass m_e , and the Coulomb force constant $k_e = 1/4\pi\epsilon_0$. From these four values, the other atomic units can be derived. Here follows an overview of the value in SI units for the fundamental constants and the derived atomic units of length, velocity, and energy:

<i>Physical quantity</i>	<i>Symbol</i>	<i>Value</i>	<i>SI unit</i>
angular momentum	\hbar	$1.05 \cdot 10^{-34}$	J s
charge	e	$1.60 \cdot 10^{-19}$	C
mass	m_e	$9.11 \cdot 10^{-31}$	kg
Coulomb force constant	k_e	$8.99 \cdot 10^9$	$\text{Nm}^2 \text{C}^{-2}$
length	Bohr radius a_0	$5.29 \cdot 10^{-11}$	m
velocity	αc	$2.19 \cdot 10^6$	m/s
energy	$E = m(\alpha c)^2$	$4.36 \cdot 10^{-18}$	J s

Another unit widely used in this work is the electronvolt. The atomic unit of energy is equal to 27.2 eV, the potential energy of a 1s electron in the hydrogen atom.

The ion velocity v_i in atomic units can be calculated from the kinetic energy E_{kin} in keV and the ion mass m_i in amu with the following formula:

$$v_i[\text{a.u.}] = 0.2 \sqrt{\frac{E_{kin}[\text{keV}]}{m_i[\text{amu}]}} \quad (\text{C.1})$$

Curriculum Vitae

Mart Johan Deuzeman

27 July 1990

Born in Rotterdam, the Netherlands

Education

- 2014-2019 **PhD** degree
Zernike Institute for Advanced Materials
University of Groningen
Title thesis: *Generation and interactions of energetic tin ions*
Supervisor: Prof. dr. ir. R.A. Hoekstra
- 2012-2014 **Master** degree in Physics
University of Groningen
Title thesis: *Absolute cross section measurements of ions on coronene*
Supervisor: Prof. dr. ir. R.A. Hoekstra
- 2007-2012 **Bachelor** degree in Physics
University of Groningen
Title thesis: *A stable isotope research on a Pinus Cembra log from the 8.2 ka event period*
Supervisor: Prof. dr. ir. J. van der Plicht

Bibliography

- [1] G.E. Moore, *Electronics*, **38** (1965).
- [2] G.E. Moore, *Int. Electron Devices Meet.*, **21**, 11 (1975).
- [3] T. Ito, S. Okazaki, *Nature*, **406**, 1027 (2000).
- [4] B.J. Lin, *Microelectron. Eng.*, **6**, 31 (1987).
- [5] E.Y. Lam, A.K.K. Wong, *Opt. Express*, **17**, 12259 (2009).
- [6] D.W. Meyers, I.V. Fomenkov, B.A.M. Hansson, B.C. Klene, D.C. Brandt, *Proc. SPIE*, **5751**, 248 (2005).
- [7] I.V. Kozhevnikov, A.V. Vinogradov, *J. Russ. Laser Res.*, **16**, 343 (1995).
- [8] H. Maury, P. Jonnard, J.-M. André, J. Gautier, M. Roulliay, F. Bridou, F. Delmotte, M.-F. Ravet, A. Jérôme, P. Holliger, *Thin Solid Films*, **514**, 278 (2006).
- [9] Q. Huang, M. de Boer, J. Barreaux, R. van der Meer, E. Louis, F. Bijkerk, *Opt. Express*, **22**, 19365 (2014).
- [10] V.V. Medvedev, A.J.R. van den Boogaard, R. van der Meer, A.E. Yakshin, E. Louis, V.M. Krivtsun, F. Bijkerk, *Opt. Express*, **21**, 16964 (2013).
- [11] V.Y. Banine, K.N. Koshelev, G.H.P.M. Swinkels, *J. Phys. D: Appl. Phys.*, **44**, 253001 (2011).

- [12] N.R. Farrar, B.M. La Fontaine, I.V. Fomenkov, D.C. Brandt, *Adv. Opt. Technol.*, **1**, 279 (2012).
- [13] W. Svendsen, G. O’Sullivan, *Phys. Rev. A*, **50**, 3710 (1994).
- [14] G. O’Sullivan, B. Li, R. D’Arcy, P. Dunne, P. Hayden, D. Kilbane, T. McCormack, H. Ohashi, F. O’Reilly, P. Sheridan, E. Sokell, C. Suzuki, T. Higashiguchi, *J. Phys. B: At. Mol. Opt. Phys.*, **48**, 144025 (2015).
- [15] S.N. Srivastava, K.C. Thompson, E.L. Antonsen, H. Qiu, J.B. Spencer, D. Papke, D.N. Ruzic, *J. Appl. Phys.*, **102**, 023301 (2007).
- [16] A.Z. Giovannini, N. Gambino, B. Rollinger, R.S. Abhari, *J. Appl. Phys.*, **117**, 033302 (2015).
- [17] M.M.J.W. van Herpen, D.J.W. Klunder, W.A. Soer, R. Moors, V. Banine, *Chem. Phys. Lett.*, **484**, 197 (2010).
- [18] N.R. Böwering, A.I. Ershov, W.F. Marx, O.V. Khodykin, B.A.M. Hansson, E. Vargas L., J.A. Chavez, I.V. Fomenkov, D.W. Myers, D.C. Brandt, *Proc. SPIE*, **6151**, 61513R (2006).
- [19] H. Mizoguchi, T. Abe, Y. Watanabe, T. Ishihara, T. Ohta, T. Hori, T. Yanagida, H. Nagano, T. Yabu, S. Nagai, G. Soumagne, A. Kurosu, K.M. Nowak, T. Sukanuma, M. Moriya, K. Kakizaki, A. Sumitani, H. Kameda, H. Nakarai, J. Fujimoto, *Proc. SPIE*, **7969** (2011).
- [20] C.L. Rettig, O.V. Khodykin, J.R. Hoffman, W.F. Marx, N.R. Böwering, E. Vargas L., A.I. Ershov, I.V. Fomenkov, W.N. Partlo, *Proc. SPIE*, **5751**, 910 (2005).
- [21] K. Gielissen, *PhD thesis*. Technische Universiteit Eindhoven (2009).
- [22] D.T. Elg, J.R. Sporre, G.A. Panici, S.N. Srivastava, D.N. Ruzic, *J. Vac. Sci. Technol. A*, **34**, 021305 (2016).
- [23] T.H.M. van de Ven, P. Reefman, C.A. de Meijere, R.M. van der Horst, M. van Kampen, V.Y. Banine, J. Beckers, *J. Appl. Phys.*, **123**, 063301 (2018).

- [24] J. Krüger, W. Kautek, *Laser Phys.*, **9**, 30 (1999).
- [25] S.I. Anisimov, D. Bäuerle, B.S. Luk'yanchuk, *Phys. Rev. B*, **48**, 12076 (1993).
- [26] B.N. Chichkov, C. Momma, S. Nolte, F. von Alvensleben, A. Tünnermann, *Appl. Phys. A*, **63**, 109 (1996).
- [27] P.P. Pronko, S.K. Dutta, D. Du, R.K. Singh, *J. Appl. Phys.*, **78**, 6233 (1995).
- [28] S. Preuss, A. Demchuk, M. Stuke, *Appl. Phys. A*, **61**, 33 (1995).
- [29] J. Vincenc Obona, V. Ocelik, J.Z.P. Skolski, V.S. Mitko, G.R.B.E. Römer, A.J. Huis in 't Veld, J.Th.M. De Hosson, *Appl. Surf. Sci.*, **258**, 1555 (2011).
- [30] T. Kato, M. Kurata-Nishimura, T. Kobayashi, Y. Okamura-Oho, T. Sano, Y. Hayashizaki, Y. Matsuo, J. Kawai, *Appl. Phys. A*, **92**, 809 (2008).
- [31] S. Döring, A. Ancona, S. Hädrich, J. Limpert, S. Nolte, A. Tünnermann, *Appl. Phys. A*, **100**, 53 (2010).
- [32] H. Varel, D. Ashkenasi, A. Rosenfeld, M. Wähmer, E.E.B Campbell, *Appl. Phys. A*, **65**, 367 (1997).
- [33] A.Yu. Vinokhodov, K.N. Koshelev, V.N. Krivtsun, M.S. Krivokorytov, Yu.V. Sidelnikov, S.V. Medvedev, V.O. Kompanets, A.A. Melnikov, S.V. Chekalin, *Quant. Electron.*, **46**, 23 (2016).
- [34] B. Toftmann, B. Doggett, C. Budzt-Jørgensen, J. Schou, J.G. Lunney, *J. Appl. Phys.*, **113**, 083304 (2013).
- [35] S. Amoruso, X. Wang, C. Altucci, C. de Lisio, M. Armenante, R. Bruzzese, R. Velotta, *Appl. Phys. Lett.*, **77**, 3728 (2000).
- [36] S. Amoruso, X. Wang, C. Altucci, C. de Lisio, M. Armenante, R. Bruzzese, N. Spinelli, R. Velotta, *Appl. Surf. Sci.*, **186**, 358 (2002).
- [37] S. Nolte, C. Momma, H. Jacobs, A. Tünnermann, B.N. Chichkov, B. Wellegehausen, H. Welling, *J. Opt. Soc. Am. B*, **14**, 2716 (1997).

- [38] B. Verhoff, S.S. Harilal, A. Hassanein, *J. Appl. Phys.*, **111**, 123304 (2012).
- [39] K. Furusawa, K. Takahashi, H. Kumagai, K. Midorikawa, M. Obara, *Appl. Phys. A*, **69**, S359 (1999).
- [40] Z. Zhang, P.A. VanRompay, J.A. Nees, P.P. Pronko, *J. Appl. Phys.*, **92**, 2867 (2002).
- [41] O. Albert, S. Roger, Y. Glinec, J.C. Loulergue, J. Etchepare, C. Boulmer-Leborgne, J. Perrière, E. Millon, *Appl. Phys. A*, **76**, 319 (2003).
- [42] J. Yang, Y. Zhao, X. Zhu, *Appl. Phys. Lett.*, **88**, 094101 (2006).
- [43] M.E. Shaheen, J.E. Gagnon, B.J. Fryer, *Laser Phys.*, **24**, 106102 (2014).
- [44] C.T. Hebeisen, G. Sciani, M. Harb, R. Ernstorfer, S.G. Kruglik, R.J.D. Miller, *Phys. Rev. B*, **78**, 081403 (2008).
- [45] A. Menéndez-Manjón, S. Barcikowski, G.A. Shafeev, V.I. Mazhukin, B.N. Chichkov, *Laser Part. Beams*, **28**, 45 (2010).
- [46] S. Amoruso, G. Ausanio, R. Bruzzese, M. Vitiello, X. Wang, *Phys. Rev. B*, **71**, 033406 (2005).
- [47] M. Mero, J. Liu, W. Rudolph, D. Ristau, K. Starke, *Phys. Rev. B*, **71**, 115109 (2005).
- [48] R. Stoian, D. Ashkenasi, A. Rosenfeld, E.E.B. Campbell, *Phys. Rev. B*, **62**, 13 167 (2000).
- [49] R. Stoian, A. Rosenfeld, D. Ashkenasi, I.V. Hertel, N.M. Bulgakova, E.E.B. Campbell, *Phys. Rev. Lett.*, **88**, 097603 (2002).
- [50] T. Ditmere, J.W.G. Tisch, E. Springate, M.B. Mason, N. Hay, R.A. Smith, J. Marangos, M.H.R. Hutchinson, *Nature*, **386**, 54 (1997).
- [51] F. Claeysens, M.N.R. Ashfold, E. Sofoulakis, C.G. Ristoscu, D. Anglos, C. Fotakis, *J. Appl. Phys.*, **91**, 6162 (2002).

- [52] A. Vinokhodov, V. Krivtsun, M. Krivokorytov, Y. Sidelnikov, S. Chekalin, V. Kompanets, A. Melnikov, K. Koshelev, "Femtosecond laser pre-pulse technology for LPP EUV source", 2014 International Workshop on EUV and Soft X-Ray Sources, Dublin, November 3-6, 2014.
- [53] E. Bodewits, R. Hoekstra, K. Dobes, F. Aumayr, Phys. Rev. A, **90**, 052703 (2014).
- [54] R. Danzl, F. Helml, S. Scherer, J. Mech. Eng., **57**, 245 (2011).
- [55] E.G. Gamaly, Phys. Rep., **508**, 91 (2011).
- [56] R. Le Harzic, D. Breitling, M. Weikert, S. Sommer, C. Föhl, S. Valette, C. Donnet, E. Audouard, F. Dausinger, Appl. Surf. Sci., **249**, 322 (2005).
- [57] B. Doggett, J.G. Lunney, J. Appl. Phys., **109**, 093304 (2011).
- [58] M.E. Shaheen, J.E. Gagnon, B.J. Fryer, J. Appl. Phys., **114**, 083110 (2013).
- [59] B. Thestrup, B. Toftmann, J. Schou, B. Doggett, J.G. Lunney, Appl. Surf. Sci., **197-198**, 175 (2002).
- [60] B. Thestrup, B. Toftmann, J. Schou, B. Doggett, J.G. Lunney, Appl. Surf. Sci., **208-209**, 33 (2003).
- [61] D. Campos, S.S. Harilal, A. Hassanein, J. Appl. Phys., **108**, 113305 (2010).
- [62] J.R. Freeman, S.S. Harilal, B. Verhoff, A. Hassanein, B. Rice, Plasma Sources Sci. and Technol., **21**, 055003 (2012).
- [63] A. Ben-Yakar, R.L. Byer, J. Appl. Phys., **96**, 5316 (2004).
- [64] D. Pietroy, Y. Di Maio, B. Moine, E. Baubeau, E. Audouard, Opt. Express, **20**, 29900 (2012).
- [65] X. Ni, K.K Anoop, X. Wang, D. Paparo, S. Amoruso, R. Bruzzese, Appl. Phys. A, **117**, 111 (2014).

- [66] E. A. Cummings, J. E. Daily, D. S. Durfee, S. D. Bergeson, *Phys. Plasmas*, **12**, 123501 (2005).
- [67] T.C. Killian, S. Kulin, S.D. Bergeson, L.A. Orozco, C. Orzel, S.L. Rolston, *Phys. Rev. Lett.*, **83**, 4776 (1999).
- [68] A. Flacco, A. Guemnie-Tafo, R. Nuter, M. Veltcheva, D. Batani, E. Lefebvre, V. Malka, *J. Appl. Phys.*, **104**, 103304 (2008).
- [69] P. McKenna, D.C. Carroll, O. Lundh, F. Nürnberg, K. Markey, S. Bandyopadhyay, D. Batani, R.G. Evans, R. Jafer, S. Kar, D. Neely, D. Pepler, M.N. Quinn, R. Redaelli, M. Roth, C.-G. Wahlström, X.H. Yuan, M. Zepf, *Laser Part. Beams*, **26**, 591 (2008).
- [70] V. Bakshi, *EUV Sources for Lithography*, Bellingham, WA: SPIE (2006).
- [71] N. Farid, S. S. Harilal, H. Ding, A. Hassanein, *Phys. Plasmas*, **20**, 073114 (2013).
- [72] R. W. Coons, D. Campos, M. Crank, S. S. Harilal, A. Hassanein, *Proc. of SPIE*, **7636**, 763636 (2010).
- [73] Z. Chen, X. Wang, D. Zuo, J. Wang, *Laser Part. Beams*, **34**, 552 (2016).
- [74] A. V. Gurevich, L. V. Pariiskaya, L. P. Pitaevskiĭ, *J. Exp. Theor. Phys.*, **22**, 647 (1966).
- [75] M. Murakami, Y.G. Kang, K. Nishihara, S. Fujioka, H. Nishimura, *Phys. Plasmas*, **12**, 062706 (2005).
- [76] P. Mora, *Phys. Rev. Lett.*, **90**, 185002 (2003).
- [77] N.M. Bulgakova, A.V. Bulgakov, O.F. Bobrenok, *Phys. Rev. E*, **62**, 5624 (2000).
- [78] M. Murakami, M.M. Basko, *Phys. Plasmas*, **13**, 012105 (2006).
- [79] J.E. Crow, P.L. Auer, J.E. Allen, *J. Plasma Phys.*, **14**, 65 (1975).
- [80] C.H. Sack, H. Schamel, *Phys. Rep.*, **156**, 311 (1987).

- [81] A. V. Arefiev, B. N. Breizman, *Phys. Plasmas*, **16**, 055707 (2009).
- [82] D. Bennaceur-Doumaz, D. Bara, M. Djebli, *Laser Part. Beams*, **33**, 723 (2015).
- [83] S. Fujioka, H. Nishimura, K. Nishihara, M. Murakami, Y.-G. Kang, Q. Gu, K. Nagai, T. Norimatsu, N. Miyanaga, Y. Izawa, K. Mima, Y. Shimada, A. Sunahara, H. Furukawa, *Appl. Phys. Lett.*, **87**, 241503 (2005).
- [84] A. Thum-Jäger, K. Rohr, *J. Phys. D: Appl. Phys.*, **32**, 2827 (1999).
- [85] J.I. Apiñaniz, A. Peralta Conde, R. Martinez Perez de Mendiola, *Eur. Phys. J. D*, **69**, 265 (2015).
- [86] L. Landau, L. Lifshitz, *Fluid Mechanics*, Oxford: Pergamon (1987).
- [87] R.A. London, M.D. Rosen, *Phys. Fluids*, **29**, 3813 (1986).
- [88] F. Robicheaux, J.D. Hanson, *Phys. Plasmas*, **10**, 2217 (2003).
- [89] I. Pelah, *Phys. Lett. A*, **59**, 348 (1976).
- [90] D. Kurilovich, A.L. Klein, F. Torretti, A. Lassise, R. Hoekstra, W. Ubachs, H. Gelderblom, O.O. Versolato, *Phys. Rev. Appl.*, **6**, 014018 (2016).
- [91] D. Bäuerle, *Laser Processing and Chemistry*, Berlin: Springer (2011).
- [92] A. Thum-Jäger, B.K. Sinha, K. Rohr, *Phys. Rev. E*, **63**, 016405 (2000).
- [93] Z. Chen, X. Wang, D. Zuo, P. Lu, J. Wang, *Laser Phys. Lett.*, **13**, 056002 (2016).
- [94] M.M. Basko, I.P. Tsygvintsev, *Comp. Phys. Comm.*, **214**, 59 (2017).
- [95] G. Cisneros, J.S. Helman, C.N.J. Wagner, *Phys. Rev. B*, **25**, 4248 (1982).

- [96] A.I. Golovashkin, I.S. Levchenko, G.P. Motulevich, A.A. Shubin, J. Exp. Theor. Phys., **24**, 1622 (1967).
- [97] L.C. Feldman, J.W. Mayer, *Fundamentals of surface and thin film analysis*, New York, NY: Elsevier (1986).
- [98] SRIM, www.srim.org.
- [99] N. Bohr, *The penetration of atomic particles through matter*, K. Dan. Vidensk. Selsk., Mat.-Fys. Medd., **XVIII**, 8 (1948).
- [100] G. Molière, Z. Naturforschg., **2 a**, 133 (1947).
- [101] O.B. Firsov, J. Exp. Theor. Phys., **33**, 696 (1958).
- [102] J.F. Ziegler, J.P. Biersack, M.D. Ziegler, *SRIM: The stopping and range of ions in matter*, Chester, MD: SRIM Co. (2008).
- [103] J. Burgdörfer, P. Lerner, F.W. Meyer, Phys. Rev. A, **44**, 5674 (1991).
- [104] A. Arnau, F. Aumayr, P.M. Echenique, M. Grether, W. Heiland, J. Limburg, R. Morgenstern, P. Roncin, S. Schippers, R. Schuch, N. Stolterfoht, P. Varga, T.J.M. Zouros, HP. Winter, Surf. Sci. Rep., **27**, 113 (1997).
- [105] F. Aumayr, H. Kurz, D. Schneider, M.A. Briere, J.W. McDonald, C.E. Cunningham, HP. Winter, Phys. Rev. Lett., **71**, 1943 (1993).
- [106] H. Kurz, F. Aumayr, HP. Winter, D. Schneider, M.A. Briere, J.W. McDonald, Phys. Rev. A, **49**, 4693 (1994).
- [107] H. Winter, C. Auth, R. Schuch, E. Beebe, Phys. Rev. Lett., **71**, 1939 (1993).
- [108] H.D. Hagstrum, Phys. Rev., **96**, 336 (1954).
- [109] R. Hentschke, K.J. Snowdon, P. Hertel, W. Heiland, Surf. Sci., **173**, 565 (1986).

- [110] J.P. Briand, L. de Billy, P. Charles, S. Essabaa, P. Briand, R. Geller, J.P. Desclaux, S. Bliman, C. Ristori, *Phys. Rev. Lett.*, **65**, 159 (1990).
- [111] HP. Winter, F. Aumayr, *J. Phys. B: At. Mol. Opt. Phys.*, **32**, R39 (1999).
- [112] *Oven head technical datasheet*, PK10-0107-DT01, v1.0.
- [113] D. Winters, *PhD thesis*, Rijksuniversiteit Groningen (2004).
- [114] E.H.A. Granneman, M.J. van der Wiel, *Transport, dispersion and detection of electrons, ions and neutrals*, Chapter 4 (1979) *in: Handbook on synchrotron radiation*, Eds.: D.E. Eastman, Y. Farge, E.E. Koch.
- [115] M. Unipan, *PhD thesis*. Rijksuniversiteit Groningen (2007).
- [116] P.A. Zeijlmans van Emmichoven, P.A.A.F. Wouters, A. Niehaus, *Surf. Sci.*, **195**, 115 (1988).
- [117] H. Hofsäss, K. Zhang, A. Mutzke, *Appl. Surf. Sci.*, **310**, 134 (2014).
- [118] V.I. Shulga, *Appl. Surf. Sci.*, **439**, 456 (2018).
- [119] K. Wittmaack, *Nucl. Instrum. Methods Phys. Res. B*, **380**, 57 (2016).
- [120] R. Souda, T. Aizawa, C. Oshima, S. Otani, Y. Ishizawa, *Surf. Sci.*, **194**, L119 (1988).
- [121] W. Möller, W. Eckstein, *Nucl. Instrum. Methods Phys. Res. B*, **2**, 814 (1984).
- [122] A. Mutzke, R. Schneider, W. Eckstein, R. Dohmen, IPP-Report **12/8** (2011).
- [123] M. P. Seah and T. S. Nunney, *J. Phys. D: Appl. Phys.*, **43** 253001 (2010).
- [124] H. Hofsäss, K. Zhang, *Nucl. Instrum. Methods Phys. Res. B*, **267**, 2731 (2009).

- [125] K. Wittmaack, J. Appl. Phys., **96**, 2632 (2004).
- [126] H. Paul, Nucl. Instrum. Methods Phys. Res. B, **247**, 166 (2006).
- [127] P. Filliatre, C. Jammes, B. Geslot, Nucl. Instrum. Methods Phys. Res. A, **618**, 294 (2010).
- [128] K.N. Yu, C.W.Y. Yip, D. Nikezic, J.P.Y. Ho, V.S.Y. Koo, Appl. Radiat. Isot., **59**, 363 (2003).
- [129] J. P. J. Dubois, K. Achkasov, D. Kogut, A. Ahmad, J. M. Layet, A. Simonin, G. Cartry, J. Appl. Phys., **119**, 193301 (2016).
- [130] M. Jurado Vargas, A. Fernández Timón, J. Radioanal. Nucl. Chem., **305**, 479 (2015).
- [131] N.V. Novikov, Y.A. Teplova, Y.A. Fainberg, V.S. Kulikauskas, Nucl. Instrum. Methods Phys. Res. B, **235**, 448 (2005).
- [132] L. Folkerts, *PhD thesis*, Rijksuniversiteit Groningen (1992).
- [133] A. Robin, W. Heiland, J. Jensen, J.I. Juaristi, A. Arnau, Phys. Rev. A, **64**, 052901 (2001).
- [134] W. Möller, W. Eckstein, Nucl. Instrum. Methods Phys. Res. B, **2**, 814 (1984).
- [135] M. Krems, J. Zirbel, M. Thomason, R.D. DuBois, Rev. Sci. Instrum., **76**, 093305 (2005).

Dankwoord

Wetenschap en het schrijven van een proefschrift kun je nooit zonder de steun van anderen en daarom wil ik als afsluiting nog de mensen bedanken die mij de afgelopen jaren hebben geholpen:

Ronnie, in al die jaren dat je mijn begeleider bent geweest heb ik, eerst als masterstudent en daarna als promovendus, onze samenwerking altijd als zeer prettig ervaren. Onze wetenschappelijke discussies en je commentaar op mijn werk was altijd goed, je begeleiding in het lab ook (waar nodig), maar bovenal kon ik je humor en de vele verhalen tijdens onze koffiepauzes zeer waarderen. Dank je wel!

Wim, ik wil jou graag bedanken voor onze samenwerking. Jouw kritische vragen en opmerkingen stuurden mijn onderzoek vaak bij in de goede richting en lieten mij vaak een denkrichting zien die ik eerder nog niet had overwogen.

Oscar, vooral in het begin van mijn promotie hebben wij veel contact gehad, tijdens mijn experimenten in Amsterdam en de uitwerking daarvan. Dank je wel voor je begeleiding en jouw aanstekelijke en inspirerende enthousiasme!

I would like to express my gratitude to the members of the assessment committee, Fritz Aumayr, Joost Frenken, and Bart Kooi, for reviewing the manuscript and for their remarks. I would also like to thank Wim van der Zande for his work as our 'liaison officer'.

Jan, jouw hulp in het lab was onontbeerlijk tijdens mijn onderzoek en in dit manuscript staan jouw tekeningen op verschillende plekken. Buiten het lab heb ik je vooral je gezellige en humoristische kant leren kennen. Dank je wel daarvoor!

I would also like to thank the other (former) members of our research

group in Groningen: Thomas, Geert, Leon, Dmitrii, Edita, Xin, Wen, Subam, Yinning, Ernesto, Nolan, Steven, Piet, Wessel, Klaas, Arnold, Walewein, Eva, Amber, Yahia, and Harry. You were the main reason I went with pleasure to Nijenborgh 4 and that I enjoyed my years as a PhD! A special thanks is for Walewein, who provided a part of the simulation results in chapter 6.

To my fellow members of the research group and other collaborators in Amsterdam (Dmitry, Francesco, Joris, Ruben, Alex, Bo, Zoi, John, Lars, Lucas, Laurens, Thomas, Arend-Jan, Jan, Aneta, Eric, Sjoerd, Stefan, Kjeld, Alessandro, Nick, Thijs, and Tiago): thank you! I always felt welcome when I travelled to Amsterdam and I hope ARCNL and the group continues to flourish as it does now.

Ik ben ook erg dankbaar voor de technische ondersteuning van de mechanische en elektronische werkplaatsen in zowel Amsterdam als Groningen en de software-afdeling in Amsterdam. Zonder jullie hulp met onder andere de ontwikkeling van de tinovens en de vele andere onderdelen van mijn opstellingen was mijn onderzoek niet mogelijk geweest. Op deze plaats wil ik ook Henk-Jan Boluijt, van wie de tekeningen op meerdere plekken in dit werk terugkomen, en Martin Stokroos, die mij enorm heeft geholpen met het vervangen van de regelapparatuur in Groningen, bedanken voor hun hulp. Naast de technische ondersteuning wil ik ook de Groningse elektronische werkplaats en Martin bedanken voor de gezelligheid tijdens de lunch.

Ik wil ook de andere ondersteunende diensten in Groningen en Amsterdam bedanken, zoals de financiële dienst, de ICT-afdelingen, secretariaat en personeelszaken die mijn werk een stuk soepeler hebben gemaakt de afgelopen jaren.

Ook buiten mijn werk ben ik door velen geholpen. Ik wil al mijn vrienden bedanken die de afgelopen jaren aan de ene kant voor de nodige afleiding hebben gezorgd en aan de andere kant geïnteresseerd waren in mijn onderzoek.

Gerrit en Wilco, onze paden lopen al een lange tijd parallel aan elkaar en ik hoop dat ze dat nog een hele tijd blijven doen. Dank jullie wel daarvoor en ik ben blij dat jullie als paranimfen mij bijstaan bij de verdediging van mijn proefschrift.

Ik ben veel dank verschuldigd aan mijn Heit en Mem, mijn broers en

hun gezinnen (Albert, Asia, Eva & Clara; Tsjipke, Angelina, Iris & Raf; Henk Leo, Rommie, Aline, Jitze & Jorrit; en Sybren), en mijn schoonfamilie (Wim & Lia, en Josse & Sanne). Jullie steunden mij op verschillende manieren: bemoedigende woorden, jullie interesse, oppassen op de kinderen of gewoon gezellig op bezoek. Dank jullie wel daarvoor!

Annemara en Elianne, ik ben blij dat jullie de afgelopen jaren in ons leven gekomen zijn. Jullie zorgden voor de nodige afleiding en door jullie kon ik het belang van mijn werk ook relativeren. Mirte, van begin tot eind moedigde jij mij aan, ondersteunde mij en was daar voor mij, waardoor ik deze promotie succesvol kon afronden. Dank jullie wel en ik hou van jullie.